

EFFECT OF $\text{Cu}(\text{In,Ga})_3\text{Se}_5$ ULTRA-THIN LAYER ON
OPTICAL PROPERTIES AND PHOTOVOLTAIC
EFFICIENCY OF $\text{Cu}(\text{In,Ga})\text{Se}_2$ THIN FILM SOLAR CELLS



Miss Boonyaluk Namnuan

จุฬาลงกรณ์มหาวิทยาลัย
CHULALONGKORN UNIVERSITY

A Dissertation Submitted in Partial Fulfillment of the Requirements
for the Degree of Doctor of Philosophy in Physics
Department of Physics
Faculty of Science
Chulalongkorn University
Academic Year 2018
Copyright of Chulalongkorn University

ผลของชั้นบางยิ่งยวดของ $\text{Cu(In,Ga)}_3\text{Se}_5$ ต่อสมบัติเชิงแสงและประสิทธิภาพทางโฟโตโวล
ทาคิกของเซลล์สุริยะชนิดฟิล์มบาง Cu(In,Ga)Se_2



วิทยานิพนธ์นี้เป็นส่วนหนึ่งของการศึกษาตามหลักสูตรปริญญาวิทยาศาสตรดุษฎีบัณฑิต
สาขาวิชาฟิสิกส์ ภาควิชาฟิสิกส์
คณะวิทยาศาสตร์ จุฬาลงกรณ์มหาวิทยาลัย
ปีการศึกษา 2561
ลิขสิทธิ์ของจุฬาลงกรณ์มหาวิทยาลัย



จุฬาลงกรณ์มหาวิทยาลัย
CHULALONGKORN UNIVERSITY



จุฬาลงกรณ์มหาวิทยาลัย
CHULALONGKORN UNIVERSITY

Thesis Title EFFECT OF $\text{Cu}(\text{In,Ga})_3\text{Se}_5$ ULTRA-THIN
LAYER ON OPTICAL PROPERTIES AND
PHOTOVOLTAIC EFFICIENCY OF
 $\text{Cu}(\text{In,Ga})\text{Se}_2$ THIN FILM SOLAR CELLS
By Miss Boonyaluk Namnuan
Field of Study Physics
Thesis Advisor Assistant Professor Sojiphong Chatraphorn,
Ph.D.

Accepted by the Faculty of Science, Chulalongkorn
University in Partial Fulfillment of the Requirement for the Doctor
of Philosophy

..... Dean of the Faculty of
Science
(Professor POLKIT SANGVANICH, Ph.D.)

DISSERTATION COMMITTEE

..... Chairman
(Assistant Professor Rattachat Mongkolnavin,
Ph.D.)

..... Thesis Advisor
(Assistant Professor Sojiphong Chatraphorn,
Ph.D.)

..... Examiner
(Associate Professor Thiti Bovornratanaraks,
Ph.D.)

..... Examiner
(Assistant Professor Montian Tianprateep,
Ph.D.)

..... External Examiner
(Assistant Professor Rachsak Sakdanuphab,
Ph.D.)

บุญลักษณ์ นามนวน : ผลของชั้นบางยิ่งยวดของ $\text{Cu(In,Ga)}_3\text{Se}_5$ ต่อสมบัติเชิงแสงและประสิทธิภาพ
 ทางโฟโตโวลตาอิกของเซลล์สุริยะชนิดฟิล์มบาง Cu(In,Ga)Se_2 . (EFFECT OF
 $\text{Cu(In,Ga)}_3\text{Se}_5$ ULTRA-THIN LAYER ON OPTICAL PROPERTIES
 AND PHOTOVOLTAIC EFFICIENCY OF Cu(In,Ga)Se_2 THIN FILM
 SOLAR CELLS) อ.ที่ปรึกษาหลัก : ผศ. ดร. โสจิพงศ์ นัตราภรณ์

ฟิล์มบาง 135-คอปเปอร์อินเดียมแกลเลียมไคซีลีไนด์ (135-CIGS) ที่มีความหนาแตกต่างกันถูกปลูกลงบนพื้นผิวของฟิล์มบาง 112-คอปเปอร์อินเดียมแกลเลียมไคซีลีไนด์ (112-CIGS) หนาประมาณ 1.8 ไมโครเมตร ในการประดิษฐ์เซลล์สุริยะชนิดฟิล์มบาง CIGS ในการวิจัยพบว่าช่องว่างแถบพลังงาน (E_g) มีการเปลี่ยนไปอย่างมีนัยสำคัญสำหรับฟิล์มบาง 135-CIGS ที่มีความหนา 10 นาโนเมตร โดยมีค่า E_g เท่ากับ 1.19 eV เมื่อเปรียบเทียบกับฟิล์มบาง 112-CIGS ที่มีค่า E_g เท่ากับ 1.15 อิเล็กตรอนโวลต์ ซึ่งผลที่เกิดขึ้นนี้นำไปสู่การเพิ่มขึ้นของแรงดันวงจรเปิด (V_{oc}) ของเซลล์สุริยะ สำหรับการวัดการส่งผ่านเชิงแสงไม่แสดงให้เห็นผลของฟิล์มชั้นเดี่ยวของ 135-CIGS และค่าสูงสุดของ V_{oc} ที่ได้มีค่า 670 มิลลิโวลต์ โดยได้จากฟิล์มบาง 135-CIGS ที่มีความหนา 5 ถึง 10 นาโนเมตรที่ปลูกลงบนชั้นฟิล์มบาง 112-CIGS ซึ่งค่า V_{oc} ที่ได้จากฟิล์มบาง 112-CIGS มีค่า 646 มิลลิโวลต์ ส่วนประสิทธิภาพการแปลงพลังงานสำหรับฟิล์มบาง 135-CIGS ที่มีความหนาน้อยกว่า 80 นาโนเมตร จะมีค่าลดลงเล็กน้อยเมื่อเปรียบเทียบกับเซลล์สุริยะของฟิล์มบาง 112-CIGS เนื่องจากความสามารถในการผลิตกระแสเชิงแสงที่ลดลง พารามิเตอร์เซลล์สุริยะจะลดลงอย่างมากเมื่อความหนาของชั้น 135-CIGS มีความหนาที่มากขึ้น สำหรับประสิทธิภาพเชิงควอนตัมบ่งชี้ว่าการเปลี่ยนจุดเริ่มต้นที่มีการดูดกลืนแสงไปในทิศทางที่ความยาวคลื่นสั้นเมื่อความหนาของชั้น 135-CIGS มีความหนาที่เพิ่มขึ้นจะสอดคล้องกับผลการวัดของการส่งผ่านเชิงแสง การวัดสเปกตรัมโฟโตลูมินเนสเซนซ์ของโครงสร้าง 135-CIGS/112-CIGS ด้วยความหนาของชั้น 135-CIGS ที่แตกต่างกันสามารถจำแนกได้เป็นการเปลี่ยนของระดับชั้นพลังงานระหว่างระดับพลังงานของผู้ให้ (donor) กับระดับพลังงานของผู้รับ (acceptor) และการเปลี่ยนของระดับชั้นพลังงานระหว่างแถบพลังงานของผู้ให้ (conduction band) กับระดับพลังงานของผู้รับ (acceptor) และสเปกตรัมโฟโตลูมินเนสเซนซ์ที่ได้จะขึ้นตรงกับอุณหภูมิที่ทำให้ไปยังชั้นงานและความเข้มของแสงเลเซอร์ที่ใช้กระตุ้นชั้นงาน ในทางตรงกันข้ามสำหรับโครงสร้าง 112-CIGS/135-CIGS สเปกตรัมโฟโตลูมินเนสเซนซ์แสดงการแยกออกของพีคอย่างเด่นชัดและไม่ขึ้นตรงกับอุณหภูมิและความเข้มของแสงเลเซอร์เนื่องจากผลของการแทรกสอดทางแสง สำหรับฟิล์มบาง 135-CIGS (ความหนา 1-200 นาโนเมตร) ที่ปลูกลงบนฟิล์มบาง 112-CIGS ความหนา 1.8 ไมโครเมตร แสดงความเป็นสารกึ่งตัวนำชนิดพี ในขณะที่ฟิล์มบาง 112-CIGS (ความหนา 5-300 นาโนเมตร) ที่ปลูกลงบนฟิล์มบาง 135-CIGS ความหนา 1.8 ไมโครเมตร จะแสดงความเป็นสารกึ่งตัวนำชนิดเอ็น

จุฬาลงกรณ์มหาวิทยาลัย
 CHULALONGKORN UNIVERSITY

สาขาวิชา ฟิสิกส์
 ปีการศึกษา 2561

ลายมือชื่อนิติ
 ลายมือชื่อ อ.ที่ปรึกษาหลัก

5672823023 : MAJOR PHYSICS

KEYWORD: 135-CIGS, 112-CIGS, Solar Cells, Thin Films

Boonyaluk Namnuan : EFFECT OF $\text{Cu}(\text{In,Ga})_3\text{Se}_5$ ULTRA-THIN LAYER ON OPTICAL PROPERTIES AND PHOTOVOLTAIC EFFICIENCY OF $\text{Cu}(\text{In,Ga})\text{Se}_2$ THIN FILM SOLAR CELLS . Advisor: Asst. Prof. Sojiphong Chatraphorn, Ph.D.

$\text{Cu}(\text{In,Ga})_3\text{Se}_5$ (135-CIGS) layers with various thicknesses were deposited on the surface of ~ 1.8 micron thick $\text{Cu}(\text{In,Ga})\text{Se}_2$ (112-CIGS) photon absorber in the fabrication of CIGS thin film solar cells. This significantly affects the shift of the optical band gap energy from 1.15 eV (112-CIGS) to 1.19 eV, with only 10 nm thick of 135-CIGS capping layer, leading to the increase in the open-circuit voltage (V_{oc}) of the solar cells. The optical transmission spectra show no sign of separated 135-CIGS layer. The maximum V_{oc} of 670 mV is obtained from 5-10 nm thick 135-CIGS capping layer on 112-CIGS compared to 646 mV of only 112-CIGS. The power conversion efficiencies of the devices covered with 135-CIGS with thickness less than 80 nm are slightly lower than that of the uncovered 112-CIGS solar cells due to lower generated photocurrents. The solar cell parameters become dramatically deteriorate with thicker 135-CIGS capping layer. The XRD also shows the shift of diffraction peak toward larger 2-theta without peak broadening or splitting when the thickness of 135-CIGS is increased. The external quantum efficiency (EQE) measurements indicate the shift of absorption threshold towards shorter wavelength when the thickness of 135-CIGS is increased that is consistent with the optical transmission measurements. The photoluminescence (PL) spectra of 135-CIGS/112-CIGS heterostructure with various thicknesses of 135-CIGS layer are identified as donor-to-acceptor pairs (DAPs) and free (conduction band) -to-bound (acceptor) transitions and show the temperature and excitation power dependence on the PL spectra. On the contrary, when the thin 112-CIGS layer is deposited on top of 135-CIGS (112-CIGS/135-CIGS), the PL spectra show more pronounced and resolved peaks which are surprisingly independent of temperature and excitation power because of the interference effect. The thin 135-CIGS (1-200 nm) capping layer on the 1.8 micron 112-CIGS films show the nature of p-type, while the thin 112-CIGS (5-300 nm) capping layer on the 1.8 micron 135-CIGS films exhibit the nature of n-type.

จุฬาลงกรณ์มหาวิทยาลัย
CHULALONGKORN UNIVERSITY

Field of Study: Physics
Academic Year: 2018

Student's Signature
Advisor's Signature

ACKNOWLEDGEMENTS

I am very appreciative for the direct and indirect support I have received from many people on the course of my research. Without their help, this work would not have been possible, and I would not have reached to this point.

First of all, I would greatly appreciate my dissertation advisor, Assistant Professor Dr. Sojiphong Chatraphorn for accepting me as a PhD student, giving me an opportunity to work on this research and helping me going through all steps, guiding me through this work, organizing the financial support and giving me with fruitful discussions, kindness suggestion, scientific skills and general conversations as much as a person can do. I am also grateful for the efforts that Emeritus Professor Per Olof Holtz (Linköping University), Assistant Professor Dr. Kajornyod Yoodee and Dr. Thiti Taychatanapat have invested in me with their times, shared many helpful and encouraged thoughts in fruitful discussions.

I would be thankful for the chairman and the committee members, Assistant Professor Dr. Rattachat Mongkolnavin, Assistant Professor Dr. Montian Tianprateep, Associated Professor Dr. Thiti Bovornratanaraks and Assistant Professor Dr. Rachsak Sakdanuphab of being the examiner for this dissertation and commenting on this research.

I would also acknowledge and appreciate the Associated Professor Dr. Vittaya Amornkitbamrung, Khon Kaen University, for supporting X-ray diffraction of thin films analysis. In addition, I would also like to thank Mr. Pornsak Panchawirat for helping with the SEM and EDS measurements. This work is complete with their kindness and generosity.

I would also like to thank all other, past, present members and guests of the Semiconductor Physics Research Laboratory (SPRL) who came through my life for me to learn to be a good grown-up, for teamwork, scientific and less scientific discussions, friendliness, empathy, encouragement, generousities, laughs and general collaboration in the lab whose names are not mentioned here because

of a lot of listing.

I would like to acknowledge the financial support from Science Achievement Scholarship of Thailand, 90th Anniversary of Chulalongkorn University Fund and also Thailand Center of Excellence in Physics (ThEP Center) for the financial support during my PhD program.

Furthermore, I would like to thank to my beloved and my parents for their patience, understanding, accepting the identity of me and enabling me on the path of dreams until success. “We are the team throughout this life.”

“There is no one who comes into our lives that will not change us.”

Boonyaluk Namnuan



TABLE OF CONTENTS

	Page
ABSTRACT (THAI)	iii
ABSTRACT (ENGLISH).....	iv
ACKNOWLEDGEMENTS.....	v
TABLE OF CONTENTS.....	vii
LIST OF TABLES.....	xi
LIST OF FIGURES	xii
CHAPTER I INTRODUCTION.....	1
1.1 Overview.....	1
1.2 CIGS Thin Film Solar Cells	4
1.2.1 Brief History of Cu(In,Ga)Se ₂ Solar Cells	4
1.2.2 Cu(In,Ga)Se ₂ Solar Cell Structure.....	5
1.3 Role of 135-CIGS	7
1.4 Motivation and Scope of This Dissertation	10
1.5 Objective of the Research.....	11
1.6 Dissertation Outline	11
CHAPTER II BASICS OF Cu(In,Ga)Se ₂ ; MATERIALS, SOLAR CELLS, AND GROWTH PROCESSES	12
2.1 Structural Properties	12
2.1.1 Crystallographic Structure of Cu(In,Ga)Se ₂ Compounds.....	12
2.1.2 Phase Diagram of Cu-In-Ga-Se Material System	14
2.1.2.1 The Cu-In-Se Material system.....	14
2.1.2.2 Defects in Cu-In-Se Material system	15
2.1.2.3 The Cu-Ga-Se Material System.....	17
2.1.2.4 The Cu-Se Material System.....	19
2.2 Optical Properties of CIGS Thin Film.....	19
2.2.1 Optical Absorption	19

2.2.2 Photoluminescence Technique	24
2.3 Photovoltaic Devices	27
2.3.1 P-N Junction of a Solar Cell.....	27
2.3.2 The Equivalent Circuit and Characteristic of Solar Cell.....	28
2.4 Growth Process of CIGS Thin Films.....	32
2.4.1 Co-Evaporation Process	32
2.4.1.1 Single-Stage Process.....	32
2.4.1.2 Two-Stage Process	33
2.4.1.3 Three-Stage Process	34
2.4.2 Reaction Deposition and H ₂ Se Selenization	35
2.5 CIGS Band Gap Profiling Techniques	36
2.5.1 Non Band Gap Grading	36
2.5.2 Normal Band Gap Grading.....	36
2.5.3 Double Band Gap Grading.....	37
2.5.4 Valence Band Offset	37
CHAPTER III FABRICATION AND CHARACTERIZATION OF Cu(In,Ga)Se₂ AND Cu(In,Ga)₃Se₅/Cu(In,Ga)Se₂ THIN FILM SOLAR CELLS.....	39
3.1 CIGS Solar Cell Fabrication.....	40
3.1.1 Soda-Lime Glass (SLG) Substrate Cleaning Procedures	40
3.1.2 Mo Back Contacts	41
3.1.3 Cu(In,Ga)Se ₂ and Cu(In,Ga) ₃ Se ₅ Absorber Layers.....	42
3.1.3.1 Molecular Beam Epitaxy System	42
3.1.3.2 Calibration of Molecular Constituents	46
3.1.3.3 Calculation of the CIGS Film Deposition	48
3.1.3.4 Deposition of the CIGS Thin Films	50
3.1.4 CdS Buffer Layer	53
3.1.5 Window Layers of CIGS	54
3.1.6 Al Metal Grid	55
3.2 Sample Characterizations	55

3.2.1 Scanning Electron Microscopy (SEM).....	55
3.2.2 Energy Dispersive X-Ray Spectroscopy (EDS).....	56
3.2.3 X-Ray Diffraction (XRD)	56
3.2.4 Optical Transmittance and reflectance Spectroscopy	57
3.2.5 Photoluminescence (PL).....	58
3.2.6 Atomic Force Microscopy (AFM)	59
3.2.7 Current-Voltage Characteristics	60
3.2.8 External Quantum Efficiency (EQE) Measurement.....	60
CHAPTER IV EFFECTS OF $\text{Cu}(\text{In,Ga})_3\text{Se}_5$ THIN LAYER ON $\text{Cu}(\text{In,Ga})\text{Se}_2$ ABSORBER THIN FILMS	62
4.1 Motivation.....	62
4.2 Experimental Details	65
4.3 Surface morphology and cross-section	66
4.4 Optical band gap energy	70
4.5 Crystal structure.....	77
4.6 Raman spectra and Raman shift	80
4.7 J-V characteristics and QE of CIGS devices	82
4.8 Summary remarks	84
CHAPTER V PHOTOLUMINESCENCE OF 135-CIGS/112-CIGS HETEROSTRUCTURE SYSTEM.....	86
5.1 PL of 112-CIGS, 135-CIGS thin films and 135-CIGS/112-CIGS heterostructure	86
5.2 PL of 112-CIGS/135-CIGS heterostructure	95
5.2.1 The interference effects in PL of 135-CIGS and CIGS thin films	97
5.2.1.1 Effect of surface roughness	98
5.2.1.2 Effect of 135-CIGS layer thickness.....	100
5.2.1.2 Effect of CIGS film composition	104
5.2.2 The PL correction for 112-CIGS/135-CIGS heterostructures.....	104
5.3 Summary Remarks.....	108
CHAPTER VI CONCLUSION	110

REFERENCES 113
VITA..... 123



LIST OF TABLES

	Page
Table 1: Majority defect pairs in CuInSe ₂ under the excess In compositions with an excess or deficiency of selenium (ΔS) ([39] and reference therein).....	16
Table 2: Formation energies of intrinsic defects in CuInSe ₂ ([39] and reference therein).....	16
Table 3: Soda-lime glass compositions.....	41
Table 4: Thermal expansion coefficients of substrate materials.....	41
Table 5: Density, mass per mole and α_i parameter of the materials.	49
Table 6: Parameters for the growth of CIGS.	51
Table 7: Parameters for the CdS chemical bath process.....	54
Table 8: Ga composition ratio (x), Cu composition ratio (y) obtained from the EDS measurements and ycal as calculated from overall thickness of the films.	76
Table 9: XRD peak position of (112) and (220) phases, shift of peak position, ratio of lattice parameters (c/a) and volume of unit cell of 112-CIGS, 135-CIGS and 135-CIGS/112-CIGS.....	76

LIST OF FIGURES

	Page
Figure 1: The evolution of world records of conversion efficiencies for various types of solar cells 1975-2017 [1].	3
Figure 2: Theoretical efficiency for various types of solar cells depends on band gap energy [5].	5
Figure 3: Schematic of Cu(In,Ga)Se ₂ thin film solar cell structure.	7
Figure 4: Schematic of band diagram of Cu(In,Ga)Se ₂ thin film solar cell with valence band widening at CdS/CIGS interface.	9
Figure 5: (a) sphalerite or zinc blend (X= Zn atom (Cu or In) and Y= Se atom) and (b) Chalcopyrite (A= Cu, B= In and C= Se atom [5].	13
Figure 6: Lattice constant of a- and c-axis as a function of the composition parameter of x in the CuIn _{1-x} Ga _x Se ₂ alloys ([36] and references therein).	13
Figure 7: Phase diagram along the Cu ₂ Se-In ₂ Se ₃ pseudobinary section of the Cu-In-Se material system ([37] and references therein).	14
Figure 8: Phase diagram of Cu ₂ Se and Ga ₂ Se ₃ for a formation of CGS compounds ([37] and references therein).	18
Figure 9: Phase diagram of the Cu-Se system above 25°C: (1) liquid+β Cu ₂ Se; (2) Cu+β Cu ₂ Se; (3) Cu+liquid; (4) liquid+Cu _{2-x} Se; (5) Cu+α Cu ₂ Se; (6) α Cu ₂ Se+Cu _{2-x} Se; (7) Cu _{2-x} Se+liquid; (8) Cu _{2-x} Se+liquid; (9) Cu _{2-x} Se+CuSe h.t.; (10) Cu _{2-x} Se+Cu ₃ Se ₂ ; (11) Cu ₃ Se ₂ +CuSe h.t.; (12) Cu ₃ Se ₂ +CuSe l.t.; (13) CuSe l.t.+CuSe ₂ ; (14) CuSe h.t.+CuSe ₂ ; (15) CuSe h.t.+liquid; (16) CuSe ₂ +liquid; (17) CuSe ₂ +Se; h.t.= high temperature; l.t.= low temperature [40].	18
Figure 10: Optically generated electron-hole pair formation in a semiconductor.	19
Figure 11: Optical transmission in a differential length.	20
Figure 12: Absorption coefficient spectrum for various types of semiconductors [5].	21
Figure 13: The multiple reflections and transmissions of thin film with film thickness d.	24
Figure 14: Radiative recombination paths: a) interband transition, b) donor to valence band transition, c) conduction to acceptor band transition, d) donor to acceptor band transition and e) conduction to intermediate band or intermediate to valence band transition.	25

Figure 15: The PL broad spectrum due to the variety of Coulomb's interaction distances.....	25
Figure 16: The structure of the p-n junction with the space charge region (SCR) and the electric field due to the charged carriers.	27
Figure 17: (a) Equivalence circuit of solar cell and (b) J-V characteristics of a p-n junction solar cell.....	29
Figure 18: A plot of open-circuit voltage (V_{oc}) and band gap energy (E_g) for various Ga compositions of CIGS thin film solar cells [8].	30
Figure 19: Schematic of the growth profile rate and Cu composition ratio (y) for single-stage deposition.....	32
Figure 20: Schematic of the growth profile rate and Cu composition ratio (y) for the 2-stage deposition.	34
Figure 21: Schematic of the growth profile rate and Cu composition (y) for the 3-stage deposition.....	35
Figure 22: Band gap profiles in CIGS thin film solar cell (a) standard band structure, (b) normal grading , (c) double band gap grading and (d) valence band offset.....	38
Figure 23: The schematic of 135-CIGS/112-CIGS solar cell fabrication.....	39
Figure 24: (a) The schematic illustration of the MBE system with RHEED and pyrometer setting. (b)The photograph of molecular beam epitaxy system contains all of the components needed for growth and in-situ analysis (SPRL, Chulalongkorn University).	44
Figure 25: Plots of elemental deposition rates vs. inverse temperature.....	47
Figure 26: In situ monitoring signals during the 3-stage CIGS growth and capping layer.....	53
Figure 27: Schematic illustration of the diffractometer of crystal analysis and of the conditions necessary for diffraction.....	57
Figure 28: Example of optical transmittance spectrum of i-ZnO.	58
Figure 29: Schematic diagram of photoluminescence spectroscopy setup.....	59
Figure 30: Schematic illustration of an atomic force microscope.	61
Figure 31: Example external quantum efficiency of a 3-stage CIGS solar cell.....	61
Figure 32: Surface morphologies of (a) 2 μm thick 112-CIGS (b) 2 μm thick 135-CIGS, 135-CIGS/112-CIGS with 135-CIGS capping layer (c) 10 nm, (d) 20 nm, (e) 40 nm and (f) 200 nm.....	68

Figure 33: FESEM surface and cross-section images of (a), (c) 1.8 μm thick 112-CIGS, (b), (d) 2 μm thick 135-CIGS and 135-CIGS/112-CIGS with 135-CIGS capping layer of thickness (e) 40 nm and (f) 200 nm.	69
Figure 34: Plots of (a) optical transmittance and (b) reflectance spectra of 112-CIGS, 135-CIGS and 135-CIGS/112-CIGS with various thicknesses of 135-CIGS; 10, 20, 40, 80, 200 and 300 nm. Inset in (a) shows the results of the transmittance of physically stacked layers of 112-CIGS and 135-CIGS by laying two samples together.	74
Figure 35: Tauc plot of $(\alpha h\nu)^2$ vs. incident photon energy ($h\nu$) for 112-CIGS, 135-CIGS and 135-CIGS/112-CIGS with various thicknesses of 135-CIGS. A straight line is extrapolated to determine band gap energy (E_g).	75
Figure 36: A plot of band gap energy vs. Cu-atomic ratios. Open circles are from the measurements with $y = 0.33, 0.65$ and 0.90 . Solid black circles represent the 112-CIGS with 135-CIGS capping layer with the thickness of 10-300 nm using calculated values of y	75
Figure 37: The XRD patterns showing (a) broad spectra, (b) (112) plane and (c) (220)(204) planes of 112-CIGS, 135-CIGS and 135-CIGS/112-CIGS with 135-CIGS capping layer of 10, 80 and 200 nm thick.	78
Figure 38: Raman spectra of 112-CIGS, 135-CIGS and 135-CIGS/112-CIGS with 135-CIGS capping layer of 10 and 200 nm thick.	81
Figure 39: Plots of solar cell parameters of 112-CIGS and 135-CIGS/112-CIGS.	83
Figure 40: External quantum efficiency of 112-CIGS and 135-CIGS/112-CIGS solar cells.	84
Figure 41: The PL spectra of 135-CIGS, 112-CIGS and 135-CIGS/112-CIGS thin films at 10 K. The black line is for the high power (35 mW) and the red line, green line and blue line are for the low excitation power.	88
Figure 42: The PL spectra of the 112-CIGS thin film under temperatures from 10 K to 300 K. Inset is the fitting result of PL spectrum at 10 K using Gaussian distribution.	89
Figure 43: The PL spectra of the 135-CIGS/112-CIGS thin film with 10 nm thick of 135-CIGS capping layer under temperatures from 10 K to 300 K. Inset is the fitting result of PL spectrum at 10 K using Gaussian distribution.	90
Figure 44: The PL spectra of the 135-CIGS thin film under temperatures from 10 K to 200 K. Inset is the fitting result of PL spectrum at 10 K using Gaussian distribution.	91
Figure 45: The Arrhenius plot of temperature-dependent PL intensity vs. $1/T$ for fitting peak 1 and peak 2.	92

Figure 46: Peak energy at high excitation power plotted as a function of temperature from 10–300 K for 112-CIGS, 135-CIGS and 135-CIGS/112-CIGS.....	93
Figure 47: The energy level diagram of (a) 112-CIGS (b) 135-CIGS/112-CIGS and (c) 135-CIGS thin films.	94
Figure 48: PL spectra of 135-CIGS/112-CIGS with various thicknesses of 135-CIGS capping layer at 10 K.	95
Figure 49: SEM Cross-sectional images of (a) 135-CIGS/112-CIGS with 40 nm thick 135-CIGS and 112-CIGS/135-CIGS with (b) 50 nm and (c) 200 nm thick 112-CIGS.	96
Figure 50: The PL spectra of 112-CIGS/135-CIGS with 50 and 200 nm thick 112-CIGS capping layers at lower (red line) and higher (black line) excitation power from 10–200 K.....	97
Figure 51: Schematic illustration of PL generated in the CIGS absorber film and collected at angle θ_1 to the surface normal. Red and black lines perform up-going and down-going rays, respectively.	98
Figure 52: Effect of rms surface roughness on PL emission for (a) 112-CIGS, (b) 135-CIGS, (c) 135-CIGS/112-CIGS and (d) 112-CIGS/135-CIGS thin films.	99
Figure 53: Simulation of Gaussian distribution (measured PL) counterpart with full width at half maximum (FWHM) affected by the interference effect.	100
Figure 54: The comparison of SEM surface, AFM, and PL measurement corrected by the interference factor ($1-R*c$) among the various thicknesses of 135-CIGS layer. .	102
Figure 55: The comparison of SEM surface, AFM, and PL measurement corrected by the interference factor for various compositions of CIGS thin films.....	103
Figure 56: The PL spectra of the 112-CIGS/135-CIGS thin film with 10 nm thick of 112-CIGS capping layer under temperatures from 10 K to 200 K. Inset is the fitting result of PL spectrum at 10 K using Gaussian distribution.	105
Figure 57: The PL spectra of the 112-CIGS/135-CIGS thin film with 10 nm thick of 112-CIGS capping layer under various excitation power.....	106
Figure 58: The PL spectra, PL correction and $1-R$ of the 112-CIGS/135-CIGS thin film with various thicknesses of 112-CIGS capping layer.	107

CHAPTER I

INTRODUCTION

1.1 Overview

At present, suitable clean resources such as renewable energy is indispensable demand for taking the place of oil resource. Using of fossil fuels produce air pollutants that are related to health risks as well as global warming by the increase in green-house gas concentration, i.e., CO, NO_x, SO_x, etc. Therefore, a step forward in the chasing of alternative energy resources in the cleanest and free from carbon such as wind, marine energy, hydroelectric, geothermal and solar power are all important. Today, many people are familiar with the photovoltaic cells or solar panels found on space crafts or satellites, rooftops and handheld calculators and many other appliances that generate electricity from the sunlight. Then, the solar energy is perhaps appropriate for country receiving the sunlight throughout the year. The first-generation solar cells, i.e., crystalline silicon (c-Si) is more efficient semiconducting material used in photovoltaic technology for the production of solar cells. However, c-Si in solar cell process requires high purity about 99.9999%, therefore, its production cost has also increased. The second- and third-generation solar cells are based on amorphous silicon, thin film solar cells, i.e., CdTe and Cu(In,Ga)Se₂ (112-CIGS), and organic solar cell materials (recently by the perovskite solar cells) and multi-junction solar cells, respectively, have been possible to reduce the production costs compared to that of the first generation. These two latter generations continuously hold the world record in solar cell performance. The evolution of world record of power conversion efficiencies (PCE) and solar cell types is illustrated in Fig. 1 [1]. Thin film solar cells have received attentions until present time, especially CIGS thin film solar cells. The world's record in 2017 of laboratory cell efficiency for CIGS is 22.9% by Solar Frontier, a company based in Japan. At the latest, there is a new world record for CuInSe₂ (CIS) thin film solar cell efficiency [2]. These gain in efficiency of both CIGS and CIS thin films in the latter are due to the improved post-deposition treatment of the film surface with alkaline metal compounds [3, 4]. CIGS is usually used as a photon absorber layer for CIGS thin film solar cell devices. Its band gap energy can be tuned from 1.02 to 1.66 eV by varying the ratio of group-III elements (x

= $[Ga]/([Ga]+[In])$) that lies within the structure of $CuInSe_2$ ($E_g = 1.02$ eV) and $CuGaSe_2$ ($E_g = 1.66$ eV) as shown in Fig. 2 [5]. Theoretically, the CIGS thin film solar cells have a potential to achieve higher efficiency if its band gap energy is appropriately adjusted to match the solar spectrum. However, the performance of high efficiency CIGS solar cells is confronted with the limitation of increasing open-circuit voltage (V_{oc}) and short-circuit current density (J_{sc}). These are two competing parameters and difficult to increase simultaneously. The alternation increase in the V_{oc} with larger band gap energy of CIGS absorber can cause photocurrent loss. The increase in J_{sc} also causes the reduction in V_{oc} . There are several attempts in recent years to increase both V_{oc} and J_{sc} by tuning of conduction band energy, e.g., front band gap grading, back band gap grading and double grading. However, it is difficult to control the precise fluxes of Ga and In to achieve the conduction band grading. The minimum front grading should be contained within the *space charge region* (SCR) without losing fill factor (FF) and J_{sc} [6]. However, there is one technique that can also enhance both V_{oc} and J_{sc} that can be achieved by the modification of the surface of 112-CIGS absorber by introducing $Cu(In,Ga)_3Se_5$ (135-CIGS) layer. This phase is unexpectedly found on 112-CIGS absorber, especially Cu-poor film, and it is also called β -phase for CIGS structure. Theoretically, 135-CIGS are believed to induce the valence band offset at the interface region [7]. It has been interesting for a long time, however, the study of this defect layer in detail is quite minimum. Then, the effect of 135-CIGS defect layer on 112-CIGS absorber is an important issue for this dissertation.

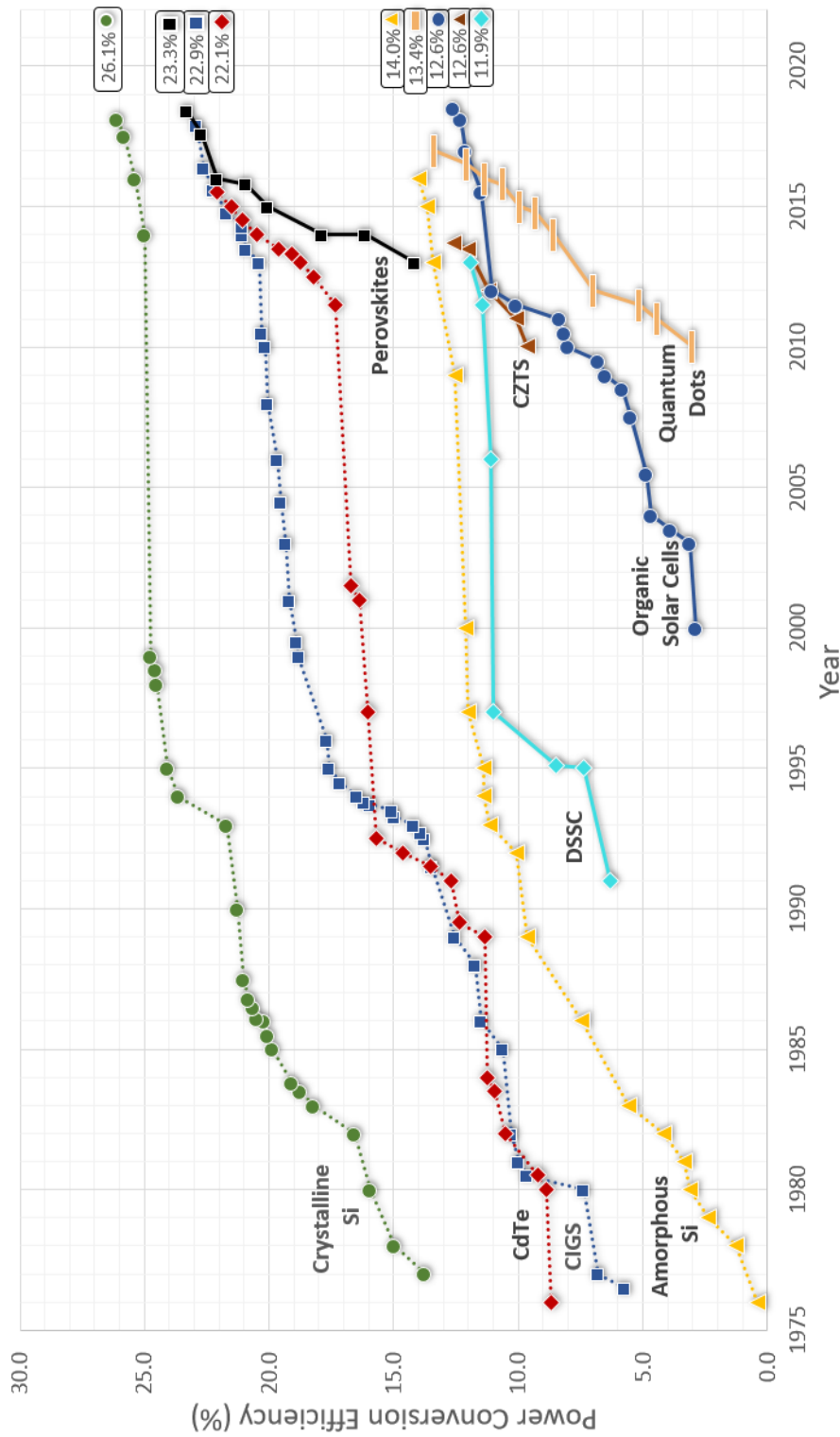


Figure 1: The evolution of world records of conversion efficiencies for various types of solar cells 1975-2017 [1].

1.2 CIGS Thin Film Solar Cells

1.2.1 Brief History of Cu(In,Ga)Se₂ Solar Cells

There is a long history of research and technological development based on CIGS thin film because CIGS can offer an exciting opportunity for the improvement of efficiency and relatively lower-cost of solar cells. Dating back in 1975, a CuInSe₂ (CIS) single crystal was evaporated by a layer of CdS, Bell laboratory scientists eventually achieved 12% of PCE [8]. During 1983–1984, Boeing Corporation reported higher efficiencies by evaporating gallium (Ga) into the CIS structure. Ga could increase V_{oc} and FF corresponding to higher band gap energy [9, 10]. Before 1990, Arco Solar developed a deposition-reaction process using Cu and In metallic precursors, subsequently, feeding by H₂Se. During the process, the absorber layer was doped with Na. It gave better efficiencies to about 15% [11]. Then, in 1995, Na containing glass such as soda-lime glass (SLG) became a standard substrate for CIGS thin film solar cell [12], because it contains a Na up to 15% of NaO₂. However, in 1994, the modification method of CIGS thin film fabrication for efficiency above 20 percent called 3-stage process was created by the scientists at National Renewable Energy Laboratories (NREL), USA [13]. In parallel, there are many researches trying to improve the performances of CIGS thin film solar cells by doping sulfur (S) to selenium (Se) position. Sulfur could widen E_g at the interface by tuning E_g from 1.02 eV to 1.52 eV. As a result, this technique can suppress the recombination at the interface region [14, 15]. Nonetheless, the sulfurization requires the use of toxic H₂S gas to supply sulfur to the Cu(In,Ga)(Se,S)₂ films. This technique may not be preferred for the absorber fabrication in a large scale. However, the development of CIGS efficient solar cell has never been stopped up until this time. There are a large number of research laboratories and companies studying subvariant techniques or processes leading to higher performance of CIGS absorber layer. The highest 22.9% PCE as stated above was achieved by the surface modification after the completion of the 3-stage absorber fabrication or post-deposition treatment with alkaline metal compounds [3]. The post-deposition treatment can also form a Cu-depleted layer and modify the chemical composition at the surface region and thereby J_{sc} benefit.

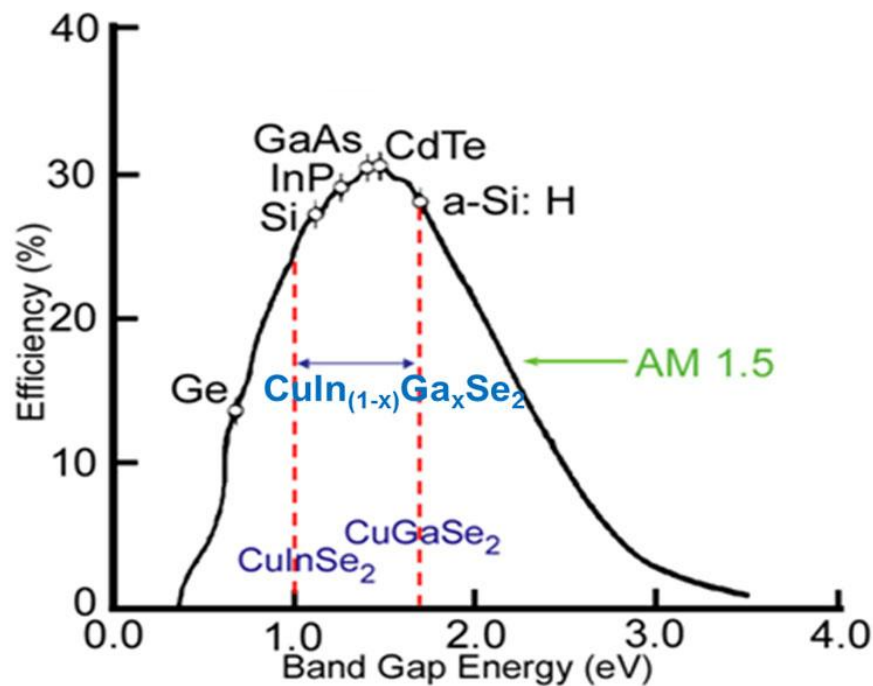


Figure 2: Theoretical efficiency for various types of solar cells depends on band gap energy [5].

1.2.2 Cu(In,Ga)Se₂ Solar Cell Structure

The typical components of CIGS solar cell comprise six main components as shown in Fig. 3, from bottom to top;

(1) Substrate: the most common substrate is soda-lime glass (SLG). It has well-matched thermal expansion coefficient as Cu(In,Ga)Se₂ [16] (SLG= $9 \times 10^{-6} \text{ K}^{-1}$, CIGS= $11\text{-}13 \times 10^{-6} \text{ K}^{-1}$). The highest limitation of thermal stability allows process temperature up to around 600°C. The SLG acts as a Na source that can diffuse into the CIGS layer through the molybdenum (Mo) back contact layer during the CIGS deposition process. With appropriate doping of Na, it results in larger CIGS grain size, preferential orientation [17], carrier concentration [18], group-III elements gradient [19], leading to higher efficiency devices. Moreover, alternative substrates, e.g., polymers and metal-foils can be used to replace the SLG in the sense of low weight and flexibility.

(2) Back contact: molybdenum (Mo) is most widely used as a back contact electrode because of its comparatively low-cost, high melting point above 2500°C and

low diffusivity. Mo is generally coated on SLG substrate by DC magnetron sputtering technique with typical thickness of 0.5–1.0 μm .

(3) p-type CIGS absorber: following molybdenum layer, there are two common processes are usually formed CIGS film: (i) Co-evaporation where Cu, In, Ga and Se are simultaneously evaporated during deposition. (ii) Deposition reaction where a precursor metal film reacts with the selenium from the selenization in a second step. However, the 3-stage co-evaporation technique is the most efficient method to date to achieve high CIGS solar cell performance. This technique will be described in details in Chapter III. A typical thickness of CIGS absorber layer is approximately 1.8–2.0 μm .

(4) CdS buffer layer: is usually deposited by chemical bath deposition (CBD) technique. CBD of CdS gives the best performance and most reliable solar cells. The absorber is completely covered by CdS with a film thickness of 50 nm.

(5) Window layer: the CIGS solar cell consists of two window layers, i.e., the high resistance ZnO or intrinsic ZnO (i-ZnO) and the low resistance aluminum doped n-type ZnO(Al). These are deposited after the buffer layer. ZnO(Al) layer provides maximum electrical conductivity at minimum optical absorption. The window layers are commonly formed by RF magnetron sputtering with a typical thickness of i-ZnO and ZnO(Al) approximately 50 nm and 200 nm, respectively.

(6) Front-contact electrode: Al is usually used as a metal front contact by employing thermal evaporation of Al through a shadow mask. The front-contact electrodes can increase the collection of the electrical current. A typical thickness of Al layer is approximately 2 μm .

Further details of the processing steps in each layer are explained in Chapter III.

Al	Al
i-ZnO/ZnO:Al	0.25-1 μm
Cds	50 nm
Cu(In,Ga)Se ₂	1-3 μm
Molybdenum (Mo)	0.5-1.0 μm
Glass, metal, polymer	

Figure 3: Schematic of Cu(In,Ga)Se₂ thin film solar cell structure.

1.3 Role of 135-CIGS

The beginning point of consideration 135-chalcopyrite composition was exposed by Schmid *et al.* in 1993 [20]. They found a polycrystalline CuInSe₂ thin film with slightly Cu-poor composition at the surface. It exhibits a Cu-deficient surface with a 1:3:5 stoichiometry of CuIn₃Se₅ (135-CIS); whereas the bulk material is 1:1:2 stoichiometry of CuInSe₂ (112-CIS). Then, they replaced the model of chalcopyrite/defect-chalcopyrite heterojunction from the previous model of the 112-CIS/CdS heterostructure. The 135-CIS and 135-CIGS are normally known as an ordered defect compounds (ODCs). It has a wide band gap energy in the range of 1.30–1.50 eV. These ODCs may be one of the factors that can help improving the CIGS solar cell performance. Evidentially, the Cu-depleted surface can induce the defect layer by shifting the valence band that was further studied by Schmid's group [20]. The valence band offset can increase the band gap at the interface and thus improve V_{oc} . This effect causes a shift of the regime $p = n$ into the absorber and then push away from the defect region at the CdS/CIGS interface. It results in a decrease in the recombination rate, because the valence band offset acts as a large transport barrier for holes, keeping them away from the interface [7, 21]. This Cu-depleted region is well-matched to the n-type CdS semiconductor. Then, a defect phase, i.e., CuIn₃Se₅ (135-CIS) or Cu(In,Ga)₃Se₅ (135-CIGS) which appears to be intrinsic or slightly n-type could form a *pseudo-homojunction* as shown in Fig. 4.

There are a lot of researches that study the 135-chalcopyrite composition through the single crystal or polycrystalline structure, e.g., CuIn_3Se_5 , CuGa_3Se_5 and $\text{Cu}(\text{In,Ga})_3\text{Se}_5$ films in order to understand the physical, optical, crystallographic phase, and electrical properties.

For example, in 1995, Negami *et al.* studied the structure, optical and electrical properties of the 135-CIGS films as a function of Ga content ($x = [\text{Ga}]/([\text{Ga}]+[\text{In}])$). They found the films with x ratio lower than 0.5 are certainly appeared with that ordered vacancy chalcopyrite and they also showed that the conductivity of the film was about $10^{-6}/\Omega\cdot\text{cm}$ for $x \leq 0.3$ and $10^{-7}/\Omega\cdot\text{cm}$ for $x \geq 0.3$ [22]. Afterwards, the comparison of structural and optical for CuIn_3Se_5 and $\text{Cu}(\text{In,Ga})_3\text{Se}_5$ single crystals were determined by other groups. The lattice constants of $\text{Cu}(\text{In,Ga})_3\text{Se}_5$ are slightly lower than those of CuIn_3Se_5 . The band gap energy evaluated from optical absorption shows 1.26 and 1.40 eV for CuIn_3Se_5 and $\text{Cu}(\text{In,Ga})_3\text{Se}_5$, respectively [23, 24]. Moreover, the excitation-dependent and temperature-dependent photoluminescence was also observed for CuIn_3Se_5 film. The dominant transition type of donor to acceptor (D-A) was the signature for CuIn_3Se_5 film [25, 26]. Additionally, several researches have reported the surface defect chalcopyrite or ordered defect compound that always forms spontaneously in growing a slightly Cu-poor ($y = [\text{Cu}]/([\text{Ga}]+[\text{In}])$) film in range 0.90 to 0.98. Later then, in 1993 up until present time, some groups need to identify the existence of 135-CIGS layer. Then, there are several techniques substantiate the existence of 135-CIGS defect layer counterpart with its effect on the CIGS absorber. Those techniques are, for examples, cathodoluminescence [27], atom probe tomography [28], X-ray photoelectron spectroscopy (XPS) [29], convergent-beam electron diffraction [30], grazing incident X-ray diffraction (GIXRD) [31], Rietveld refinement method [32] and positron annihilation spectroscopy [33].

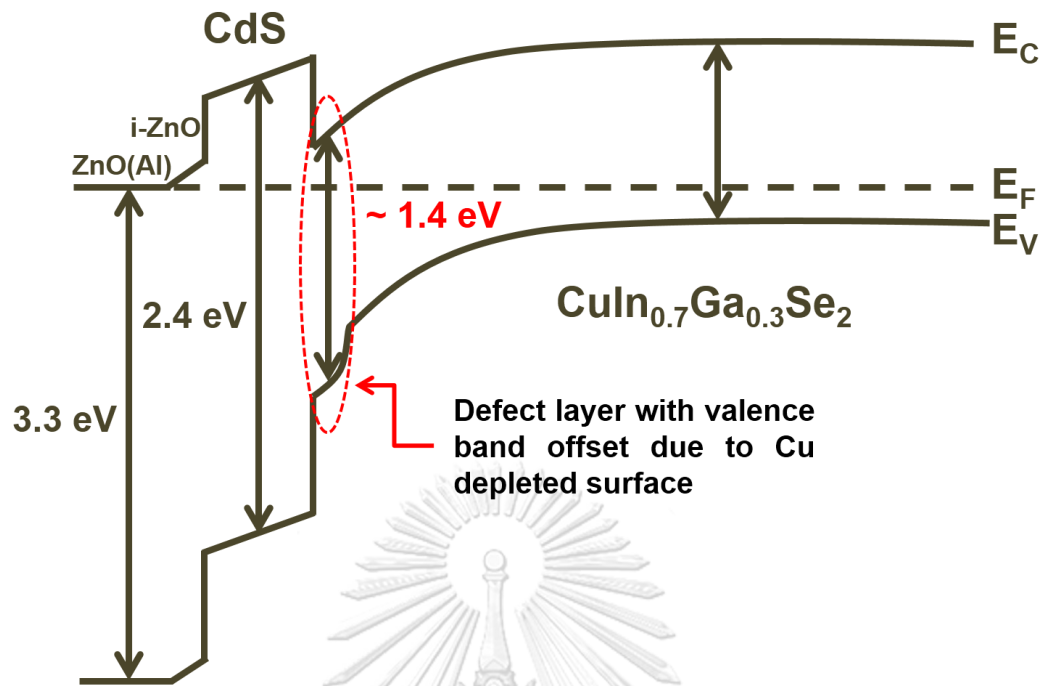


Figure 4: Schematic of band diagram of Cu(In,Ga)Se₂ thin film solar cell with valence band widening at CdS/CIGS interface.

Moreover, it has been reported how 135-chalcopyrite composition has an effect on the 112-chalcopyrite thin film solar cells. In 1998, the effect of CuIn₃Se₅ with various thicknesses on CuInSe₂ thin films and devices was investigated by Kwon's group research. The optimum device yielded a solar efficiency of 8.46 percent with a thin CuIn₃Se₅ capping layer of 100 nm. They found the reduction of cell efficiency as CuIn₃Se₅ layer increased [34]. This similar observation was also found in the work of Islam and his group. They studied the effect of group-III element ratio and selenium flux over the formation of Cu(In,Ga)₃Se₅ on the CIGS film. They discovered an appropriate thin layer of this defect phase that would play the important role for high efficiency and this phase tended to increase with the decrease in Se flux [33]. In 2015, Nishimura *et al.* inserted Cu(In,Ga)₃Se₅ at CdS/CIGS interface for 1.4 eV band gap energy of CIGS. The highest conversion efficiency of 14.4 percent and V_{oc} of 720 mV was reported for 30 nm thick of 135-CIGS layer. They suggested that there may have a valence band offset at the interface. By inserting a wide-gap layer of 135-CIGS, it can decrease a recombination rate by repelling holes from the interface

[35]. Then, the thickness of 135-CIGS on 112-CIGS absorber is the main key factor under study for this dissertation.

1.4 Motivation and Scope of This Dissertation

The 135-chalcopyrite composition was discovered by chance on the surface of 112-composition absorber for which the film was a slightly Cu-poor composition [20]. The ODC is considered to play an important role in improving the performance of the CIGS thin film solar cells. Then, there have been several attempts in many years trying to understand and needing to confirm the appearance and effects of 135-chalcopyrite composition, i.e., CuIn_3Se_5 , CuGa_3Se_5 and $\text{Cu}(\text{In,Ga})_3\text{Se}_5$ by various methods previously mentioned. However, those characteristics have not been yet adequate or less report on optical properties and photovoltaic efficiency versus the quantity of this ODC. Thus, in this dissertation, ultra-thin $\text{Cu}(\text{In,Ga})_3\text{Se}_5$ (135-CIGS) films of various thicknesses are intentionally deposited on the 112-CIGS absorber surface. The effects of 135-CIGS layer on 112-CIGS thin films on the performance of CIGS solar cells are investigated. The optical properties of the films are examined by optical transmission and reflection spectroscopy as well as photoluminescence (PL) technique. The first tools are used to obtain the optical band gap energy (E_g) of the materials while the latter technique is used to probe the radiative recombination transitions for the defect states or impurity levels of the 135-CIGS/112-CIGS heterostructure. The various thicknesses of 135-CIGS on 112-CIGS are the main key factor for this research.

Importantly, it is indispensable to couple the relationship with the 112-CIGS solar cell performances and the properties of 135-CIGS with respect to its thickness via the optical characterizations.

The chalcopyrite absorber layers either 135-CIGS or 112-CIGS are fabricated by molecular beam deposition (MBD) technique. The effects of 135-CIGS on 112-CIGS are also explored by atomic force microscope (AFM), X-ray diffraction (XRD), scanning electron microscope (SEM), energy dispersive X-ray diffraction spectroscopy (EDS), J-V characteristic and external quantum efficiency (EQE) measurements.

1.5 Objective of the Research

The objectives of this dissertation are

1. To fabricate and verify the existence of $\text{Cu}(\text{In,Ga})_3\text{Se}_5$ ultra-thin layer capping on $\text{Cu}(\text{In,Ga})\text{Se}_2$ thin films,
2. To describe effects of $\text{Cu}(\text{In,Ga})_3\text{Se}_5$ ultra-thin layer on $\text{Cu}(\text{In,Ga})\text{Se}_2$ thin films on their optical and photovoltaic properties.

1.6 Dissertation Outline

This dissertation consists of six chapters. Chapter I covers the introduction of this research, i.e., CIGS thin film solar cells, literature reviews based on the role of 135-chalcopyrite structure, motivation and scope of this dissertation. Chapter II describes the background of 135- and 112-chalcopyrite materials, CIGS band gap profiling techniques, optical band gap calculation, photoluminescence, current density-voltage characteristics of solar cells, 3-stage process of CIGS absorber fabrication and molecular beam deposition technique. Chapter III introduces the experimental details of the fabrication of absorbers and solar cells. The calibrations of molecular constituents for the CIGS absorbers are explained in details. The characterizations of the samples are described. Chapter IV presents the results of the macroscopic measurements for 112-CIGS, 135-CIGS and 135-CIGS/112-CIGS heterostructure via SEM, AFM, optical transmission and reflection, EDS and XRD. Moreover, the results of the solar cell devices will be determined by the J-V characteristic and the EQE measurements. Chapter V shows the consequences of 135-CIGS/112-CIGS and 112-CIGS/135-CIGS in their microstructure, i.e., defect states by means of the photoluminescence (PL) technique. Finally, in chapter VI, the important results are summarized and the prospect guidelines for future research will be given.

CHAPTER II

BASICS OF Cu(In,Ga)Se₂; MATERIALS, SOLAR CELLS, AND GROWTH PROCESSES

The relevant structural properties of CIGS system through the I-III-VI₂ phase diagram is described in this chapter. Besides, methods for the fabrication of CIGS absorber are mentioned. Thereafter, the approaches of CIGS band gap grading techniques are presented. Then, the overview of optical and photovoltaic properties of CIGS materials is given. It is the basic for understanding and explaining the behavior of Cu(In,Ga)₃Se₅ (135-CIGS) effects on CIGS absorber and CIGS thin film solar cells.

2.1 Structural Properties

2.1.1 Crystallographic Structure of Cu(In,Ga)Se₂ Compounds

The crystal structure of CuInSe₂ materials is the I-III-VI₂ (ABC₂) ternary compounds. It virtually exhibits either tetragonal with space group of $I\bar{4}2d$, that is a chalcopyrite structure or the doubling cubic unit cell of zinc blend structure with space group $F\bar{4}3m$, that is a *sphalerite structure*. A and B-metallic atoms are tetrahedrally coordinated to four C non-metallic-atoms while each C-atom is tetrahedrally coordinated to two A-atoms and two B-atoms as depicted in Fig. 5. The *c*-axis (*z direction*) of the tetragonal chalcopyrite structure is not exactly twice of the *a*-axis (*x and y direction*). It is generally slightly less than twice of the dimension along the *a*-axis, i.e., $c \leq 2a$. The primitive unit cell has eight atoms and is four times as large as the primitive unit cell for the sphalerite structure.

The substitution of Ga atoms into In lattice sites in the CIS structure can form the alloying of CuIn_{1-x}Ga_xSe₂ where *x* can vary from 0 to 1 and cause the reducing of

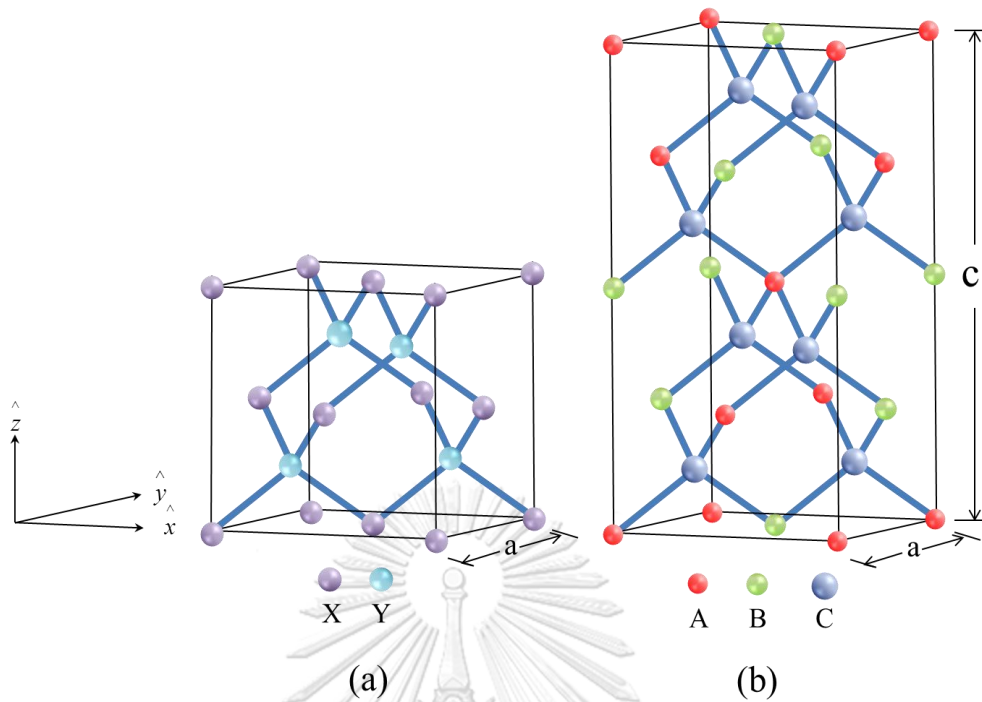


Figure 5: (a) sphalerite or zinc blend ($X = \text{Zn}$ atom (Cu or In) and $Y = \text{Se}$ atom) and (b) Chalcopyrite ($A = \text{Cu}$, $B = \text{In}$ and $C = \text{Se}$ atom [5]).

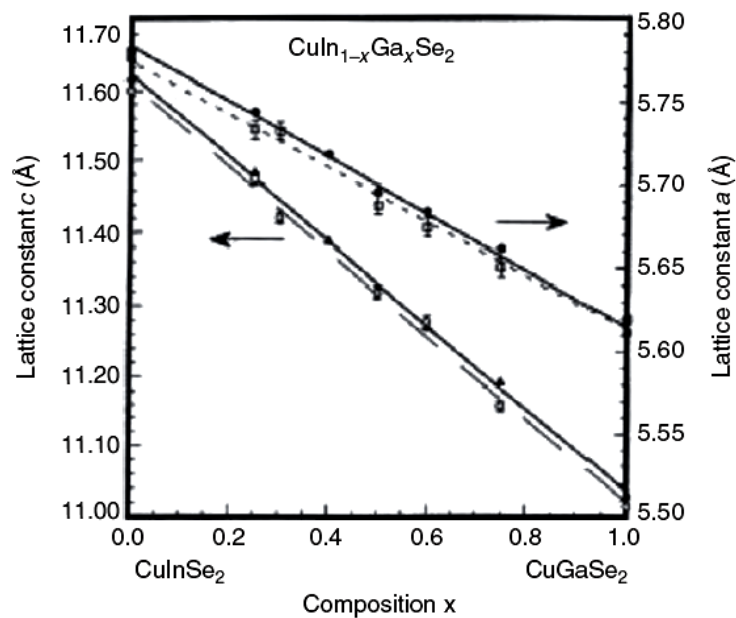


Figure 6: Lattice constant of a - and c -axis as a function of the composition parameter of x in the $\text{CuIn}_{1-x}\text{Ga}_x\text{Se}_2$ alloys ([36] and references therein).

lattice constants (a and c). Since, the atomic size of Ga is smaller than In, the unit cell size of CIS is decreased. The estimated lattice constants of a -axis and c -axis obey Vegard's law and the data are proportional to x composition or group-III atomic ratio, i.e., $x = [\text{Ga}]/([\text{Ga}]+[\text{In}])$, as shown in Fig. 6. These results agree with other researcher by the error of the lattice constants less than 0.001 \AA [36].

2.1.2 Phase Diagram of Cu-In-Ga-Se Material System

2.1.2.1 The Cu-In-Se Material system

The fundamental of Cu-In-Ga-Se system is similar to that of the Cu-In-Se system. The Cu-In-Se phase is closely related with the *pseudobinary* section between the Cu_2Se and In_2Se_3 compounds, and centered on the equimolar composition corresponding to CuInSe_2 , as illustrated in Fig. 7.

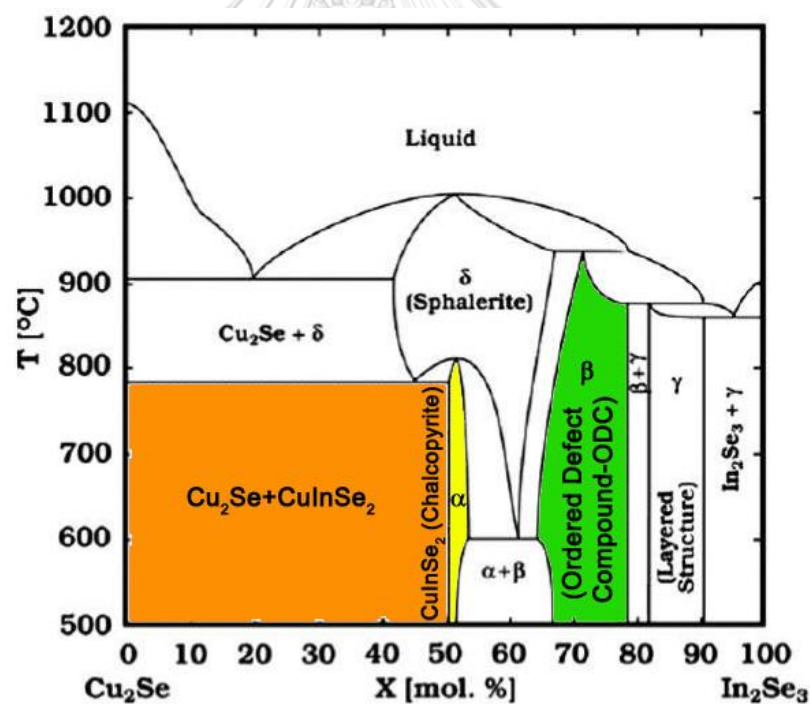


Figure 7: Phase diagram along the Cu_2Se - In_2Se_3 pseudobinary section of the Cu-In-Se material system ([37] and references therein).

The crystal structure of α -CIS phase is a adamantine chalcopyrite structure (yellow zone) as compared to δ -CIS and β -CIS, The δ -CIS phase is a sphalerite which is unstable at room temperature. The δ -CIS single phase exhibits a melting composition for 1005°C at 52.5 mol% of In_2Se_3 . The β -CIS phase such as $\text{Cu}_2\text{In}_4\text{Se}_5$ and CuIn_3Se_5 are also sometimes referred to “Ordered Defect Compounds” (ODCs) that have the Cu atomic ratio ($y = [\text{Cu}]/[\text{In}]$) of about 0.30 while γ -CIS is the persistence of a close packed lattice of Se atoms, i.e., CuIn_5Se_8 . However, the occurrence of In binary compound In_2Se_3 mixed with γ -CIS phase can be appeared along the Cu_2Se - In_2Se_3 pseudobinary section. The single phase chalcopyrite CIS will exist around 50.8-53.0 mol.% of In_2Se_3 (Cu at.% from 25.4 to 26.5), correspondingly, the Cu atomic ratio lies approximately between 0.97 and 0.88 as well as in the temperature range from room temperature to 780°C. The CuInSe_2 phase along Cu_2Se exists for $[\text{Cu}]/[\text{In}] \geq 1$, including the stoichiometric composition that has two-phase mixture of Cu-deficient α -CIS and Cu_{2-x}Se [37].

2.1.2.2 Defects in Cu-In-Se Material system

The defects that happen in the formation of this material system are induced by the composition of the atomic concentration. For the CIS material, it could be made either n- or p-type; p-CIS materials with low resistivity ($\rho \sim 0.5 \Omega\text{-cm}$) and high mobility of minority carriers ($\mu_e > 500 \text{ cm}^2\text{V}^{-1}\text{s}^{-1}$). By transforming p- to n-type, it is easily achieved by annealing CIS in vacuum or In-atmosphere because of *antisite defects*, e.g., In in Cu lattice sites (In_{Cu}) that is the *donor type defects* [38]. Based on the defect chemistry model of the nearly stoichiometric compound CIS; Rincon *et al.*[39] proposed the deviation of composition from the ideal formula CIS that could be described by two parameters, the *molecularity deviation* (Δm) and the *stoichiometry deviation* (ΔS). The first parameter explains the deviation of Cu and In compositions from the nominal CIS, as define in Eq. 2.1;

$$\Delta m = \frac{[\text{Cu}]}{[\text{In}]} - 1, \quad (2.1)$$

where $[\text{Cu}]$ and $[\text{In}]$ are the total atomic concentrations of Cu and In atoms, respectively. In the case of regular CIS, an excess of Cu compositions or Cu-rich gives $\Delta m > 0$, meanwhile an excess of In compositions, Cu-poor film gives $\Delta m < 0$.

Table 1: Majority defect pairs in CuInSe_2 under the excess In compositions with an excess or deficiency of selenium (ΔS) ([39] and reference therein).

Majority defect pair		Stoichiometry deviation (ΔS)
Acceptor	Donor	
V_{Cu}	In_{Cu}	<0
V_{Cu}	V_{Se}	<0
V_{Cu}	In_i	>0
Se_i	In_{Se}	>0
Se_i	In_i	>0

Table 2: Formation energies of intrinsic defects in CuInSe_2 ([39] and reference therein).

Types of defects	Formation energy (eV)	
Vacancies	V_{Se}	2.4
	V_{Cu}	2.6
	V_{In}	2.8
Interstitials	Cu_i	4.4
	In_i	9.1
	Se_i	22.4
Antisites	In_{Cu}	1.4
	Cu_{In}	1.5
	In_{Se}	5.0
	Se_{In}	5.5
	Se_{Cu}	7.5
	Cu_{Se}	7.5

Another parameter that describes the film composition whether there are more supplied ($\Delta S > 0$) or deficient ($\Delta S < 0$) selenium atoms is defined in Eq. 2.2;

$$\Delta S = \frac{2[Se]}{[Cu] + 3[In]} - 1, \quad (2.2)$$

where $[Se]$ is the total atomic concentrations of Se atoms. According to these parameters, the possible majority defect pairs which can be present under $\Delta m < 0$ are summarized in Table 1 and satisfied the defect activation energy (formation energy) in CIS given in Table 2, where the last two possibilities Se interstitials and In on Se lattice sites are less probable to form due to unfavorable high activation energy.

2.1.2.3 The Cu-Ga-Se Material System

The phase diagram of the Cu-Ga-Se material system has not been investigated widely in detail. However, in the earliest study, the Cu-Ga-Se phase was restricted to the *pseudobinary* $Cu_2Se-Ga_2Se_3$ section within the ternary phase field. The chalcopyrite phase of CGS is extended further towards Cu-poor composition (20.7% of Cu atomic content) that is lower than that in Cu-In-Se system, as illustrated in Fig. 8. The appearance of phases on the Cu-poor side is not less complicated than that of the Cu-In-Se system. The additional phases that exist in the phase diagram are $CuGa_3Se_5$, $CuGa_5Se_8$ and Ga_2Se_3 all of which correspond to disordered zinc blend (sphalerite) crystal structure.

Interestingly, from the phase diagrams, the melting point of $CuGaSe_2$ ($T_m \approx 1050-1030^\circ C$) is higher than that of $CuInSe_2$ ($T_m \approx 986^\circ C$). Investigating at the same temperature for the growing film, the lower T_{sub}/T_m ratio appears for the CGS structure. It is not wondering that growth of high-quality CGS films seems to be more difficult than growth of CIS films and thus leading to smaller CGS grain sizes.

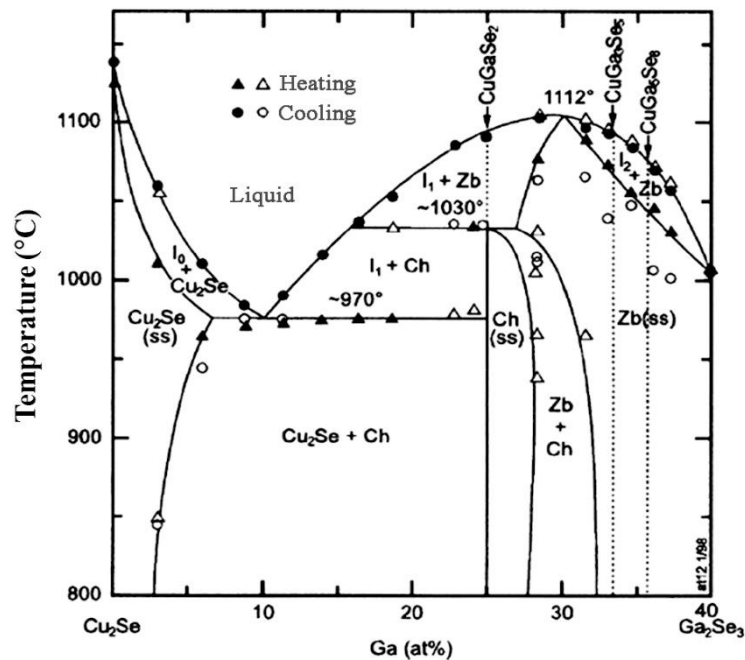


Figure 8: Phase diagram of Cu_2Se and Ga_2Se_3 for a formation of CGS compounds ([37] and references therein).

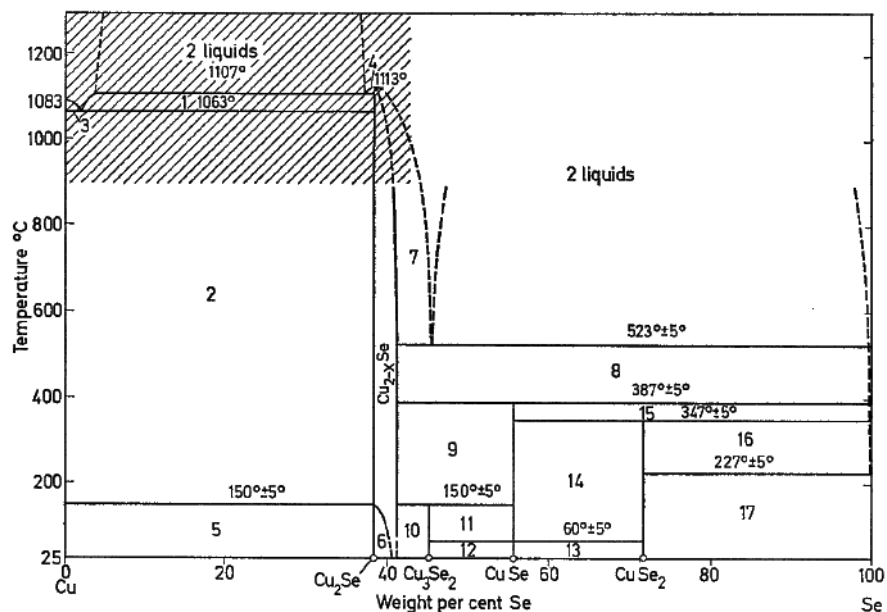


Figure 9: Phase diagram of the Cu-Se system above 25°C: (1) liquid+ β Cu_2Se ; (2) $\text{Cu}+\beta$ Cu_2Se ; (3) $\text{Cu}+\text{liquid}$; (4) liquid+ Cu_{2-x}Se ; (5) $\text{Cu}+\alpha$ Cu_2Se ; (6) α $\text{Cu}_2\text{Se}+\text{Cu}_{2-x}\text{Se}$; (7) $\text{Cu}_{2-x}\text{Se}+\text{liquid}$; (8) $\text{Cu}_{2-x}\text{Se}+\text{liquid}$; (9) $\text{Cu}_{2-x}\text{Se}+\text{CuSe}$ h.t.; (10) $\text{Cu}_{2-x}\text{Se}+\text{Cu}_3\text{Se}_2$; (11) $\text{Cu}_3\text{Se}_2+\text{CuSe}$ h.t.; (12) $\text{Cu}_3\text{Se}_2+\text{CuSe}$ l.t.; (13) CuSe l.t.+ CuSe_2 ; (14) CuSe h.t.+ CuSe_2 ; (15) CuSe h.t.+liquid; (16) $\text{CuSe}_2+\text{liquid}$; (17) CuSe_2+Se ; h.t.= high temperature; l.t.= low temperature [40].

2.1.2.4 The Cu-Se Material System

Cu-Se phase is frequently found in the Cu-rich ternary compound composition. It can exhibit in two types; Cu_{2-x}Se and Cu_xSe phases. By the investigation of the microstructure of CIGS grown with the 3-stage process, Cu_{2-x}Se has the cubic phase and resides on the surface and grain boundaries of CIGS structure when Cu atoms exceed stoichiometry. Cu_xSe has the tetragonal structure and resides along the CIGS grain boundary which is formed during the second stage [41]. The liquid Cu-Se phase appears at temperature exceeding 523°C (796K), which enhances CIGS grain growth by a vapor-liquid-solid growth mechanism by improving mobility of the constituent atoms in the liquid phase. At temperatures lower than the melting point, many Cu_xSe phases co-exist depending on the temperature and weight percent of Cu and Se, as illustrated in Fig. 9. At present, the role of Cu-Se phase on grain growth and atomic inter-diffusion (Cu, In and Ga) remains unclear, however, it is believed as a “quasi-liquid” phase that enhances high diffusivity of elements.

2.2 Optical Properties of CIGS Thin Film

2.2.1 Optical Absorption

When a semiconductor is illuminated with light, the photons may be absorbed or they may propagate through the semiconductor, depending on the photon energy and the band gap energy (E_g). Generally, if the photon energy ($h\nu$) is less than E_g , the photons are not readily absorbed. In this case, the light is transmitted through the material and the semiconductor appears to be transparent.

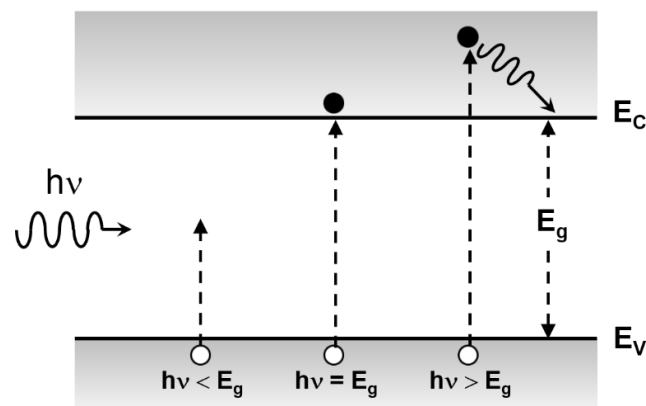


Figure 10: Optically generated electron-hole pair formation in a semiconductor.

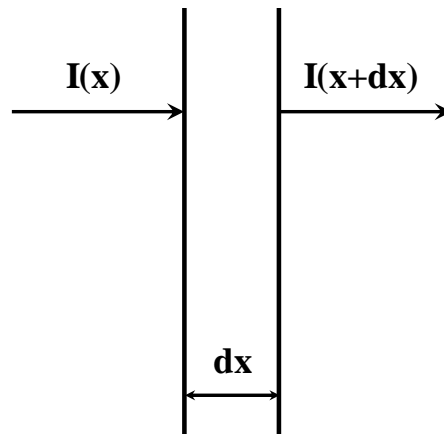


Figure 11: Optical transmission in a differential length.

If the photon energy is equal to or greater than E_g , the photon can interact with a valence electron leading to a transition of electron to the conduction band. This interaction creates an electron in the conduction band leaving a hole in the valence band, i.e., forming an electron-hole pair. The basic absorption processes for different values of $h\nu$ are shown in Fig. 10. When $h\nu > E_g$, an electron-hole pair is created and the excess energy may give the electron or hole additional kinetic energy, which will be dissipated as heat in the material.

Moreover, when light travels through semiconductors, the transmitted intensity of light decreases depending on the photon energy. An incident photon intensity at a position x and the emerging photon intensity at a distance $x+dx$ is shown in Fig. 11. The energy absorbed per unit time in the distance dx is given by

$$\alpha I(x)dx, \quad (2.3)$$

where α is the absorption coefficient of a material. The absorption coefficient is the relative number of photons absorbed per unit distance, given in unit of cm^{-1} .

From Fig. 11, we can write

$$I(x+dx) - I(x) = \frac{dI(x)}{dx} \cdot dx = -\alpha I(x)dx, \quad (2.4)$$

or

$$\frac{dI(x)}{dx} = -\alpha I(x). \quad (2.5)$$

If the initial condition is given as $I(0) = I_0$, then, the solution to the differential equation is

$$I(x) = I_0 e^{-\alpha x}. \quad (2.6)$$

The intensity of the photon decreases exponentially with distance through the material. If the absorption coefficient is large, the photons are absorbed over a relatively short distance.

The absorption coefficient in the semiconductor is a very strong function of photon energy and band gap energy. The absorption coefficient α plotted as a function of photon energy for several semiconductor materials is shown in Fig. 12 [42]. The absorption coefficient increases very rapidly for $h\nu > E_g$. The absorption coefficients are very small for $h\nu < E_g$, so the semiconductor appears transparent to photons in this energy range.

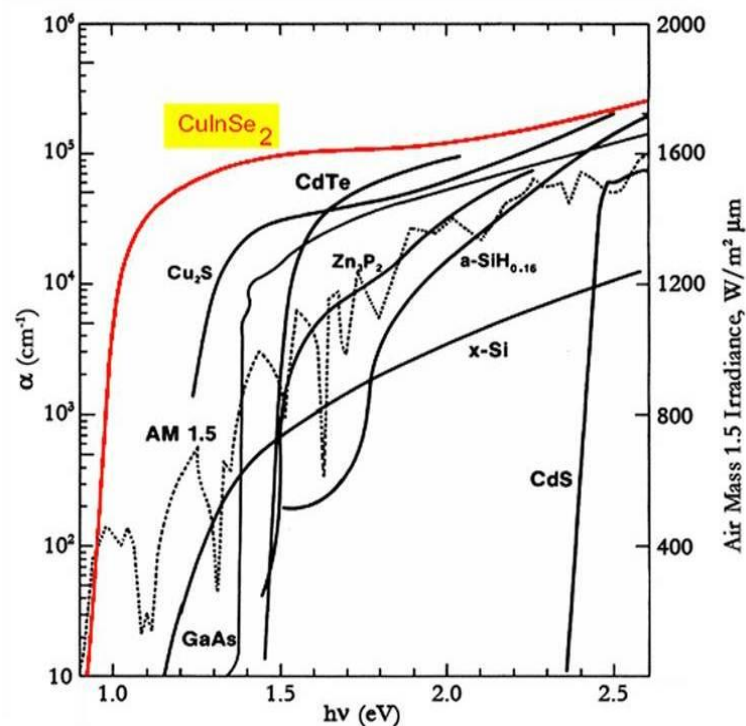


Figure 12: Absorption coefficient spectrum for various types of semiconductors [5].

There are several methods to determine the absorption coefficient (α). The transmission measurement as a function of wavelength is mostly used. It can be used to evaluate a refractive index, thickness (one or another) and band gap energy of semiconductor materials.

The optical band gap energy can be determined from the absorption coefficient that corresponds to a band-to-band transition. There are two kinds of transitions, i.e., direct and indirect in which one is allowed and another one is forbidden transition. The relation for the optical transition is given by

$$\alpha h\nu = A(h\nu - E_g)^y, \quad (2.7)$$

where A is a constant, $y = 1/2$ for direct allowed transitions, $y = 3/2$ for direct forbidden transitions, $y = 2$ for indirect allowed transitions and $y=3$ for indirect forbidden transitions [43]. The allowed transitions with $y=1/2$ are typically dominated the basic absorption process. Then, the direct band gap energy (E_g) of a semiconductor can be obtained using Tauc plot from the intercept of the extrapolation of a straight line on $h\nu$ axis for the plot of $h\nu$ and $(\alpha h\nu)^2$ [44-46].

In addition, the absorption coefficient (α) is determined by measuring the transmittance (T_{meas}) of normally impinging light. There is no universally accepted formula for its calculation. However, there are only three formulas that are used to estimate the absorption coefficient as the followings [43]

$$\alpha = -\frac{1}{d} \ln[T_{meas}], \quad (2.8)$$

or

$$\alpha = -\frac{1}{d} \ln \left[\frac{T_{meas}}{(1 - R_{meas})} \right], \quad (2.9)$$

or

$$\alpha = -\frac{1}{d} \ln \left[\frac{T_{meas}}{(1 - R_{meas})^2} \right], \quad (2.10)$$

where d is the sample thickness, T_{meas} is the measured transmittance of the sample and R_{meas} is the measured reflectance from the photon incident surface of the sample.

These formulas are approximation in applying any of them for a particular structure. In thin film materials, the absorption coefficient can be calculated from Eq. (2.10) due to multiple reflections and transmissions at both the top and bottom surfaces as shown in Fig. 13. The transmission coefficient (T) is defined as the ratio of transmitted to incident intensity, I_t/I_0 . If thin film has a thickness d , an absorption coefficient (α), and a reflectivity (R), the radiation traversing the first interface is $(1-R)I_0$, the radiation reaching the second interface is $(1-R)I_0e^{-\alpha d}$, and only a fraction $(1-R)^2I_0e^{-\alpha d}$, $(1-R)^2R^2I_0e^{-3\alpha d}$ and so on emerges; then

$$\begin{aligned}
 I_t &= (1-R)^2I_0e^{-\alpha d} + (1-R)^2R^2I_0e^{-3\alpha d} + (1-R)^2R^4I_0e^{-5\alpha d} + \dots, \\
 I_t &= I_0(1-R)^2e^{-\alpha d} [1 + R^2e^{-2\alpha d} + R^4e^{-4\alpha d} + R^6e^{-6\alpha d} + \dots], \\
 I_t &= I_0(1-R)^2e^{-\alpha d} [1 + (R^2e^{-2\alpha d}) + (R^2e^{-2\alpha d})^2 + (R^2e^{-2\alpha d})^3 + \dots]. \quad (2.11)
 \end{aligned}$$

Let $x \equiv R^2 e^{-2\alpha d}$ and use the Taylor's series,

$$f(x) = \frac{1}{1-x} = \sum_{n=0}^{\infty} x^n = 1 + x + x^2 + \dots, \quad (2.12)$$

then Eq. (2.11) becomes

$$T = \frac{I_t}{I_0} = \frac{(1-R)^2 e^{-\alpha d}}{1 - R^2 e^{-2\alpha d}}. \quad (2.13)$$

When the product αd is large, one can neglect the second term in the denominator; thus

$$T = \frac{I_t}{I_0} \approx (1-R)^2 e^{-\alpha d}, \quad (2.14)$$

then we obtain

$$\alpha = -\frac{1}{d} \ln \left[\frac{T_{meas}}{(1-R_{meas})^2} \right].$$

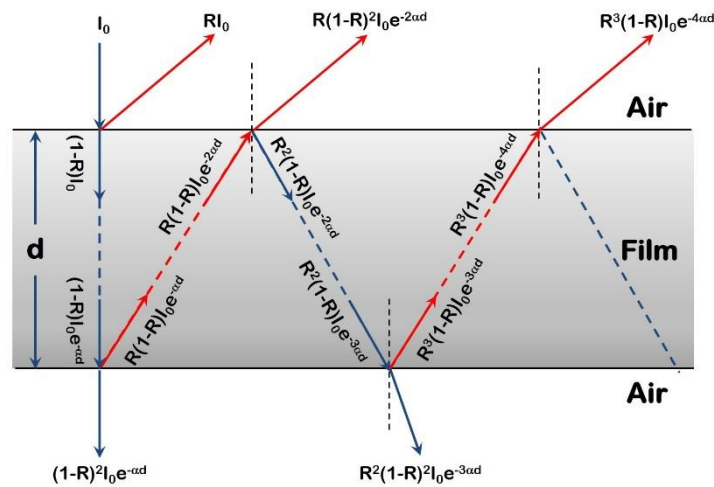


Figure 13: The multiple reflections and transmissions of thin film with film thickness d .

Furthermore, the estimated band gap of $\text{Cu}(\text{In}_{1-x}\text{Ga}_x)\text{Se}_2$ (CIGS) absorber thin films varies from 1.02 to 1.66 eV with increasing Ga contents among CuInSe_2 ($x = 0$, $E_g = 1.02$ eV) and CuGaSe_2 ($x = 1$, $E_g = 1.66$ eV). The variation of band gap with function of Ga or In composition in the $\text{Cu}(\text{In}_{1-x}\text{Ga}_x)\text{Se}_2$ grown by the 3-stage process shows 1.0, 1.14, 1.20, 1.40 and 1.60 eV for x values of 0.11, 0.29, 0.46, 0.76 and 1, respectively [47]. In term of x compositions, with increasing Ga content, the absorption edge moves toward shorter wavelength because of the increasing of Ga content in the CIGS films [34].

2.2.2 Photoluminescence Technique

Photoluminescence (PL) is a technique to detect and identify probable defect states in semiconductor materials. PL describes the photon emission processes after the material being irradiated with photons (usually ultraviolet or visible laser). It relies on the creation of electron-hole pairs by incident radiation and subsequent radiative recombination photon emission. Photons of a particular energy that are absorbed or emitted by a sample provide evidence of electronic states differing by that energy within the band gap. The radiative emission intensity is proportional to impurity density [48].

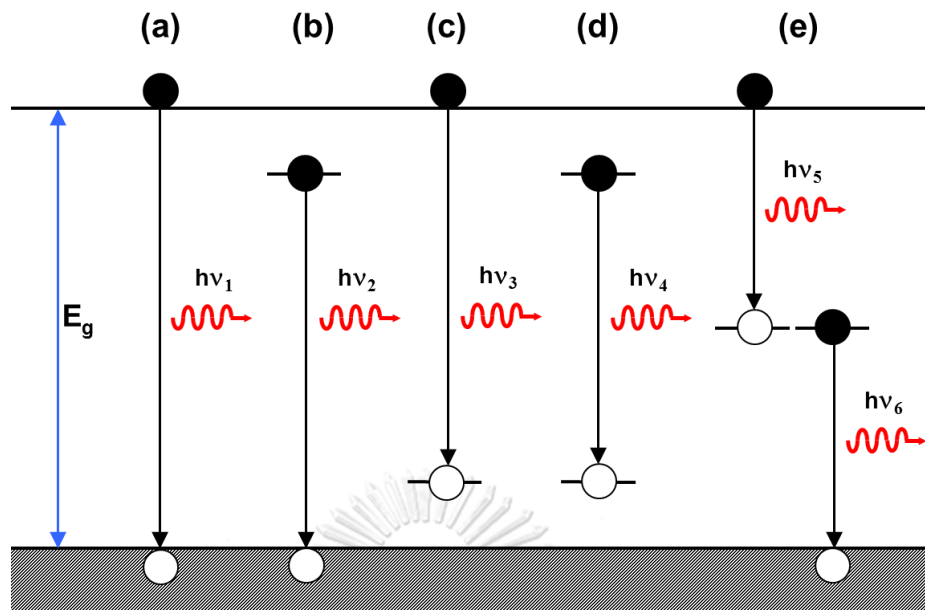


Figure 14: Radiative recombination paths: a) interband transition, b) donor to valence band transition, c) conduction to acceptor band transition, d) donor to acceptor band transition and e) conduction to intermediate band or intermediate to valence band transition.

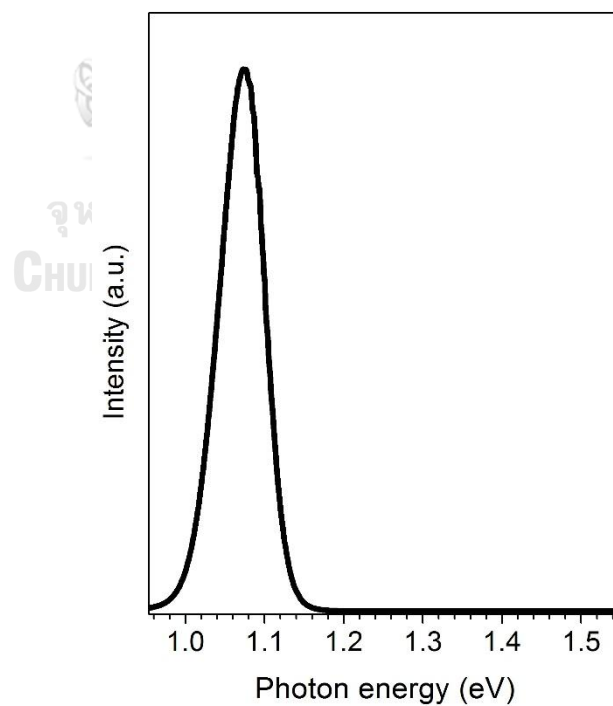


Figure 15: The PL broad spectrum due to the variety of Coulomb's interaction distances.

Depending on the defect or impurity, the state forms as a donor or acceptor of excess electrons or holes in the crystal. Electrons or holes are attracted to the excess or deficiency of local charge due to the impurity nucleus or defect, and thus Coulomb binding occurs. Fig. 14 shows a simplified sketch of the tentative PL recombination paths for intrinsic and impurity transitions. When the temperature is sufficiently low, carriers will be trapped at these states. If these carriers recombine radiatively, the energy of the emitted light can be analyzed to determine the energy of the defect or impurity level as shown in Fig. 14. Shallow levels that lie near the conduction or valence band edge are more likely to participate in radiative recombination; however, the sample temperature must be small enough to discourage thermal activation of carriers out of the traps. Deep levels tend to facilitate non-radiative recombination by providing a stop-over for electrons making their way between the conduction and valence bands by emitting phonons.

When the sample temperature is decreased from room to low temperature or conversely in PL measurement, the thermal activation energy of the defect state for the emission peak corresponds to

$$\frac{I_T}{I_0} = \frac{1}{[1 + C \exp(-\Delta E) / k_B T]}, \quad (2.15)$$

where I_T is the intensity of photoluminescence peak at temperature T , I_0 is the radiative intensity at $T = 0$ K, k_B is the Boltzmann's constant (1.38×10^{-23} J/K), C is a constant and ΔE is the thermal activation energy of the donor or acceptor.

In the case of donor-acceptor pair (DAP) transition in the semiconductor materials, the activation energy levels of the donor and acceptor can be written by

$$h\nu = E_g - (E_D + E_A) + \frac{e^2}{4\pi r \epsilon_0 \epsilon_r}, \quad (2.16)$$

where E_g is the band gap energy, E_D and E_A are the donor and acceptor ionization energies, respectively. The last term corresponds to the Coulomb's interaction between the pair, r is the distance between the donor and acceptor that involves in the transition, ϵ_r and ϵ_0 are the dielectric constant of the vacuum and material. When r is small, individual pair line may be observed. When r becomes larger, the emission

usually merges into a broad band as shown in Fig. 15. The peak energy of the broad band corresponds to the suitable separation of the pair.

The transition from donor levels to valence band or acceptor levels to conduction band can be related to

$$h\nu = E_g - E_{D,A} + k_B T, \quad (2.17)$$

where $E_{D,A}$ represents the activation energy of either donor (D) or acceptor (A). This is known as the free to bound transition (FB). It can be referred to a free electron recombines with a hole bound to an acceptor or a free hole recombine with a donor bound to an electron.

2.3 Photovoltaic Devices

2.3.1 P-N Junction of a Solar Cell

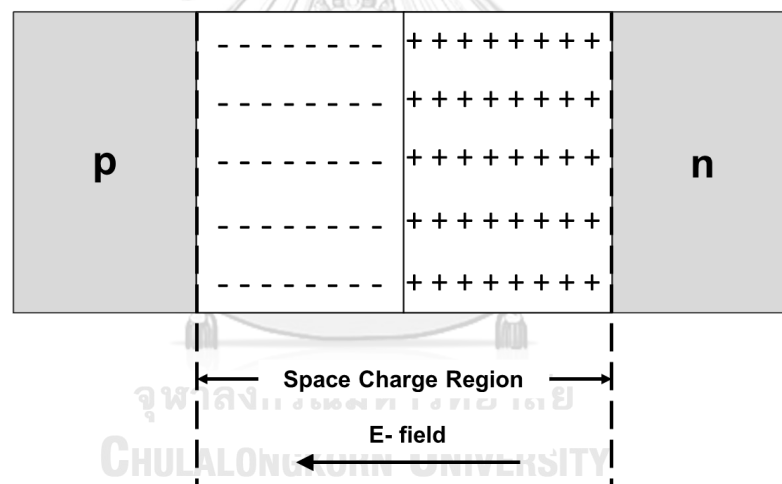


Figure 16: The structure of the p-n junction with the space charge region (SCR) and the electric field due to the charged carriers.

When a p-type and an n-type semiconductors are brought in contact with one another, they form a p-n junction. In other words, one region is doped with acceptor impurity atoms to form the p region and the adjacent region is doped with donor atoms to form the n region as shown in Fig. 16. There is a very large density gradient in both electron and hole concentrations. Majority carrier electrons in the n region will begin diffusing into the p region, and majority carrier holes in the p region will begin diffusing into the n region. As electrons diffuse from the n region, positively charged donor atoms are left behind. Similarly, as holes diffuse from the p

region, they uncover negatively charged acceptor atoms. The net positive and negative charges in the n and p regions induce an electric field in the region near the p-n junction, in the direction from the positive to negative charge, or from the n to p region.

The net positively and negatively charged regions are referred to as the space charge region (SCR). Essentially, all majority charge carriers are swept out of the SCR by the electric field except for minority charge carriers. Since the space charge region is depleted of any mobile charge, this region is also referred to as the depletion region, where the *built-in potential barrier* (V_{bi}) is created in order to maintain the equilibrium between majority carrier electrons in the n region and minority carrier electrons in the p region, and also between majority carrier holes in the p region and minority carrier holes in the n region [49]. In this work, CIGS is the p-type semiconductor while CdS is the n-type counterpart.

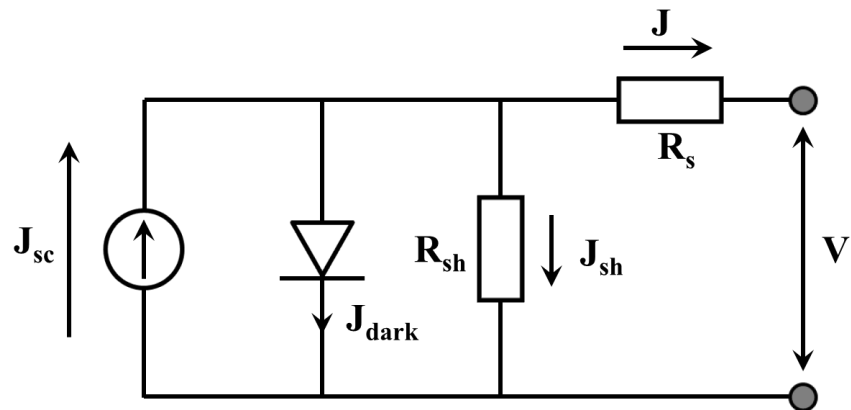
2.3.2 The Equivalent Circuit and Characteristic of Solar Cell

A solar cell is a p-n junction device with no voltage directly applied across the junction. It converts photon energy into electrical energy that can deliver to a load. Important parameters of a solar cell are short-circuit current density (J_{sc}), open-circuit voltage (V_{oc}), fill factor (FF) and the power conversion efficiency (η).

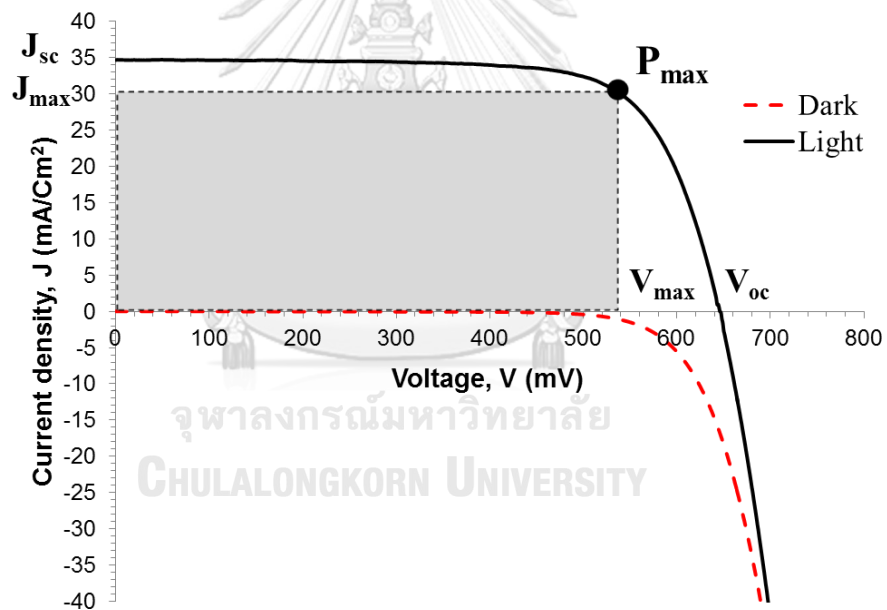
Without illumination, the dark current of p-n junction is given by the ideal Shockley diode equation

$$J_{dark}(V) = J_0(e^{qV/k_B T} - 1), \quad (2.18)$$

where J_{dark} is the dark current density, J_0 is the reverse saturation current density (constant), q is the electrical charge, V is the applied bias voltage, k_B is the Boltzmann's constant (1.38×10^{-23} J/K) and T is the temperature of the device [50].



(a)



(b)

Figure 17: (a) Equivalence circuit of solar cell and (b) J-V characteristics of a p-n junction solar cell.

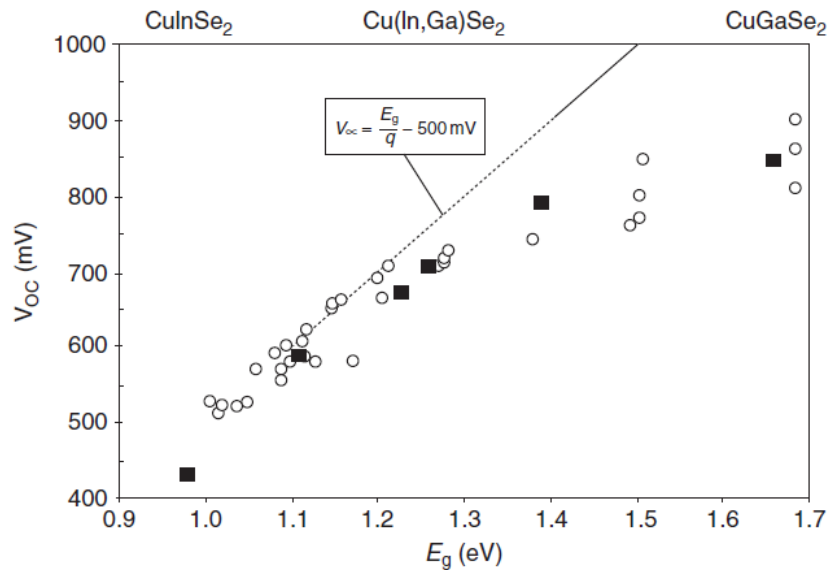


Figure 18: A plot of open-circuit voltage (V_{oc}) and band gap energy (E_g) for various Ga compositions of CIGS thin film solar cells [8].

Under illumination, even with zero voltage bias ($V=0$) applied to the junction, an electric field exists in the space charge region. Incident photon can create electron-hole pairs in the space charge region that will be swept out producing the photocurrent (J_L) or the short-circuit current density (J_{sc}) in the reverse-biased direction that has an opposite of the dark current (J_{dark}) direction. Then, the net p-n junction current, in the reverse-biased direction is

$$J(V) = J_{sc} - J_{dark}(V) = J_{sc} - J_0(e^{qV/k_B T} - 1). \quad (2.19)$$

Practically, the loss current and voltage of the device depends on the contact resistance and the leakage current. Fig. 17(a) shows the equivalent circuit of a solar cell that consists of two resistances, i.e., the series resistance (R_s) and shunt resistance (R_{sh}). The series resistance is the overall resistance of the solar cell and the shunt or parallel resistance (R_{sh}) refers to the leak path or tunneling pathways at the p-n junction. The leakage current increases with the decreasing of the shunt resistance. These two resistance parameters can describe the quality of the p-n junction which low R_s and high R_{sh} are required for the solar cells. Therefore, the equation that includes the resistances is

$$J = J_{sc} - J_0(e^{q(V+JR_s)/k_B T} - 1) - \frac{V + JR_s}{R_{sh}}. \quad (2.20)$$

The open-circuit voltage (V_{oc}) is acquired under the condition $J = 0$, $R_s \rightarrow 0$ and $R_{sh} \rightarrow \infty$. Then, Eq. (2.20) can be rewritten as

$$V_{oc} = \frac{k_B T}{q} \ln\left(\frac{J_{sc}}{J_0} + 1\right). \quad (2.21)$$

Additionally, in the experiment on various CIS, CIGS and CGS devices, it has been found that the V_{oc} increases linearly with increasing band gap energy (E_g) up to certain point before it becomes nonlinear as shown in Fig. 18 [8]. This corresponding linear equation is

$$V_{oc} = \frac{E_g}{q} - 0.5. \quad (2.22)$$

Finally, a plot of the diode current density J as a function of the diode voltage V (J-V characteristic) is shown in Fig. 17(b). The fill factor is defined as the ratio of maximum power delivered by the device to the product of J_{sc} and V_{oc} that is

$$FF = \frac{J_m V_m}{J_{sc} V_{oc}}, \quad (2.23)$$

where J_m and V_m are the current-density and voltage corresponding to the maximum power point, respectively. FF is one of the parameters that can predict the stability of solar cell. The low efficiency solar cell leads to poor FF . The high series resistance and low shunt resistance also cause low FF in the solar cells. Typically, the fill factor is between 0.7 and 0.8.

The conversion efficiency (η) of a solar cell is defined as the ratio of output electrical power to incident photon power (P_i). For the maximum power output (P_m), we can write

$$\eta = \frac{P_m}{P_i} \times 100\% = \frac{J_m V_m}{P_i} \times 100\% = \frac{J_{sc} V_{sc} FF}{P_i} \times 100\%. \quad (2.24)$$

2.4 Growth Process of CIGS Thin Films

2.4.1 Co-Evaporation Process

The most prosperous method for CIGS fabrication to yield highest efficiencies to date is the co-evaporation from elemental sources in single or sequential process. Slightly Cu-deficiency around 10% ($y \approx 0.9$) with group-III element concentration of 30-40% ($x \approx 0.3-0.4$) is required for the best cell performances. This process needs a maximum substrate temperature reaching to about 500–600°C during a part of the deposition process. The composition of the deposited elements corresponds to their evaporation rates. During the film growth, a Cu-rich stage is also required in order to enhance large grains growth that are more favorable for electronic properties. Se is usually over supplied in co-evaporation process in order to minimize Se vacancies in CIGS film. Then, Se is usually maintained during the growth and cooling down of the films. The co-evaporation processes for CIGS thin films may be classified as the followings.

2.4.1.1 Single-Stage Process

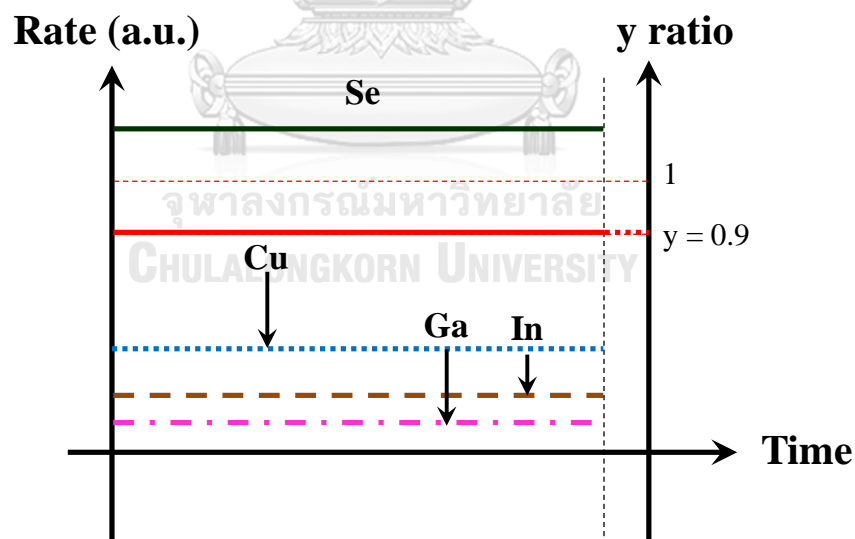


Figure 19: Schematic of the growth profile rate and Cu composition ratio (y) for single-stage deposition.

The single-stage process is the most basic co-evaporation process to deposit CIGS thin films evaporating all elements simultaneously in one step. Substrate temperature and elemental fluxes are constant until end of the process with pre-defined composition. The growth profile for this method is shown in Fig. 19. The CIGS thin films obtained by this single-stage process have more amounts of triangular-shaped grains as well as some tiny holes between the grains on surface. The grain size is relatively smaller compared with other processes [51].

2.4.1.2 Two-Stage Process

The 2-stage process is generally known as “bilayer process” or “Boeing recipe” or noted as CURO (Cu-rich then Cu-off) process. The Cu-rich growth phase is realized by excess of Cu during the first stage in order to get a large grain growth. The second stage is followed by In and Ga surplus without Cu flux to convert to Cu-poor composition ratio (y) around 0.9. The substrate temperature is high and constant in both stages. Se flux is also oversupplied throughout the process. During the change in film composition, there is the idea that the hole concentration of the film is abruptly changed at the stoichiometric composition while the film composition gradually changed from Cu-rich to Cu-poor composition. Then, the real-time monitoring method of Cu-atomic ratio is introduced to detect the end-point deposition process [52, 53]. The obtained CURO films have large grains, but a rough surface with crevices between the grains. The transport of Cu from Cu_xSe during the first stage is segregated in the grain boundaries and subsequently consumed during the second stage [54]. The growth profile and composition evolution of the films in two-stage process is illustrated in Fig. 20. The relationship of Cu-atomic ratio and deposition time process as

$$y(t_1) \cdot t_1 = y(t_2) \cdot t_2, \quad (2.25)$$

where $y(t_1)$ is the required composition at the growth process time t_1 and $y(t_2)$ is the final desired composition at the end of the growth process time t_2 that detected by the *in-situ* monitoring.

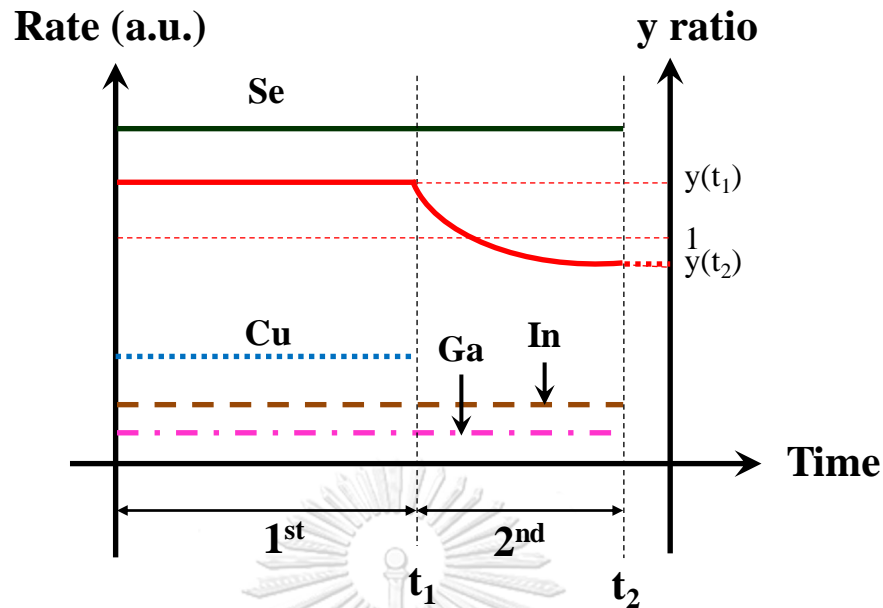


Figure 20: Schematic of the growth profile rate and Cu composition ratio (y) for the 2-stage deposition.

2.4.1.3 Three-Stage Process

The 3-stage process is by far the method to achieve the highest solar cell efficiency for CIGS. It follows by three deposition steps. In-Ga-Se precursor layer is first deposited onto low heated (250–400°C) Mo coated SLG glass substrates to form an $(\text{In,Ga})_2\text{Se}_3$ phase. Then, followed by evaporation of Cu and Se at higher substrate temperature (550–600°C) for a small time period until the overall composition is Cu-rich film ($y > 1$). Cu atoms are diffusing into $(\text{In,Ga})_2\text{Se}_3$ and grain growth is taking place by recrystallization. Again, In-Ga-Se contents are co-evaporated at the same high substrate temperature in the third stage until the required composition is Cu-deficiency with $y \approx 0.9$. The co-evaporation profile is given in Fig. 21. Cu-atomic ratio and deposition time at 1st and 2nd stages are corresponded to Eq. (2.20) while Cu-atomic ratio and deposition time at 3rd is related to Eq. (2.25)

$$\frac{y(t_1)}{t_1} = \frac{y(t_2)}{t_2}, \quad (2.26)$$

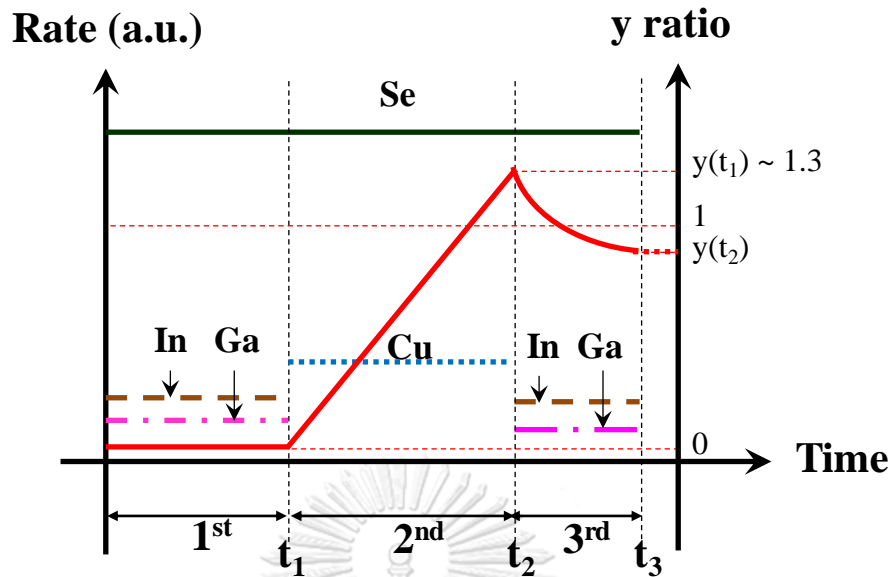


Figure 21: Schematic of the growth profile rate and Cu composition (y) for the 3-stage deposition.

Although, the 2-stage process is done by the Cu-poor composition that resembles to the 3-stage process. The final film morphologies are different between the 2- and 3-stage processes. The films for the 2-stage process show larger grains and larger surface roughness, because the nucleation takes place under Cu-rich composition with Cu_xSe secondary phase. Oppositely, the Cu-rich at the 2nd stage in the 3-stage process results in a recrystallization of small grained from the 1st stage and then produce large grains with small surface roughness. Rougher surface has an effect on thin buffer layer coverage and risk to sputter damage during window layer deposition. Then, the *in-situ* spectroscopic light scattering has been reported for surface roughness. The reduction of surface roughness is found in the end of Cu-rich stage and the Cu-poor stage, 2nd and 3rd stages, respectively [55].

2.4.2 Reaction Deposition and H_2Se Selenization

The reaction deposition technique is more popular for a large-scale CIGS absorber production. However, the uniformity of absorber film is one of the problems for this technique. Generally, the reaction process is separated into two or more different processing steps. A stack of precursor layer is deposited first. These layers can be metal layers, alloys, or complete compounds typically deposited without substrate heating. Then, the precursor is passed to a thermal reaction step in order to

complete the semiconductor film. The selenization of metallic Cu-In-Ga precursors is most deposited by sputtering from multi-sputtering sources under Se or H₂Se atmospheres. The sequential RF sputtering (In,Ga)₂Se₃ and CuSe targets that is followed by annealing in Se vapor showed higher efficiency of 13.6% by comparing to CIGS solar cell sputtering from a quaternary CIGS target of 9–11% [56, 57]. The sequential deposition for CIGS film causes smoother surface, better crystallinity and more compact structure of CIGS film.

2.5 CIGS Band Gap Profiling Techniques

The band gap energy is one of the important factors in achieving maximum conversion efficiency for the p-n hetero-junction solar cells. The CIGS absorber has a direct band gap with high optical absorption coefficient. In order to improve the CIGS solar cell performance, the electronic and optical properties of the cell have to be optimized. In this section, the types of CIGS band gap profiling are reviewed in their benefit and unfavorable effect compared with non-graded band gap.

2.5.1 Non Band Gap Grading

Formerly, a constant band gap of the CIGS thin film solar cell was usually obtained from the single-stage and two-stage or even three-stage growth process with a constant $x = [\text{Ga}]/([\text{Ga}]+[\text{In}])$ concentration ratio. The conduction band has a constant energy level throughout the CIGS film thickness as shown in Fig. 22(a). However, electrons that are excited to the conduction band are possibly recombined before they are sweep across the junction. Then, the short circuit current density (J_{sc}) and open circuit voltage (V_{oc}) are both less than they should be.

2.5.2 Normal Band Gap Grading

In the earlier as 1960, Wolf suggested the improvement of photovoltaic devices by the modification of band gap energy as graded band gap in absorber semiconductor [58]. This application enhances quasi-drift electrical field or back surface field in the *space charge region* (SCR), then, the conversion efficiency can be improved. Fig. 22(b) shows a normal band gap grading; the conduction band increases gradually towards the Mo back contact as Ga content increases. The Ga gradient produces a gradient in the electron affinity that is related to a quasi-electrical field. The diffusion

length of the electrons can be enlarged and then supported more carrier collection. Moreover, widening the band gap near the back contact region leads to a lower recombination current. In fact, for thick CIGS films about 1.5–2.0 μm , with an increased Ga composition ratio (x) towards the back contact can improve the efficiency of around 0.4% units. Increasing J_{sc} due to an improved carrier collection at long wavelengths is the main consequence. There is no significant gain either V_{oc} or FF [59, 60]. Similarly, the back Ga-graded CIGS film for modified 2-stage profile shows only higher J_{sc} and then enhances solar cell efficiency of 0.3% compared with 2-stage profile [61].

2.5.3 Double Band Gap Grading

There is the reverse band gap grading which is linearly decreasing band gap towards the back contact that results in the increasing of the recombination rate at the back contact. However, the V_{oc} is high at the SCR owing to widened band gap and lower recombination rate. In double grading profile, the Ga content increases towards the front CIGS surface with an optimum distance and then increases to the back contact as shown in Fig. 22(c). Front grading repels minority carriers away from the interface and reduces the recombination rate, and then V_{oc} increase, and back grading increases the band gap that enhances the carrier collection by drifting the carriers to the SCR by the additional electric field. As a result, the quantum efficiency response is improved at long wavelengths and enhances J_{sc} . By adjusting an appropriate Ga content for the three-stage growth process, it can allow the double graded profile [59]. Additionally, Na also plays an important role to the diffusion of Ga and In during the film growth [17, 62]. Then, the double Ga graded phenomena was also observed via a NaF precursor before grown CIGS film [63] and NaF during Cu and Se evaporation at 2nd stage for the three-stage growth process [64].

2.5.4 Valence Band Offset

The downward valence band shift at the surface region has been automatically observed on Cu-poor CIGS surface by $\text{Cu}(\text{In,Ga})_3\text{Se}_5$ (135-CIGS) phase [20]. Many theoretical and experimental researches notified that the valence band offset is effective on the solar cell parameters, especially V_{oc} that is improved by enlarging the high barrier for holes at interface. In fact, the recombination easily takes place at the

interface by the condition of $p = n$ (high defect zone). Then, the 135-CIGS defect surface layer can cause a shift of the regime $p = n$ into the absorber and then stay away from the rich defect zone at CdS/CIGS interface. The band diagram for valence band offset is shown in Fig. 22(d). Gorji *et al.* proposed the effects of the valence band offset at the CIGS surface and proved that the valence band enlarging improved the solar cell parameters with the exception of J_{sc} by reducing the recombination rate at the surface regions as shown in Fig. 22(d). A larger valence band offset less than 0.4 eV can create a sufficient barrier to eliminate interface recombination.

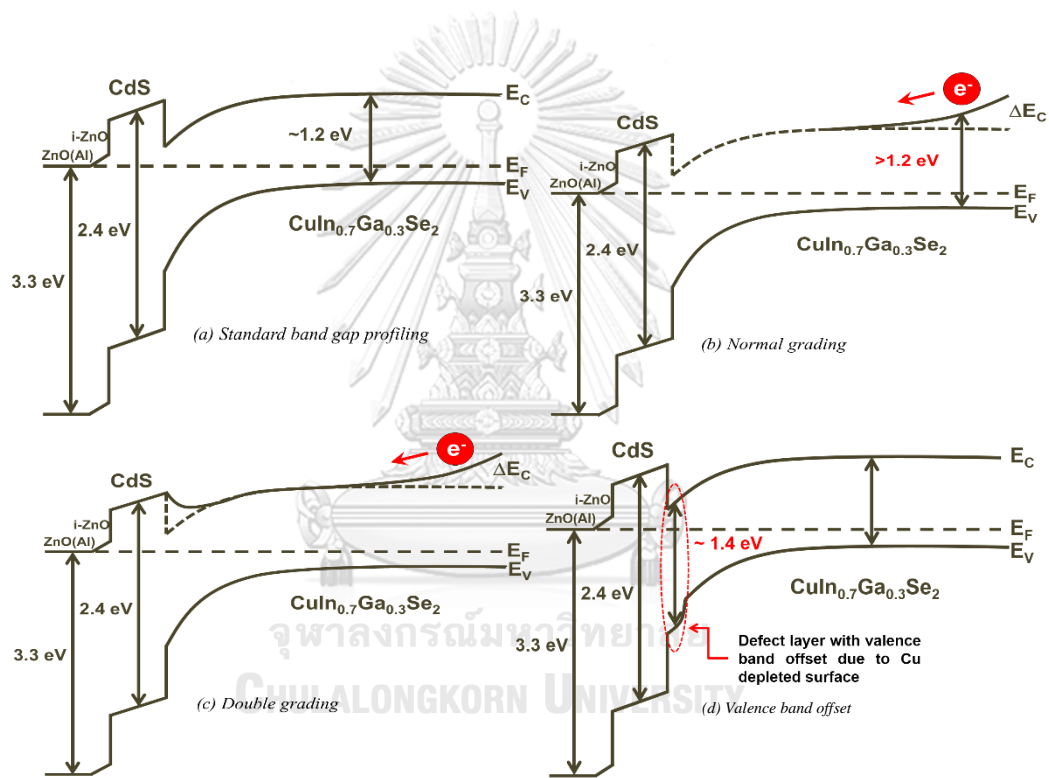


Figure 22: Band gap profiles in CIGS thin film solar cell (a) standard band structure, (b) normal grading, (c) double band gap grading and (d) valence band offset.

CHAPTER III

FABRICATION AND CHARACTERIZATION OF Cu(In,Ga)Se₂ AND Cu(In,Ga)₃Se₅/Cu(In,Ga)Se₂ THIN FILM SOLAR CELLS

The important step for preparation the sample for the vacuum process is the substrate cleaning. Then, the detail of SLG substrate cleaning process before the film growth will be presented first. Next, the growth details of the 112-CIGS and 135-CIGS absorber layers via the molecular beam deposition (MBD) technique are explained to the calibration of the molecular constituents for obtaining the desired film composition and thickness. The absorber for the solar cell devices will be passed through the multi-layer for solar cell fabrication process until reaching the J-V characteristic and QE measurements. Finally, the analyzed equipment for the CIGS absorber layer and CIGS thin film solar cells are briefly described in their methods and basic principles.

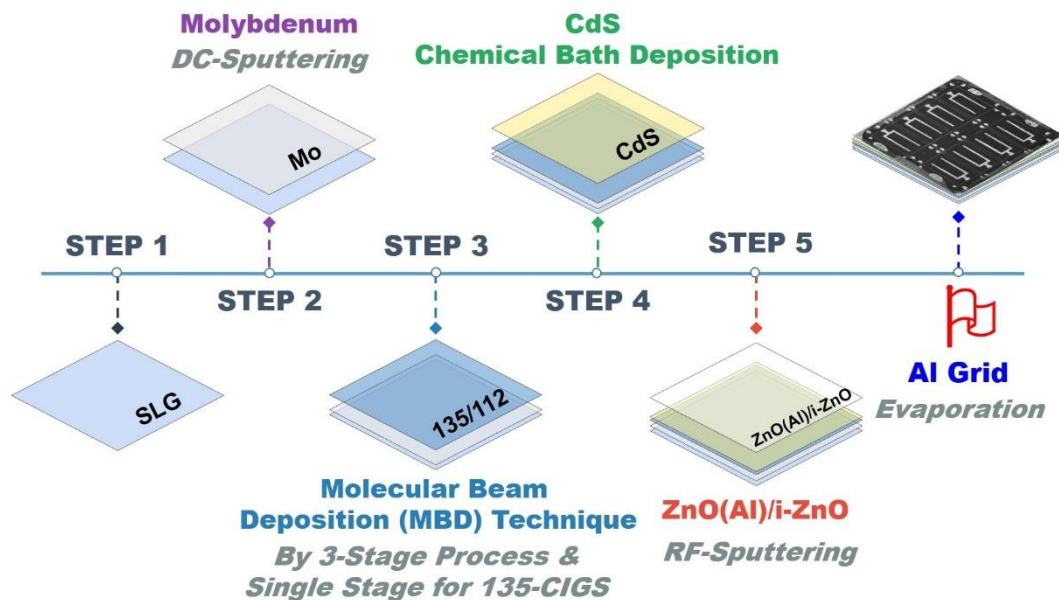


Figure 23: The schematic of 135-CIGS/112-CIGS solar cell fabrication.

3.1 CIGS Solar Cell Fabrication

3.1.1 Soda-Lime Glass (SLG) Substrate Cleaning Procedures

In order to obtain sufficiently clean surface for vacuum purposes, the SLG substrate should be thoroughly cleaned even if it is perfectly transparent. SLG is a typical and suitable substrate for CIGS thin film solar cells. It acts as the Na reservoir as shown in Table 3 to enhance CIGS solar cell performance as well as the CIGS texture [65]. It also has a well-matched thermal expansion coefficient ($9-10 \times 10^{-6} \text{ K}^{-1}$) [16] as shown in Table 4. The cleaning steps are as followed [66]:

1. Immerse the SLG substrates in deionized (DI) water ($\sim 18.3 \text{ M}\Omega\text{-cm}$) with dishwashing detergent at least one hour in order to remove grease from the surface.
2. Thoroughly scrub the SLG substrates with a cellulose sponge and clean with DI water.
3. Immerse the SLG substrates in an ultrasonic bath with a mixture of the glassware detergent (Micro-90) and DI water at 60°C for an hour, and rinse with DI water.
4. Immerse the SLG glass in the usual cleansing known as chromic acid (H_2CrO_4) for an hour in order to create the rough surface before depositing film. The chromic acid contains a saturated aqueous sodium dichromate in a litre of concentrated sulfuric acid. Then, rinse the SLG with DI water.
5. Thoroughly immerse the SLG substrates again in DI water using an ultrasonic bath.
6. Dry the washed glass with compressed nitrogen gas and keep in a dry cabinet before loading into the vacuum chamber in the next step.

Table 3: Soda-lime glass compositions.

Composition	Typical container Glass (%)
SiO ₂	74.42
Al ₂ O ₃	0.75
MgO	0.30
CaO	11.27
Li ₂ O	0.00
Na ₂ O	12.90
K ₂ O	0.19
Fe ₂ O ₃	0.01
TiO ₂	0.01
SO ₃	0.16

Table 4: Thermal expansion coefficients of substrate materials.

Material	CTE (10 ⁻⁶ K ⁻¹)	T _{Sub} (max) (°C)	Notes
SLG	9 (20-300°C)	≈ 600	Standard glass substrate
Corning 7059	4.6	> 600	Alkali-free glass
Mo	4.8-5.9 (20-600°C)	> 600	Adhesive layer
Al ₂ O ₃	6-8	> 600	Insulating layer and/or blocking Na
CuInSe ₂	11.2-11.4		c-axis
CuGaSe ₂	13.1		c-axis

3.1.2 Mo Back Contacts

Mo is the most widely used contact material for CIGS thin film solar cells because of its comparatively low cost, high electrical conductivity, high melting point (2700°C) and low diffusivity in the semiconductor films.

Mo layer is the first thin film layer deposited on the SLG substrates. The Mo layer is deposited for the thickness ~600 nm by DC magnetron sputtering using a 4-

inch diameter Mo target with a sputtering power of 575W for 12 minutes by rotating the samples of 3 rounds per minute (rpm). Argon atmosphere is controlled at 6×10^{-3} mbar. The distance between the substrate holder and the target is approximately 6 cm.

In humid air, the Mo can be oxidized. This is particularly critical for a decrease in conductivity and possibly loss fill factor. The optical transparent can be seen for a completely oxidized Mo films. Next, the sputtered Mo films are kept in a desiccator.

3.1.3 Cu(In,Ga)Se₂ and Cu(In,Ga)₃Se₅ Absorber Layers

3.1.3.1 Molecular Beam Epitaxy System

(1) The MBE System

Molecular beam epitaxy (MBE) was established as a technology of great potential for the fabrication of high quality epitaxial semiconductor films with the ability of atomic layer growth. To avoid contaminations, high purity materials and ultra-high vacuum (UHV – base pressure $\sim 10^{-10}$ Torr) are required for a long mean free path of the atoms or molecular beam directional flow. The epitaxial film is achieved through the chemical reaction of multiple molecular beams which originate from evaporation or sublimation of elements or sources that are kept in separate effusion cells or *Knudsen cell* (K-cell), as schematically illustrated in Fig. 24. Each K-cell consists of pyrolytic boron nitride (PBN) crucible housed with tantalum (Ta) heater wire with layers of molybdenum (Mo) radiation shield in order to secure temperature uniformity. The temperature of the heated source is measured by type K (NiCr-NiAl) and type C (W5%Re-W26%Re) thermocouples for low (0°C–275°C) and high (-270°C–1,260°C) temperature, respectively, and stable source temperature is assured by proportion-integral-deviation (PID) programmable controller.

Molecular beam epitaxial system (EIKO model EW-100) is used for this work either polycrystalline or single crystalline epitaxial bilayer thin films. The system comprises two main parts:

(a) Growth Chamber consists of

- Evaporation sources or K-cells with thermal isolating shutters; Copper (Cu), Indium (In), Gallium (Ga) and Selenium (Se) elements,
- A heated substrate rotation holder,
- In-situ analysis UHV equipment; a residual gas analyzer (RGA), a quartz crystal thickness monitor (QCM), a beam flux monitor, a reflection high energy electron diffraction (RHEED) and a pyrometer,
- Vacuum gauges; pirani gauge (1.3×10^2 – 1.3×10^{-1} Pa) and nude ionization gauge (10^{-3} – 10^{-11} Torr),
- A turbo molecular pump with a rotary backing pump (corrosion resist grade),
- Titanium sublimation pump (TSP) for ultra-high vacuum.

(b) Loadlock chamber

A loadlock chamber is a vacuum chamber that is used to exchange a specimen with the growth chamber in order to keep the vacuum and reduce a contamination the main chamber. Without an exposure of the main vacuum growth chamber to atmospheric pressure for substrate exchange, it is the also an advantage for improving the crucible life-time as well as the ultimate film purity level. The components of the load-lock chamber are

- Vacuum gauges; pirani gauge (1.3×10^2 – 1.3×10^{-1} Pa) and nude ionization gauge (10^{-3} – 10^{-11} Torr),
- A turbo molecular pump with a rotary backing pump (regular grade),
- A substrate holder,
- A transfer rod for specimen exchange with the main growth chamber.

(2) UHV Analysis Equipment**(a) Residual Gas Analyzer (RGA)**

A residual gas analyzer (RGA) is operated based on the quadrupole mass spectrometer (QMS) for analyzing the contamination and residual gas such as H₂, O₂, H₂O, N₂ and hydrocarbon compounds, etc. in the vacuum systems. The instruments measuring the partial pressure of the residual gases are basically ionization gauges in

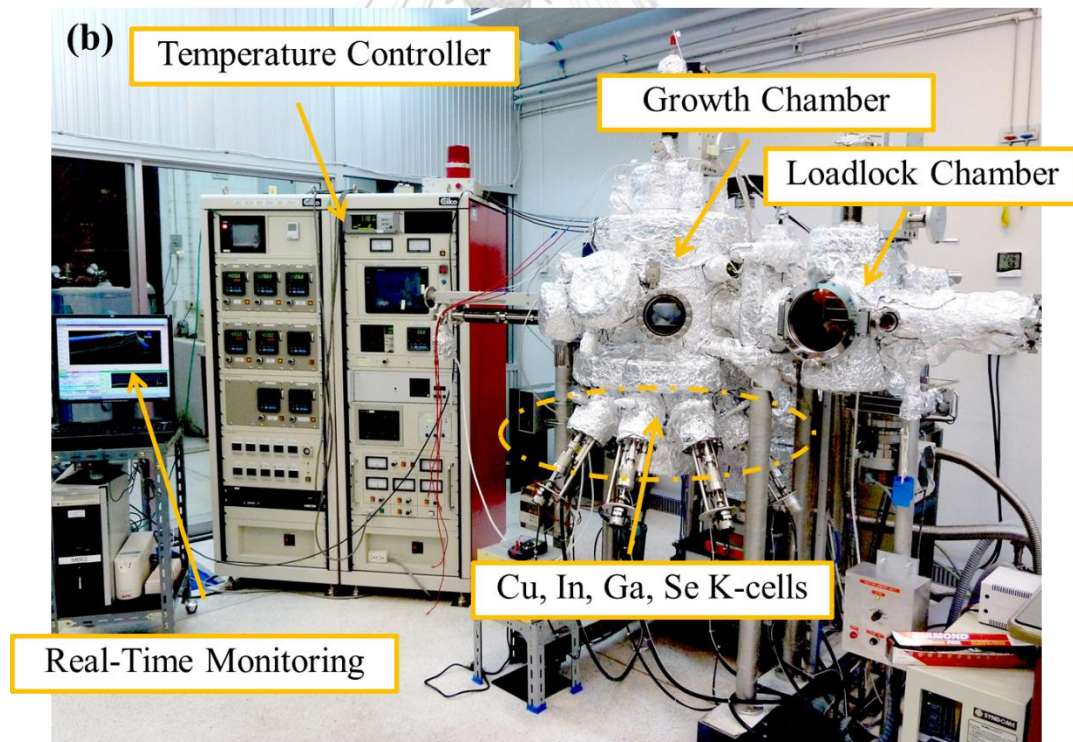
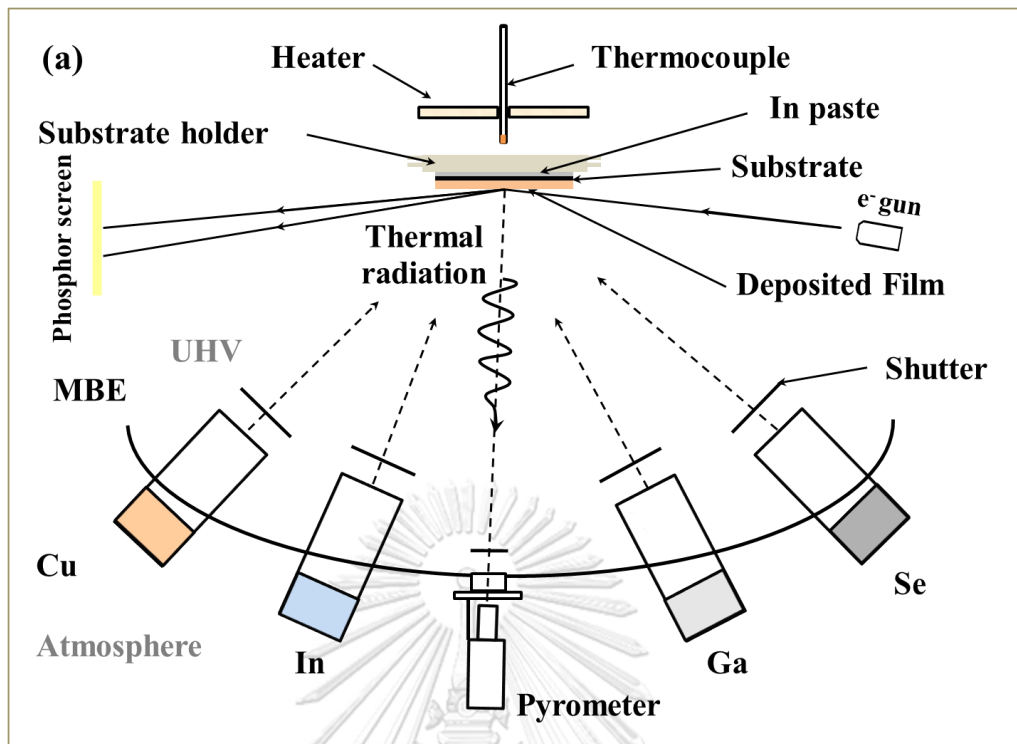


Figure 24: (a) The schematic illustration of the MBE system with RHEED and pyrometer setting. (b) The photograph of molecular beam epitaxy system contains all of the components needed for growth and in-situ analysis (SPRL, Chulalongkorn University).

which the ions formed are resolved by a mass spectrometer. For our system, the RGA has a capacity for determining the composition of gas in the range 1–100 AMU, with a resolution of 0.5 The AMU and the measurement of partial pressures about 10^{-12} Torr.

(b) Quartz Crystal Thickness Monitor (QCM)

To measure a film thickness or a deposition rate for film growth, a quartz crystal thickness monitor is generally used to measure the amount of deposition via its own surface of acoustic resonator. The quartz crystal performs based on a principle of the piezoelectric effect. At a constant temperature, the quartz vibrates at its natural frequency, and this frequency is still stable as long as it is not interrupted by the materials deposited on its surface. Depositing of the material on the crystal's surface induces the change of the mass of the crystal. Increasing mass from the deposition results in the change of the resonant frequency of the crystal that is lower and can be detected electronically and converted into the thickness or deposition rate. Due to the fact that quartz crystal is an indirect monitor and stand in the different position from the specimen, the quartz presents an accurate indication only of the film thickness on the crystal itself. Thus, it is not a true representation of the thickness of the film being deposited on actual substrate position. However, it can give a very close to real values of thickness or deposition rates with appropriate correction factor.

(c) Reflection High Energy Electron Diffraction (RHEED)

A RHEED system consists of an electron gun and a phosphor screen, the acceleration voltage for a commercially available RHEED system is typically between 5–50 keV. Electron beam is directed towards the sample at grazing incidence. Electrons scatter through small angles, only the top 1–2 atomic layers of the crystal, and a diffraction pattern appears on the phosphor screen. Thus, it can be used to monitor the growth of epitaxial films with the resolution of atomic layer that is also known as RHEED oscillation.

(d) Pyrometer

A pyrometer is normally used for monitoring the radiation from the front surface of the substrate which converts the radiation signals into the temperature obeying the Stefan-Boltzmann's radiation law. The pyrometer (IR-FA model) contains a high

resolution monochromatic (InGaAs, 1.55 μm) fiber optic type that responds to the range of infrared radiation of 250–1000°C. For CIGS thin film growth using the 2-stage or 3-stage processes, the thermal radiation signals from the pyrometer can be used to observe the conversion of the composition of CIGS thin films [67, 68]. Additionally, the signals from pyrometer also yield the thickness of the film by observing the period of oscillations due to the interference by the multiple reflections of thermal radiation at the back and the front surface of the growing films.

3.1.3.2 Calibration of Molecular Constituents

Cu(In,Ga)Se₂ thin films are grown by MBE system from solid sources of Cu (6N = 99.9999% of purity), In (6N), Ga (7N) and Se (5N) by co-evaporation of the elements in each K-cell. The elements have different vapor pressures that are related to their melting point temperature. Then, the working ranges of temperature to provide the evaporation rate of the elements are also different. Before the growth process, it is necessary to check the evaporation rate of each source at different temperatures in the range of working temperature by using the quartz thickness monitor (QCM). These data will be plotted following the relationship between the deposition rate and the effusion cell temperature given by

$$\ln(r) = a \frac{1}{T} + b, \quad (3.1)$$

where r is the deposition rate ($\text{\AA}/\text{s}$), T is the effusion cell temperature ($^{\circ}\text{C}$), a and b are parameters obtained by the least-square fit. The plot of the logarithm of deposition rate versus the inversed effusion cell temperature of Cu, In and Ga are shown in Fig. 25. It is noted here that the deposition rate of Se is not involved in this calibration because it is always oversupplied during the film deposition.

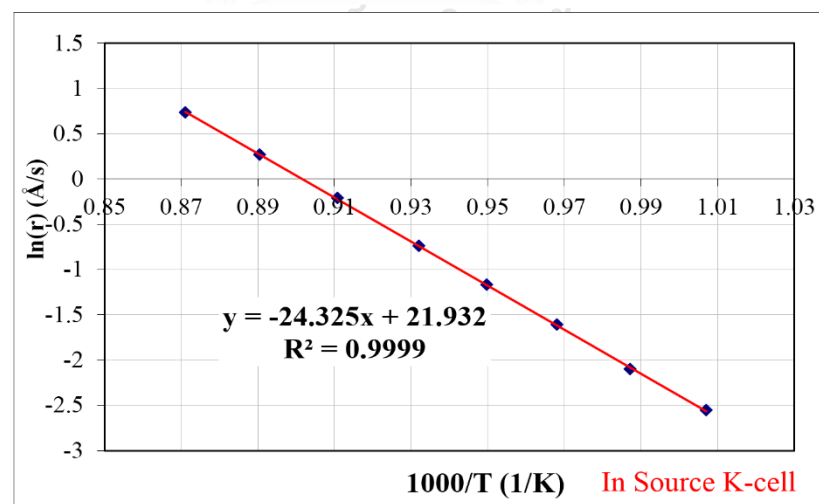
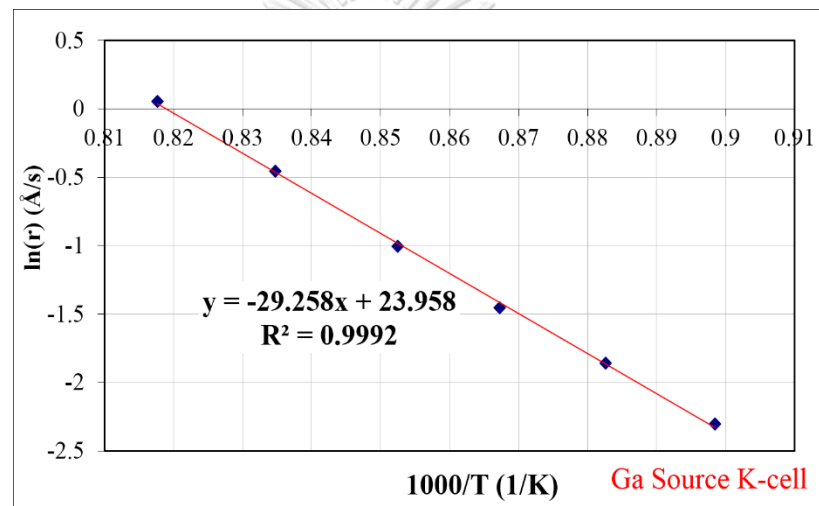
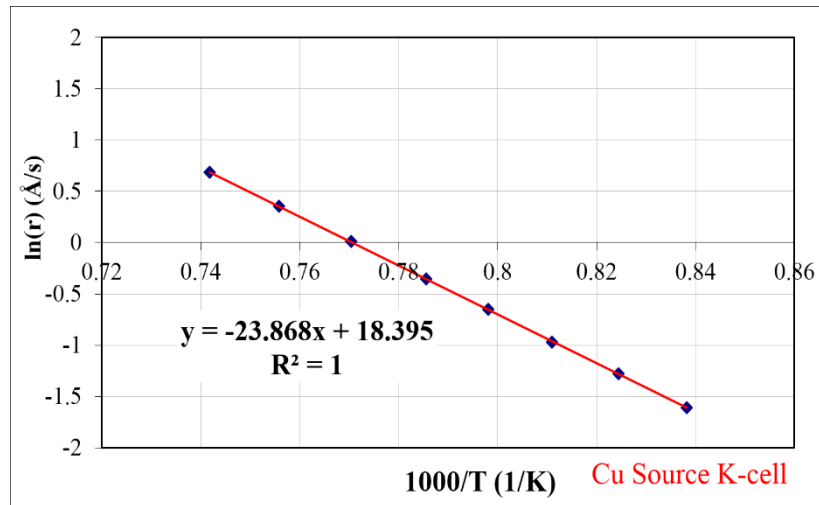


Figure 25: Plots of elemental deposition rates vs. inverse temperature.

3.1.3.3 Calculation of the CIGS Film Deposition

After obtaining the fitting parameters a and b from Eq. (3.1) for each source and suppose a certain thickness of film is required, one must know the deposition rate of the elements in order to set the deposition temperature of each K-cell. Firstly, it is necessary to determine the rate of Cu (r_{Cu}) by using the equation

$$r_{Cu} = \frac{d_{Cu}}{t_{Cu}}, \quad (3.2)$$

$$\text{and } d_{Cu} = \frac{N_{Cu} \cdot (M_{Cu}) \cdot (\rho_{CIS} \cdot (1-x) + \rho_{CGS} \cdot x)}{N_{CIGS} \cdot (M_{Cu} + M_{In} \cdot (1-x) + M_{Ga} \cdot x + 2 \cdot M_{Se}) \cdot (\rho_{Cu})} \cdot d_{CIGS}, \quad (3.3)$$

where r_{Cu} is the deposition rate of the Cu elements ($\text{\AA}/s$),

d_{Cu} is the thickness of the Cu element (\AA),

t_{Cu} is the total time for deposition of Cu element,

N_{Cu} and N_{CIGS} are the number of Cu atoms and CIGS molecules that is set N_{Cu}/N_{CIGS} equal unity,

x is the ratio of group-III elements, $[Ga]/([Ga]+[In])$, that corresponds to the alloying combination between CuInSe_2 (CIS; $x = 0$) and CuGaSe_2 (CGS; $x = 1$) of $\text{Cu}(\text{In}_{1-x}\text{Ga}_x)\text{Se}_2$ film,

i is the elemental symbol of Cu, In and Ga,

M_i is the molecular mass of each element,

and ρ_i is the density of each element.

The rate of Ga and In (r_{In} , r_{Ga}) can be derived from the Ga and In elements ratio and Cu-atomic ratio,

$$x = \frac{[Ga]}{[Ga]+[In]} = \frac{N_{Ga}}{N_{Ga} + N_{In}}, \quad (3.4)$$

$$y = \frac{[Cu]}{[Ga]+[In]} = \frac{N_{Cu}}{N_{Ga} + N_{In}}, \quad (3.5)$$

The number of atoms for each element (N_{Ga} , N_{In} and N_{Cu}) is

$$N_i = \frac{\rho_i \cdot V \cdot N_A}{M_i} = \rho_i \cdot M_i^{-1} \cdot d_i \cdot A \cdot N_A. \quad (3.6)$$

Then, the x and y ratios in a unit area of CIGS thin film are rewritten as;

and

$$x = \frac{\rho_{Ga} \cdot M_{Ga}^{-1} \cdot d_{Ga} \cdot A \cdot N_A}{(\rho_{Ga} \cdot M_{Ga}^{-1} \cdot d_{Ga} + \rho_{In} \cdot M_{In}^{-1} \cdot d_{In}) \cdot A \cdot N_A}, \quad (3.7)$$

where A is the unit area for growing film,

N_A is Avocadro's constant = 6.02×10^{23} atoms or molecules.

The parameter α_i is defined as the ratio of density to molecular mass of each element.

$$\alpha_{Cu} = \rho_{Cu} \cdot M_{Cu}^{-1}, \quad (3.8a)$$

$$\alpha_{In} = \rho_{In} \cdot M_{In}^{-1}, \quad (3.8b)$$

and

$$\alpha_{Ga} = \rho_{Ga} \cdot M_{Ga}^{-1}, \quad (3.8c)$$

where the density (ρ_i) and molecular mass values (M_i) of the materials are given in Table 5

Table 5: Density, mass per mole and α_i parameter of the materials.

Material	ρ (g/cm ³)	M (g/mole)	$\alpha = \rho/M$ (mole/cm ³)
Cu	8.96	63.55	0.1410
In	7.31	114.82	0.0637
Ga	5.91	69.72	0.0848
Se	4.79	78.96	0.0607
CIS	5.89	336.29	-
CGS	5.27	291.19	-

Substituting Eqs. (3.8a), (3.8b) and (3.8c) into Eqs. (3.6) and (3.7), then the relationship of the metal film thicknesses is obtained;

$$d_{Ga} \cdot \alpha_{In} + d_{Ga} \cdot \alpha_{Ga} = d_{Cu} \cdot \alpha_{Cu} \cdot \frac{1}{y} = d_{Ga} \cdot \alpha_{Ga} \cdot \frac{1}{x} \quad (3.9)$$

Rearranging Eq. (3.9) to obtain

$$d_{Ga} = \frac{x}{y} \cdot \frac{\alpha_{Cu}}{\alpha_{Ga}} \cdot d_{Cu}, \quad (3.10)$$

$$d_{In} = \frac{(1-x)}{y} \cdot \frac{\alpha_{Cu}}{\alpha_{In}} \cdot d_{Cu}, \quad (3.11)$$

Since, the thickness of the element is proportion to the total time of deposition of the element, $d_i = r_i \cdot t_i$. Thus, Eqs. (3.10) and (3.11) become

$$r_{Ga} = \frac{x}{y} \cdot \frac{\alpha_{Cu}}{\alpha_{Ga}} \cdot r_{Cu}, \quad (3.12)$$

$$r_{In} = \frac{(1-x)}{y} \cdot \frac{\alpha_{Cu}}{\alpha_{In}} \cdot r_{Cu}, \quad (3.13)$$

Substituting r_{Cu} , r_{Ga} and r_{In} back into Eq. (3.1), including fitting parameters, a and b , then the working temperatures of the sources for the deposition of CIGS thin films can be obtained. The details for the deposition of 3-stage CIGS (112-CIGS) and $\text{Cu}(\text{In,Ga})_3\text{Se}_5$ (135-CIGS) thin films are described in the next section.

3.1.3.4 Deposition of the CIGS Thin Films

As previously mentioned in chapter II, the 3-stage process is widely used to achieve high efficiency device. For this experiment, the deposition method of the 112-CIGS thin film is based on the 3-stage growth process. For example of the CIGS thin film of 1.8 μm thick and a thin layer capping of 135-CIGS of 10 nm thick. The deposition time (t_i) and composition x and y parameters of CIGS and 135-CIGS films are listed in Table 6. The expression (3.3) shows that the amount of Cu film depends on the total thickness of CIGS film. Thus, by substituting the number of Cu atoms and

CIGS molecules, the density of each element, group-III element ratio (x) and Cu-atomic ratio (y), the Cu thickness (d_{Cu}) is obtained, and hence the deposition rate of Cu (r_{Cu}) using Eq. (3.2). Finally, the operating temperature for Cu (T_{Cu}) is achieved from Fig. 25. In the same way, the Eq. (3.12) and (3.13), the rate of Ga and In can be attained and thus their operating temperatures.

Table 6: Parameters for the growth of CIGS.

Parameters	Required data	
	CIGS	135-CIGS
$d_{CIGS, 135-CIGS}$	1800 nm	10 nm
t_{Cu}	1800 s	90 s
x	0.37	0.37
y	1.3	0.33
Parameters	Calculated data	
	CIGS	135-CIGS
d_{Cu}	2,268.8 Å	12.6 Å
r_{Cu}	1.260 Å/s	0.140 Å/s
r_{Ga}	0.593 Å/s	0.259 Å/s
r_{In}	1.350 Å/s	0.591 Å/s
T_{Cu}	1061°C	914°C
T_{Ga}	927°C	883°C
T_{In}	861°C	814°C

The *in-situ* monitoring signals of the 3-stage 112-CIGS and 135-CIGS fabrication are shown in Fig. 26. These main signals compose of (i) emission of radiation from the front surface of the growing film detected by a pyrometer (T_{pyro}) (ii) substrate temperature (T_{sub}) and (iii) output power of substrate temperature controller (OP). During the process, T_{sub} , OP and T_{pyro} are monitored simultaneously. Nishiwaki and his group found that the existence of a $Cu_{2-x}Se$ secondary phase affects the infrared (IR) emissivity of the growing CIGS film [68, 69]. Then, the desired Cu-rich and Cu-deficient composition can be obtained. In the first stage, In Ga and Se are

deposited by setting the substrate temperature at 300°C in order to form $(\text{In,Ga})_2\text{Se}_3$ (IGS). Afterwards, only Cu and Se are deposited and the substrate temperature is ramped up to 450°C within 7 minutes. Then, the overall composition of $[\text{Cu}]/([\text{Ga}]+[\text{In}])$ is continuously increased towards $y \sim 1.0$ (stoichiometry) at the process point namely $t_{\text{stoi},1}$ where T_{pyro} suddenly decreases while OP rises up due to the surface segregation of Cu_{2-x}Se . This secondary phase has a higher emissivity in the IR range than Cu-poor CIGS materials and the increased emission of heat radiation results in a lowering substrate temperature, and then the heating OP of substrate increases in order to keep the heating power at the setting point. After $t_{\text{stoi},1}$, the time for the 2nd stage by Eq. (2.26) is terminated at a typically $y \sim 1.3$ (Cu-rich). Cu-rich film is a beneficial impact on film morphology and electronic properties [68]. Again, In Ga and Se are co-evaporated in the 3rd stage until $t_{\text{stoi},2}$ to convert from Cu-rich to Cu-poor. The heating OP decreases because Cu_{2-x}Se segregation disappears. The OP signal is descending and reaching stable value until its composition becomes to Cu-poor at $y \sim 0.9$. Next, the thin layer of 135-CIGS is thereupon deposited after the completion of the 3-stage CIGS layer with the deposition time of 90 seconds. Finally, the as-grown film is over supplied with Se during the decreasing of the substrate temperature until room temperature.

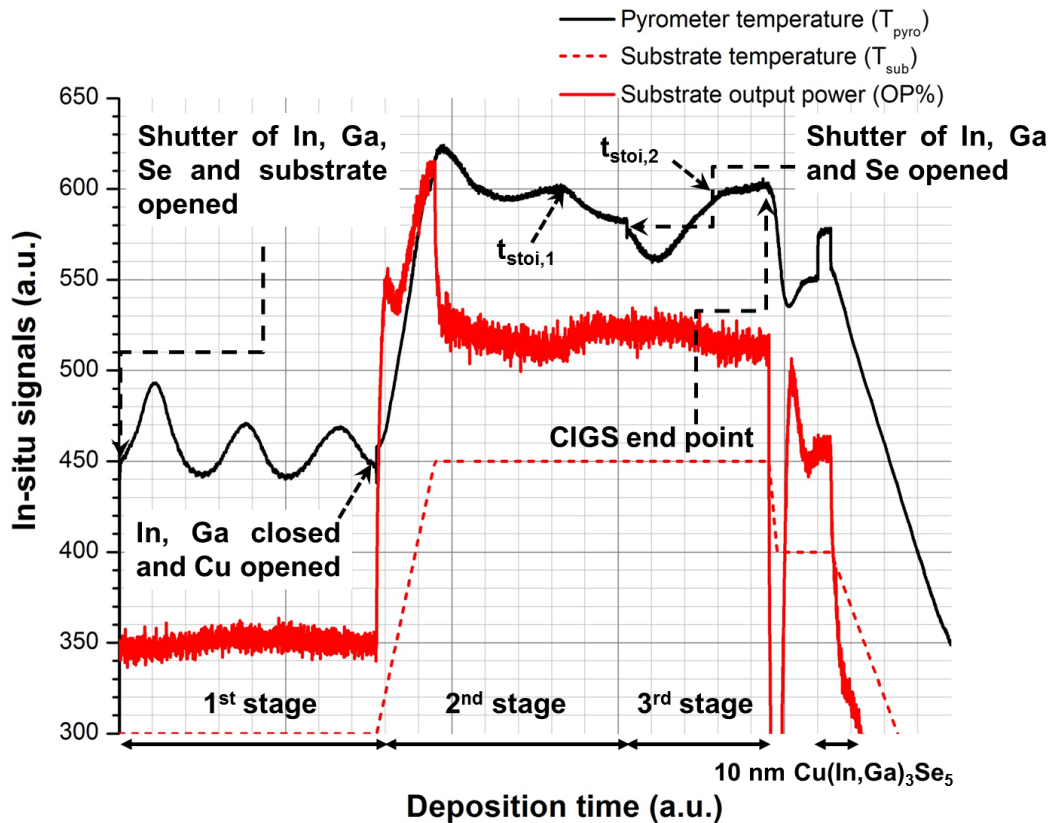


Figure 26: In situ monitoring signals during the 3-stage CIGS growth and capping layer.

3.1.4 CdS Buffer Layer

Chemical bath deposited (CBD) is employed for the deposition of CdS layer. CdS is formed by aqueous solutions using thiourea as the sulfur sources and cadmium-ammonia complex ions as cadmium precursor. DI water is used to dissolve the solids Cd salt and thiourea. The CdS liquid solution is prepared by using Cd salt (CdSO_4), thiourea ($\text{CS}(\text{NH}_2)_2$) and ammonia (NH_4OH). The amount of each solution is summarized in Table 7. Finally, the as-grown CIGS film is immersed into a beaker containing the prepared CdS prepared chemical solution with the bath temperature of 65°C and 150 rpm stirring using a magnetic stirrer. After 15 minutes, a CdS film of 50 nm thick is obtained.

The general chemical reaction of the CdS process [70] is given by

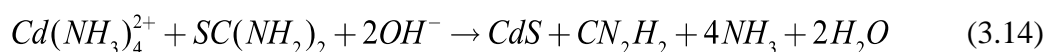


Table 7: Parameters for the CdS chemical bath process.

Chemicals	Quantity
CdSO ₄	0.3546g + 50ml DI water
SC(NH ₂) ₂	2.85g + 100ml DI water
NH ₄ OH	80ml
DI Water	270ml

Ammonia supplies the ligand for the metal ions and controls the hydrolysis of thiourea. At the end of the process, the saturation phase is reached where the solution has been depleted from non-reacted Cd atoms. In order to minimize Cd particle on the surface and reduce film roughness, the deposition must be terminated before the saturation phase. The films are then rinsed with DI water and dried with compressed nitrogen gas.

3.1.5 Window Layers of CIGS

The window layers of the CIGS thin film solar cells consist of two layers; (i) the high resistance (HR) window layer which is deposited onto the CdS buffer layer (ii) the low resistance (LR) window layer. The high resistance intrinsic ZnO (i-ZnO) and the low resistance n-type of ZnO(Al) semiconductor are a typical combination for the CIGS thin film solar cells. The role of i-ZnO is to permit the junction of CIGS and CdS to be more stable during the deposition of ZnO(Al). Moreover, it would be favorable for the band alignment. Intrinsic ZnO and ZnO(Al) have band gaps of 3.2 eV and 3.6–3.8 eV, respectively. The role of ZnO(Al) is to provide maximum electrical conductivity with its minimum optical absorption to collect and move electrons to the front contact (Al grid).

In the deposition process of i-ZnO, the RF (13.6 MHz) magnetron sputtering is used from a ceramic i-ZnO target (2-inch diameter) in Ar atmosphere of 6×10^{-3} mbar with the sputtering power of 40 Watt for 20 minutes. The thickness of i-ZnO layer is about 50 nm. Then, the ZnO(Al) is subsequently deposited by the RF magnetron sputtering using the ZnO target with 2wt.% doped of Al₂O₃ (4-inch diameter) in Ar

atmosphere of 3×10^{-3} mbar with the sputtering power of 220 Watt for 17 minutes. The samples are rotated at 3 rpm in order to allow the relaxation of the film. The distance between a substrate holder and a target is about 6 cm. The desired thickness for ZnO(Al) is approximately 200 nm.

3.1.6 Al Metal Grid

Al grid is used as the front contact in order to collect and move current to an external circuit. This Al grid is an advantage for a reduction of ZnO(Al) thickness which minimizes optical losses. The metal Al grid is evaporated through a shadow mask by the thermal evaporation system at vacuum pressure in the order of 10^{-6} mbar. Al grid thickness is approximately 1.5–2.0 μm .

3.2 Sample Characterizations

3.2.1 Scanning Electron Microscopy (SEM)

SEM is an important apparatus used for the measurements of microscopic features. For imaging, a beam of electrons in a pinpointed spot impinges on the surface or cross-section of a specimen. Then, the image collections and displays are produced by scanning the sample with a focused electron beam and detecting the secondary and/or backscattered electrons from the target materials. The electron energy is typically 10–30 keV for most samples, but for insulating samples the energy can be as low as several hundred eV. The use of electrons has two main advantages over optical microscopes; (i) much larger magnifications are possible since electron wavelengths are much smaller than photon wavelengths and (ii) the depth of field is much higher.

The JEOL JSM-7001F SEM equipment is used to apply in this work. Its resolution is about 1.2 nm at 30 kV with a wide range of magnification about $25\times$ to $1,000,000\times$. The SEM is used to investigate the surface texture in comparing CIGS and 135-CIGS films. The samples to be analyzed using SEM are often bound with a thin conductive layer such as silver paint to achieve better resolution and signal quality.

3.2.2 Energy Dispersive X-Ray Spectroscopy (EDS)

EDS analysis system is generally attached to the SEM, where the electron beam serves to excite characteristic X-rays from the area of the specimen being probed. EDS is used for inspection of the elemental composition or chemical characterization of thin films. Ordinarily, EDS has an effective probe depth of $\sim 1 \mu\text{m}$ and is restricted to detect elements with $Z > 5$ (Boron, B). The detection limits for the EDS are ranging from ~ 0.1 to 1 at.% when a Beryllium (Be) window is used. In this work, the samples are analyzed with an acceleration voltage of 15 kV.

3.2.3 X-Ray Diffraction (XRD)

The crystalline structures of 112-CIGS, 135-CIGS and bilayer systems of 112-CIGS and 135-CIGS are investigated by XRD technique to identify and compare their crystallographic phases.

X-rays used for diffraction are electromagnetic waves with wavelengths ~ 0.5 – 2.5 \AA . In this work, the Bruker D8 Advance X-ray powder diffractometer emitted the wavelengths of $\text{Cu}_{K\alpha 1}$ ($\lambda = 1.5406 \text{ \AA}$) and $\text{Cu}_{K\alpha 2}$ ($\lambda = 1.54439 \text{ \AA}$) radiations at 40 kV was used. When an incident beam of X-rays strikes the crystal planes that act as mirrors in reflecting the incident X-ray beams, at an angle such that the wave patterns of the beam leaving the various planes are in phase, then the constructive interference of waves occurs as shown in Fig. 27. These constructive waves satisfy Bragg's condition,

$$2d_{hkl} \sin \theta = n\lambda, \quad (3.15)$$

where d_{hkl} is the interplanar spacings. In most cases, the first order of diffraction ($n = 1$) is used.

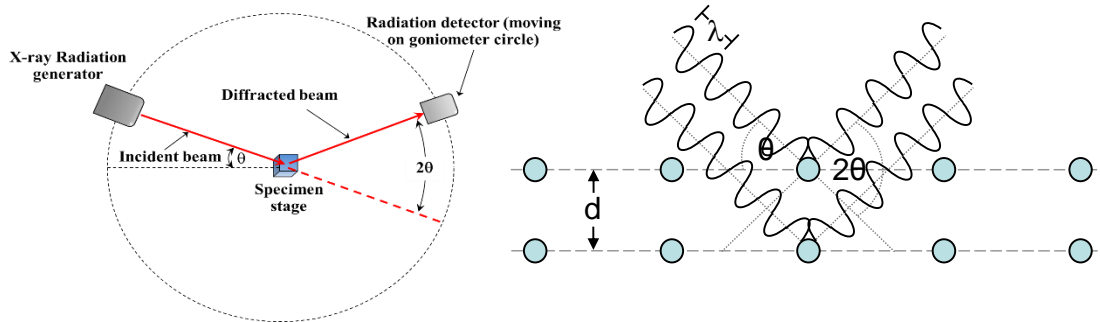


Figure 27: Schematic illustration of the diffractometer of crystal analysis and of the conditions necessary for diffraction.

For the tetragonal unit cell with lattice parameters a and c of chalcopyrite structure, d_{hkl} can be determined from

$$\frac{1}{d_{hkl}^2} = \frac{h^2 + k^2}{a^2} + \frac{l^2}{c^2}, \quad (3.16)$$

where h , k and l are the Miller indices of the diffraction planes.

3.2.4 Optical Transmittance and reflectance Spectroscopy

As previously mentioned on the optical absorption in chapter II, the band gap energy can be determined through the transmission measurements. Perkin-Elmer model Lambda 900 UV-VIS-NIR spectrophotometer is used to measure optical transmission and reflection for this study. From Eq. (2.6), the film thickness must be known before calculating absorption coefficient (α). The thickness of the film on the SLG substrate can be determined from the interference fringes of transmission or reflection spectra as shown for example in Fig. 28 and corresponded to Eq. (3.17)

$$d = \frac{M\lambda_1\lambda_2}{2n|\lambda_1 - \lambda_2|}, \quad (3.17)$$

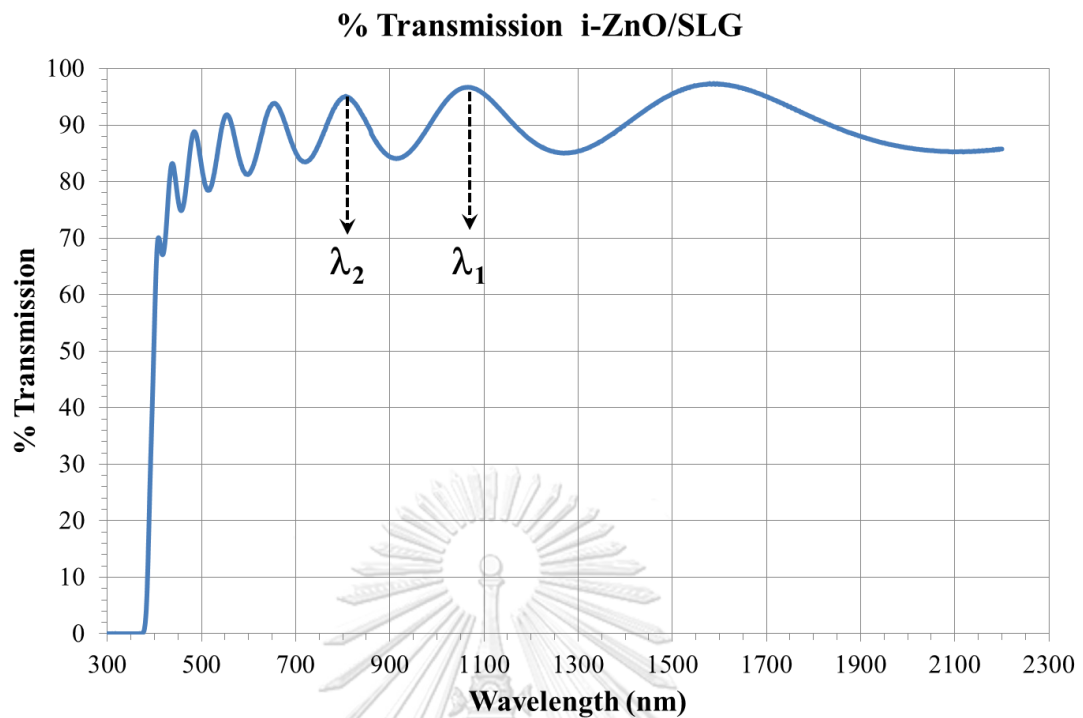


Figure 28: Example of optical transmittance spectrum of i-ZnO.

where M is the number of cycles observed from wavelength λ_1 to λ_2 and n is the refraction index of measured film. The number of interference fringes increases with increasing of film thickness. The cut-off wavelength shows no interference because of the complete light absorption near the band edge.

3.2.5 Photoluminescence (PL) มหาวิทยาลัย

The photoluminescence setup is illustrated in Fig. 29. The sample is excited by He-Ne laser (632 nm) with 35 mW. A closed-circuit helium cryostat (Leybold: Model RDK 10-320) is used to cool down the sample from room temperature 300 K to 10 K. The PL system consists of two lenses that are used to collect photoluminescence signals into the adjustable entrance slit of a doubled grating monochromator (Jobin Yvon SPEX 750M). The signal in the IR range is detected by a liquid-nitrogen cooled Ge (Edinburgh Instrument model EI-L). The detected signal is then filtered and amplified by a lock-in amplifier. The spectrometer is controlled through Syner jyTM Jobin Yvon Horiba program and the collected signal is recorded in a computer. The measurements are performed both temperature-dependent from 10 K to 300 K and excitation power-dependent from 0.1 to 35 mw.

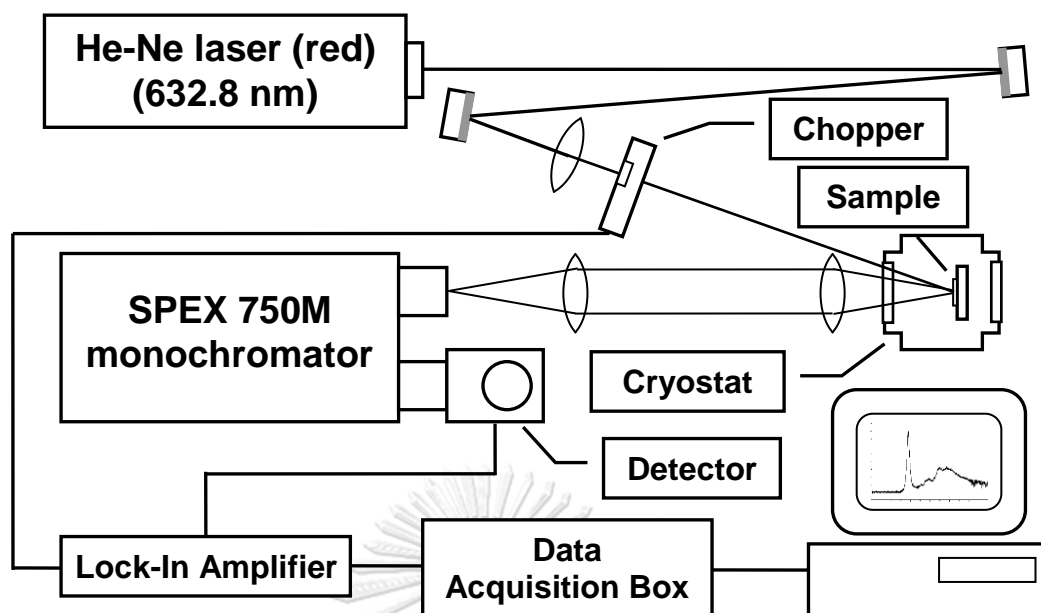


Figure 29: Schematic diagram of photoluminescence spectroscopy setup.

3.2.6 Atomic Force Microscopy (AFM)

The atomic force microscope is generally used in the fields of surface science, electrochemistry biology and technology. AFM is used to measure the surface morphology, grain size evaluation, the roughness of the film, i.e., peak-to-valley roughness, average rough and root mean squared (RMS) roughness. AFM operates by the measuring force between a probe and sample. This force depends on the nature of the sample, the distance between the probe and the sample, the probe geometry, and sample surface contamination. AFM is suitable for conducting as well as insulating samples. The AFM principle is illustrated in Fig. 30. The instrument consists of a PZT tube scanner, a laser with position-sensitive photo detector and a cantilever with a sharp tip mounted on its end. The vertical sensitivity depends on the cantilever length. For topographic imaging, the tip is brought into continuous or intermittent contact with the sample and scanned across the sample surface. The changes in surface topography results in a deflection of the cantilever. The deflection of the cantilever is measured using a laser spot reflected from the top surface of the cantilever into an array of photodiodes and generates a surface topography. In this study, the surface texture of samples is investigated by AFM (Veeco model Dimension 3100) counterpart with SEM surface. The operation mode of this

measurement is the tapping mode which maps topography by lightly tapping the surface with an oscillating probe tip.

3.2.7 Current-Voltage Characteristics

The solar cell parameters, e.g., open-circuit voltage (V_{oc}), short-circuit current density (J_{sc}), fill factor (FF), series resistance (R_s), shunt resistance (R_{sh}) and solar cell efficiency (η) are obtained under the light irradiation of AM 1.5 at 25°C. Xenon arc lamp is served as a light source with the power density about 100 mW/cm². Keithley model 238 is a bias voltage source and a current measurement unit. The solar cell is contacted using a four-probe configuration. The solar cell area is approximately 0.5 cm².

3.2.8 External Quantum Efficiency (EQE) Measurement

The quantum efficiency is used to determine the capability to generate photocurrent when a solar cell is illuminated by photons at particular wavelength. The EQE can be defined as

$$EQE(\lambda) = \frac{\text{number of collected electrons}}{\text{number of incident photons}}. \quad (3.18)$$

In other words, the EQE is the probability that the number of charge carriers produced by the solar cell when irradiated by photon of a particular wavelength. The EQE also shows the carrier collection and defects that possibly agree to the leak path of poor solar cell. In fact, the ideal EQE is equal to one. However, the actual EQE can be reduced from unity due to the capable a layer film to generate its photocurrent as shown in Fig. 31. The EQE system is composed of a KEITHLEY 238 High Current SMU (Source-measure unit) with a four-probe configuration. A monochromator is used to apply monochromatic light in the range of 300–1300 nm. The J_{sc} at zero voltage bias is measured and collected by a computer with a reference cell.

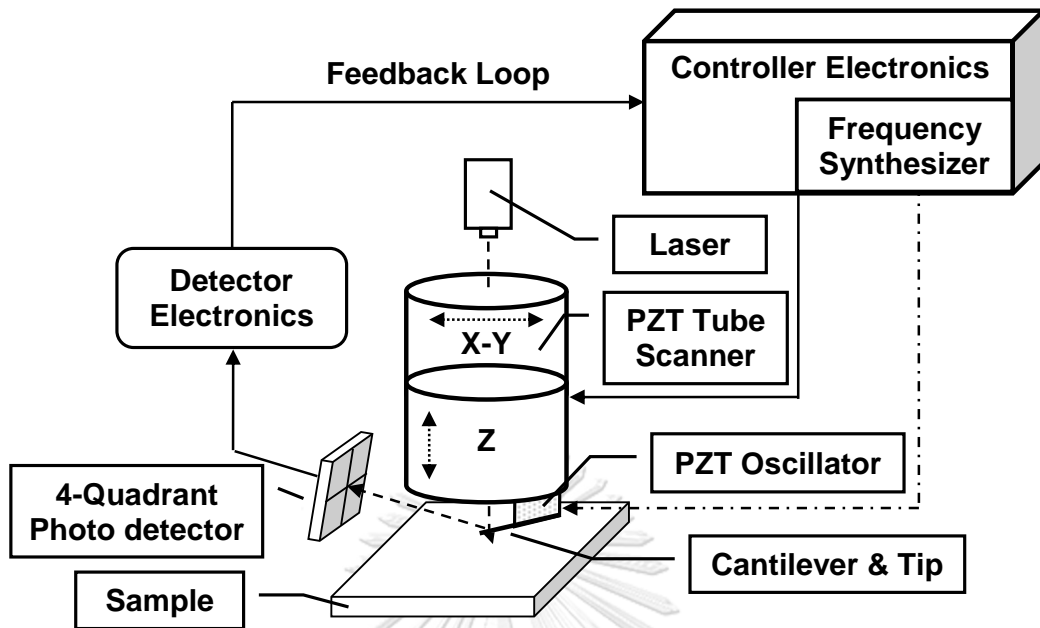


Figure 30: Schematic illustration of an atomic force microscope.

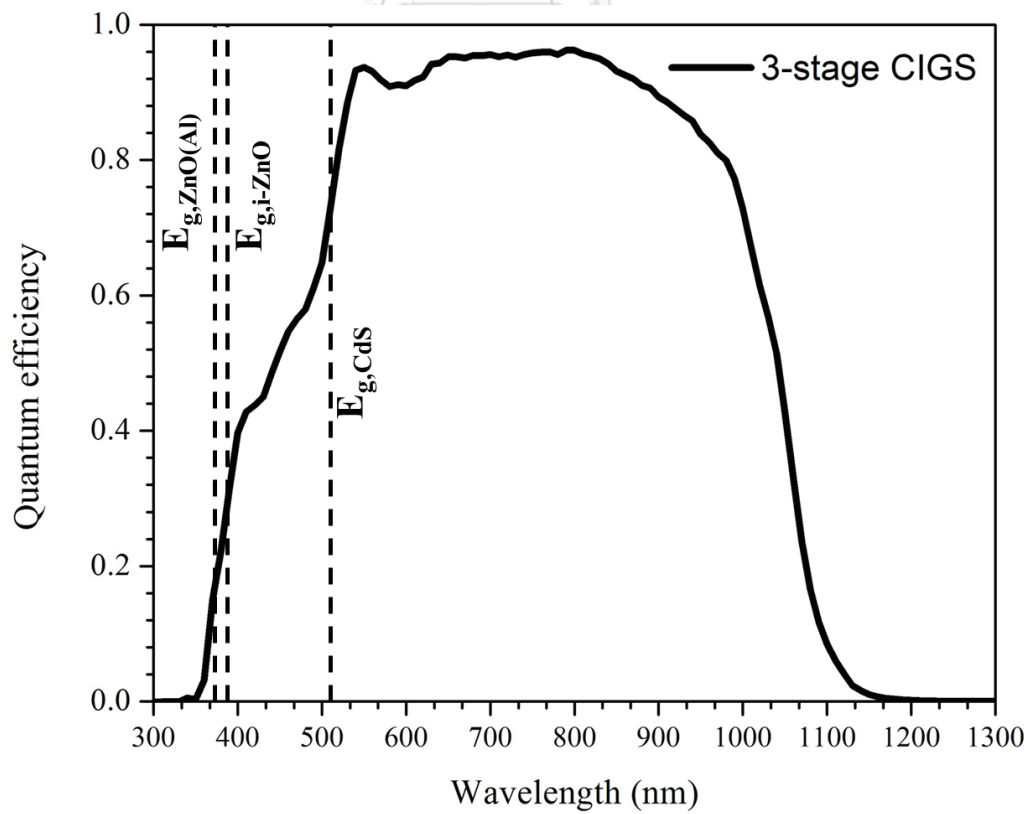


Figure 31: Example external quantum efficiency of a 3-stage CIGS solar cell.

CHAPTER IV

EFFECTS OF Cu(In,Ga)₃Se₅ THIN LAYER ON Cu(In,Ga)Se₂ ABSORBER THIN FILMS

Cu(In,Ga)Se₂ (112-CIGS) and Cu(In,Ga)₃Se₅ (135-CIGS) semiconductor thin films have in common a direct band gap energy, chalcopyrite crystalline structure or even higher absorption coefficient. However, there are a few differences between them in their values of energy gap, lattice parameters and carrier types. In order to understand effects of 135-CIGS on 112-CIGS thin films (135-CIGS/112-CIGS), this chapter describes in details about the influences of 135-CIGS capping layer on the properties such as morphologies, XRD patterns and optical band gap energy. Moreover, the solar cell parameters and external quantum efficiency (EQE) by the effects of 135-CIGS capping layer on the devices are investigated.

4.1 Motivation

CuInGaSe₂ (112-CIGS) is a chalcopyrite semiconductor that was introduced as a photon absorber material for high efficiency thin film solar cells, whose world-record efficiency of 22.9% was reported by Solar Frontier [2]. The world-record cells were achieved with the Ga composition ratio $x \equiv [\text{Ga}]/([\text{In}]+[\text{Ga}])$ in the ranges of 0.30-0.33 that corresponds to a band gap energy (E_g) of less than 1.4 eV. It has also been shown that the E_g of CIGS varies with Ga content [10, 71]. The highest efficiency is relatively lower than the optimum value given by the theoretical calculation [72, 73]. The wider E_g has an effect on the increase in open-circuit voltage (V_{oc}) of the photovoltaic devices. However, excessive E_g or V_{oc} leads to a negative impact on the device performance due to the decrease in generated current in the long wavelength region [74]. Grading of the conduction band (ΔE_c), e.g., normal grading or double grading, has been adopted in order to improve the carrier collection and also to improve V_{oc} with an additional electric field due to the variation of conduction band of the absorber. The normal grading is achieved from the increase in the band gap towards the back contact leading to additional electric field which enhances the diffusion length of the electrons due to a lower recombination at the back contact. This results in the increase in short-circuit current density (J_{sc}) of the devices.

However, the normal grading may lead to lower V_{oc} because of narrower E_g at the front region near the junction. An alternative choice is a double grading of conduction band at the front and back regions of the CIGS film that can enhance V_{oc} due to the increase in the E_g of the space charge region (SCR) as well as the improvement of J_{sc} due to the additional electric fields and the absorption in the long wavelength region [59, 60]. However, the design of graded band gap is rather limited by the difficulty in controlling elemental diffusion in the depth profile. The minimum front band gap grading should be contained within the SCR without losing fill factor (FF) and J_{sc} [6]. By increasing Ga concentration for grading band gap configuration, the increase in charge recombination at CdS/CIGS interface owing to higher deep defect concentrations of Ga contents can also cause V_{oc} of CIGS devices to decrease [75-77]. Furthermore, the increase in V_{oc} without losing J_{sc} was also achieved by the modification of CIGS surface, e.g., through sulfurization to form a $Cu(In,Ga)(Se,S)_2$ [14, 78] or post-deposition treatment (PDT) with alkali metal compounds such as KF, RbF and CsF to form a Cu-depleted layer in the near-surface region [4, 79-83]. It has been shown that the incorporation of S can cause the diffusion of Ga toward the surface of the CIGS absorber [78]. This results in the Ga gradient near the SCR and leads to the increase in E_g and V_{oc} of the CIGS devices. However, the sulfurization requires the use of toxic H_2S gas to supply sulfur to the $Cu(In,Ga)(Se,S)_2$ films. For the PDT with heavy alkali metal compounds, such as RbF and CsF, they were found to significantly affect the increase in E_g or V_{oc} of high Ga CIGS devices. The use of RbF was shown to be the most effective PDT for reducing the loss of V_{oc} as indicated by the lowest slope of $V_{oc}(t) - \text{transient}$ [81]. For the narrow- E_g CIGS absorbers, RbF-PDT has also been employed to increase the performance of the CIGS bottom sub-cell used in the perovskite/CIGS tandem devices [82]. The devices with RbF treatment yield more than 4 times longer carrier lifetime than those without the treatment [82]. The alkali-PDT, especially RbF, also leads to a noticeable Cu depletion at the grain boundaries which is an advantage for hole-barriers and thus increases the efficiency of the CIGS solar cells [83]. Similar effect has also been observed in the PDT using CaF_2 [84]. However, the alkali metal treatment requires an extra source, in addition to Cu, In, Ga and Se, in the deposition system. The alkali-PDT is also in the form of harmful fluoride compound in the growth process. In addition to the recent

development in the fabrication of CIGS thin films using the sulfurization and alkali PDT techniques, the insertion of a wide band gap layer, e.g., $\text{Cu}(\text{In,Ga})_3\text{Se}_5$ (135-CIGS) with $E_g \sim 1.4$ eV, that causes a valence band offset (ΔE_v) at CIGS surface provides yet another method for pseudo-homojunction without extra deposition sources. The valence band offset at CdS/CIS interface was observed using x-ray photoelectron spectroscopy (XPS). Schmid *et al.* found that the larger E_g of 135-CIS layer at the surface can induce a valence band offset between the 135-CIS and 112-CIS films [85]. Theoretically, the valence band offset between n-type CdS and p-type 112-CIGS can repel holes and eliminate the recombination at the interface. Nishimura *et al.* showed that V_{oc} and conversion efficiency of single graded CIGS devices could be achieved with higher values than those of the devices with double graded band gap profile due to the formation of ordered defect chalcopyrite compound such as 135-CIGS, 158-CIGS or 247-CIGS on the surface of 112-CIGS [86]. Their findings also suggested that the V_{oc} improvement without affecting J_{sc} was due to ΔE_v . It has also been reported that 135-CIGS accidentally exists on Cu-poor CIGS surface [27, 28, 30, 31]. In principle, as shown in Fig. 22(d), 135-CIGS layer creates a barrier (ΔE_v) for blocking holes from reaching the interface and shifts the defect zone at p-n junction into the CIGS absorber. As a result, this defect layer should help reduce the recombination rate near the junction [7, 20, 21] despite the fact that it is very challenging to verify the existence of this defect layer directly. However, excessive thickness of this barrier could also deteriorate the performance of the CIGS solar cells [32]. Nevertheless, very few reports exist on the effects of this defect layer on the optical absorption and the solar cell properties [32, 35, 87-89].

In this dissertation, the experiment on the influence of very thin layers of 135-CIGS intentionally deposited on the surface of 112-CIGS thin films is carried out. The correlation between the optical E_g through the optical transmission and reflection measurements, the lattice parameters by the x-ray diffraction (XRD) and the photovoltaic parameters via current-density – voltage (J–V) measurements are investigated among various thicknesses of 135-CIGS layer on top of 112-CIGS films. We observe indirect evidence of the existence of these very thin 135-CIGS layers on the 112-CIGS films and devices shall be observed.

4.2 Experimental Details

A typical structure of standard 112-CIGS thin film solar cell is Al-grid/ZnO(Al)/i-ZnO/CdS/CIGS/Mo/SLG. First, 600 nm thick Mo layer was deposited on clean 3 cm × 3 cm SLG substrates by DC magnetron sputtering from a 4-inch diameter Mo metallic target using Ar gas and DC power of 6.0×10^{-3} mbar and 575 W, respectively. Then, 112-CIGS absorber was deposited by molecular beam deposition method under ultra-high vacuum environment using EIKO model EW-100 MBE system. 112-CIGS thin films were deposited by the 3-stage deposition process whose details are described in Chapter II and III. Briefly, In, Ga and Se were first deposited onto Mo-coated SLG substrate at 300°C (as measured by a thermocouple behind the substrate) to form $(\text{In,Ga})_2\text{Se}_3$ precursor, followed by evaporation of Cu and Se at higher substrate temperature of 450°C in the second stage until the overall composition was Cu-rich, e.g., $y \equiv [\text{Cu}]/([\text{Ga}]+[\text{In}]) \sim 1.3$ in this work. Again, In, Ga and Se were co-evaporated in the third stage at the same substrate temperature as performed in the second stage until the required composition was Cu deficient with $y \sim 0.9$. Ga composition ratio, i.e., $x \equiv [\text{Ga}]/([\text{Ga}]+[\text{In}])$ was set at ~ 0.37 . The Cu, In and Ga fluxes were calibrated prior to the deposition. We note that Se flux was always over supplied throughout the growth process. The thickness of 112-CIGS films was set at 1.8 μm . Next, n-type CdS buffer layer with a thickness of 50 nm was deposited by a chemical bath deposition (CBD) process. Then, the 50 and 200 nm thick i-ZnO and ZnO(Al) were respectively sputtered by RF magnetron sputtering using RF power of 40 W for i-ZnO and 220 W for ZnO(Al). Lastly, 2 μm thick Al front contact was deposited by thermal evaporation through a shadow mask.

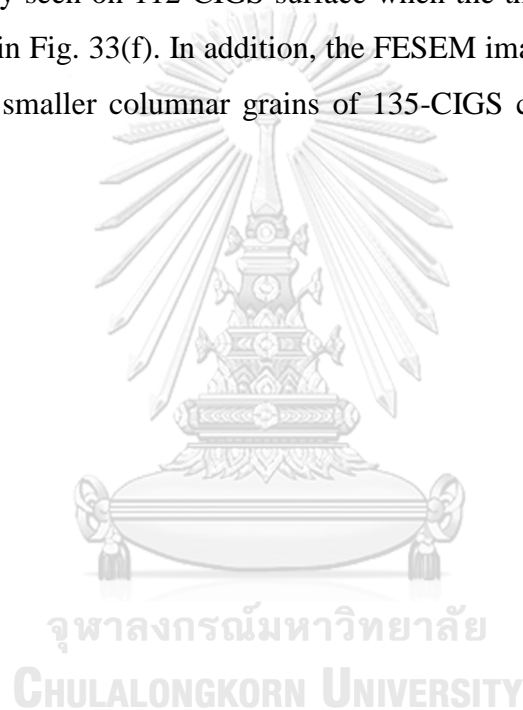
For the samples with Cu-depleted layer, the 135-CIGS thin films with the thickness of 5, 10, 20, 40, 80, 200 and 300 nm were deposited onto the 112-CIGS surfaces. In order to limit the diffusion of the constituent elements, the 135-CIGS layers were grown at 400°C within 90–180 seconds after the completion of 112-CIGS thin films. The y and x composition ratios of 135-CIGS capping layers were aimed to be 0.33 and 0.37, respectively.

Surface morphology and cross-section images of the films were investigated by atomic force microscope (AFM, Veeco model Dimension 3100) and field emission scanning electron microscope (FESEM, JEOL model 7001F). The deposition fluxes of 112-CIGS and 135-CIGS thin film were verified by the energy dispersive x-ray spectroscopy (EDS, Oxford model PentaFET X3). The accelerating voltage used for the EDS measurements of all samples was 15 kV which was sufficient for all constituent elements of the samples. UV-VIS-NIR spectrophotometer (Perkin-Elmer model Lambda 900) was used to measure the optical transmittance and reflectance of 112-CIGS, 135-CIGS and 135-CIGS/112-CIGS films in the range of 700–1400 nm. The x-ray diffractometer (PANalytical model Empyrean) was used to investigate the lattice parameter alteration of the diffraction peak of (112) and (220)(204) phases due to the 135-CIGS capping layer from the stand alone 112-CIGS thin film. The J-V characteristics of the devices were determined under AM 1.5 and 100 mW/cm² irradiance at 25°C. The external quantum efficiency (EQE) of the devices was also investigated in the range of 300–1300 nm.

4.3 Surface morphology and cross-section

The evolution of surface morphology of 112-CIGS with 135-CIGS capping layer is shown by AFM images in Fig. 32. Surface morphologies of 112-CIGS with less than 40 nm thick of 135-CIGS capping layer are indistinguishable from that of 112-CIGS with large grain size in the order of a few microns. Tiny islands start to appear on 112-CIGS surface when 135-CIGS capping layer is about 40 nm thick as shown in Fig. 32(e). When 135-CIGS capping layer becomes thicker, 112-CIGS surface is covered with small grains of 135-CIGS as shown in Fig. 32(d). We note here that the grains of 135-CIGS, Fig. 32(b), are relatively smaller than that of 112-CIGS, Fig 32(a). The surface height (z) of 112-CIGS in Fig. 32(a), Fig. 32(c), Fig. 32(d), Fig.32(e) is in the range of approximately 650–800 nm with the rms roughness (S_q) of 80–90 nm while the surface height covered with 200 nm 135-CIGS shown in Fig. 32(f) decreases to approximately 580 nm with the roughness (S_q) of 58 nm. The variation of the surface height in Fig. 32(a), Fig. 32(c), Fig. 32(d), Fig.32(e) is due to the crevices that naturally occur in 112-CIGS grown by the 3-stage deposition

process. In contrast, for the 2 μm thick 135-CIGS layer in Fig. 3(b), the surface height (z) and the rms roughness (S_q) is approximately 360 nm and 50 nm, respectively. The cross-section images from FESEM in Fig. 33 also agree with the AFM morphology images that the thin 135-CIGS capping layer residing on 112-CIGS surface is difficult to observe by physical methods for surface imaging when 135-CIGS capping thickness is less than 40 nm. The cross-section image of 40 nm thick 135-CIGS on 112-CIGS shown in Fig. 33(e) does not clearly show the capping layer contrary to the observation of tiny islands in the AFM image in Fig. 32(e). The 135-CIGS capping layer can be clearly seen on 112-CIGS surface when the thickness is more than 100–200 nm as shown in Fig. 33(f). In addition, the FESEM image in Fig. 33(b), Fig.33(d) also shows much smaller columnar grains of 135-CIGS compared to those of 112-CIGS.



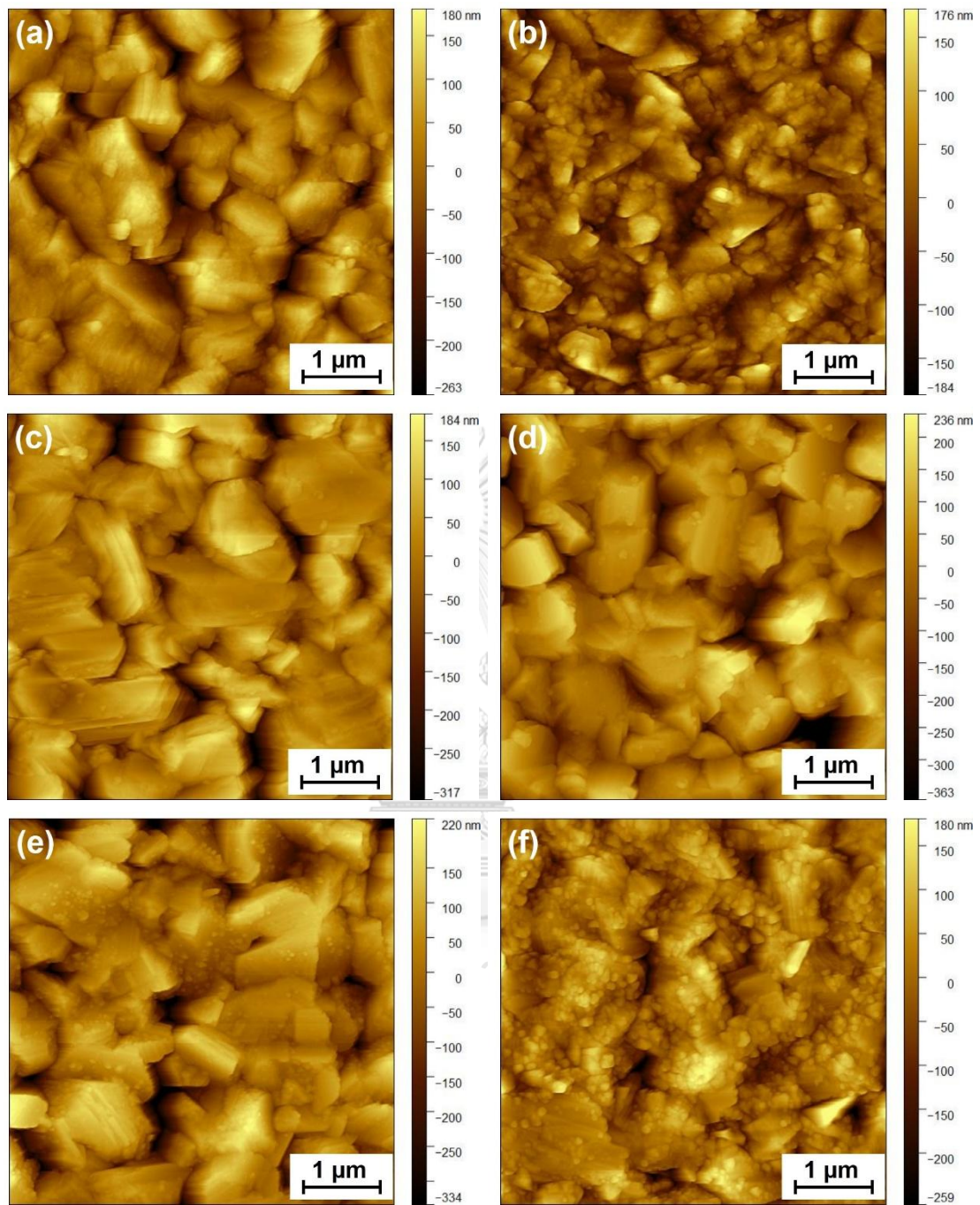


Figure 32: Surface morphologies of (a) 2 μm thick 112-CIGS (b) 2 μm thick 135-CIGS, 135-CIGS/112-CIGS with 135-CIGS capping layer (c) 10 nm, (d) 20 nm, (e) 40 nm and (f) 200 nm.

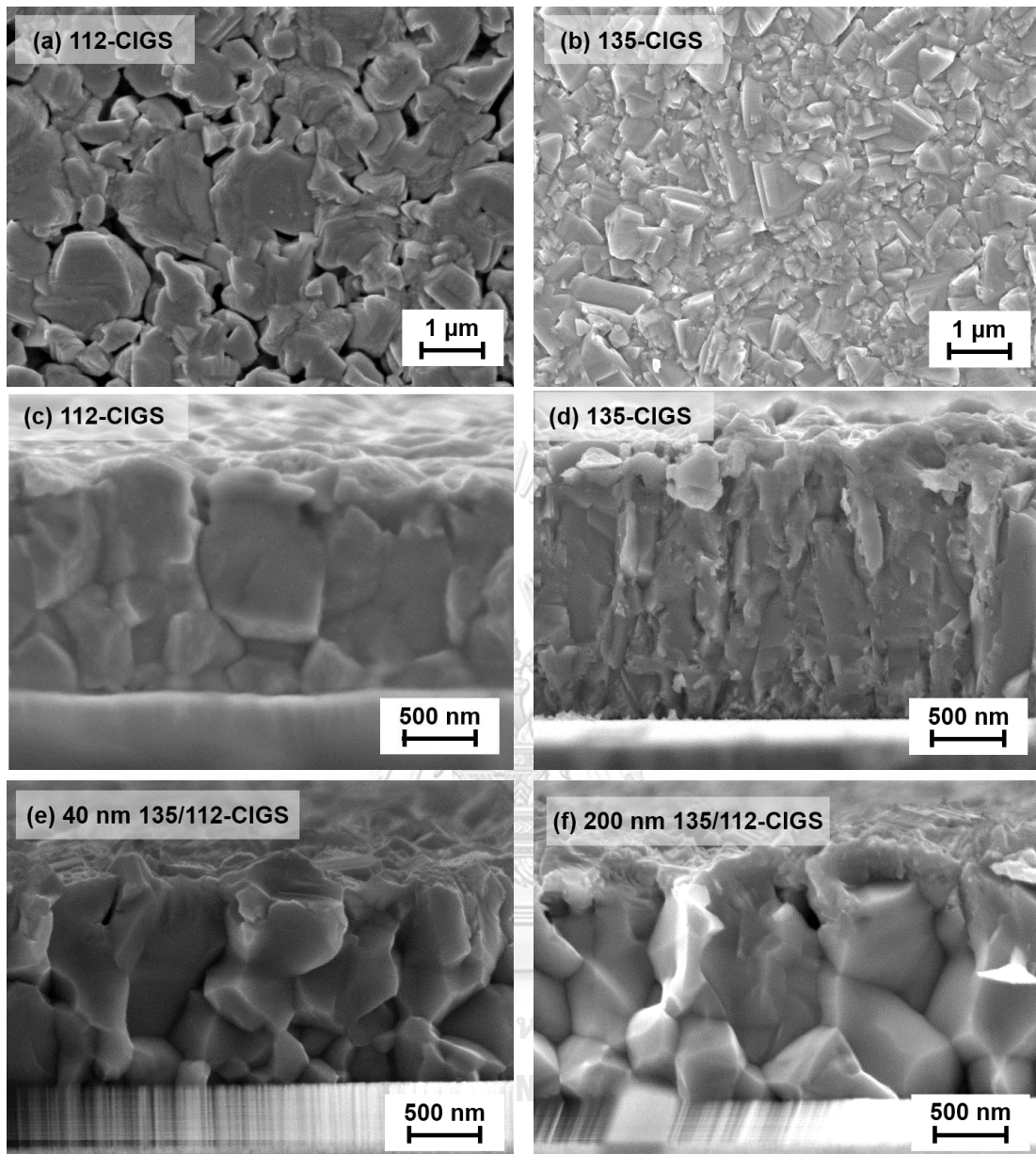


Figure 33: FESEM surface and cross-section images of (a), (c) 1.8 μm thick 112-CIGS, (b), (d) 2 μm thick 135-CIGS and 135-CIGS/112-CIGS with 135-CIGS capping layer of thickness (e) 40 nm and (f) 200 nm.

4.4 Optical band gap energy

The optical transmittance of the as-grown 112-CIGS, 135-CIGS and 135-CIGS/112-CIGS with various thicknesses of 135-CIGS was measured through an intentionally unfilled region of Mo layer on the SLG substrate. The reflectance spectra over the same area of the transmittance measurements were obtained using the reflection measurement assembly of the spectrophotometer with the beam set 6° off the normal of the film's surface. The transmission and reflection spectra are shown in Fig. 34 in the range of 700–1400 nm. The absorption edge significantly shifts toward shorter wavelengths with increasing thickness of 135-CIGS layer as seen in the transmission spectra of Fig. 34(a). It is relatively difficult to indicate the shifts from the reflection spectra in Fig. 34(b). The thickness of all 112-CIGS and 112-CIGS with 135-CIGS capping layer films is approximately $1.8 \mu\text{m}$ while the thickness of 135-CIGS film is only $1 \mu\text{m}$. The transmittance and reflectance were used to determine the absorption coefficient (α) of thin films of thickness d according to

$$\alpha = -\frac{1}{d} \ln \left[\frac{T_{meas}}{(1-R_{meas})^2} \right], \quad (2.10)$$

where T_{meas} and R_{meas} are the transmittance and reflectance measured by the spectrophotometer, respectively [44]. We note that expression (2.10) is an approximation based on the assumption that αd is large near the absorption edge. The energy gap E_g of each sample was obtained using Tauc plot governed by the relation

$$\alpha h\nu = A(h\nu - E_g)^{1/2}, \quad (2.7)$$

where A is a constant, $h\nu$ is the incident photon energy [45, 46]. The E_g of direct bandgap semiconductors can be obtained from the extrapolation of the linear section to the intercept on $h\nu$ axis in the plot of $(\alpha h\nu)^2$ vs. $h\nu$ as shown in Fig. 35. The E_g of 112-CIGS and 135-CIGS were found to be ~ 1.15 and ~ 1.46 eV, respectively. The E_g of 135-CIGS in this work agrees with the E_g of single crystal and polycrystalline 135-CIGS of 1.40 and 1.49 eV, respectively, reported elsewhere [24, 87]. The E_g of 135-CIGS thin film is about 0.3 eV larger than that of 112-CIGS and agrees with others [85, 88]. The absorption edge of thin 135-CIGS capping layer on 112-CIGS shifts toward higher energy, i.e., from ~ 1.15 eV (112-CIGS) to ~ 1.23 eV (300 nm thick of

135-CIGS capping layer). The inset in Fig. 34(a) shows the results of the transmittance of physically stacked layers of 112-CIGS and 135-CIGS by laying two samples together, each of about 1.5 μm thick, e.g., 135-CIGS/SLG on 112-CIGS/SLG (red dash-dotted line), and vice versa (green dashed line). The transmission spectra are almost identical to the transmission of only 112-CIGS (blue solid line) as expected, i.e., 112-CIGS, with sufficient thickness whose E_g is also less than that of 135-CIGS, absorbs all photons. In other words, 135-CIGS does not contribute to the absorption in these physical stacking configurations. However, when the thin 135-CIGS capping layers were deposited on top of 112-CIGS, the absorption edges shift towards shorter wavelengths. This indicates that E_g increased when the thin 135-CIGS was deposited on top of 112-CIGS. It is in contrast to the physically stacked layers of 135-CIGS and 112-CIGS.

The values of x and y of the samples from the EDS measurements as well as the calculated y (y_{cal}) values are listed in Table 8. The values of y_{cal} were obtained by assuming that 135-CIGS layer completely diffused throughout and mixed homogeneously with the underlying 112-CIGS layer. The values of y by the EDS measurements are lower than the calculated ones especially when the 135-CIGS layer becomes thicker, as shown in Table 8, due to more contributions from the x-rays emitted from the lower Cu-depleted layer deposited on top of 112-CIGS. Thus, it is worth mentioning that the y values reported by the EDS measurements of the samples with various thicknesses of 135-CIGS capping layer are not accurate representations of the Cu composition ratio as a whole due to inhomogeneity of Cu across the thickness of the films, especially when the 135-CIGS capping layers become thicker.

Further analysis was carried out to confirm that the widening of the E_g is not artificial due to an incidental change of composition, especially the Ga composition ratio (x). The E_g vs. x was achieved from the optical transmittance and reflectance measurements described above for the 112-CIGS films of $\sim 1.8 \mu\text{m}$ thick deposited with $x = 0, 0.1, 0.2, \dots, 1$ and $y \sim 0.9$ for all samples. The relationship of E_g vs. x for $\text{CuIn}_x\text{Ga}_{1-x}\text{Se}_2$ was obtained from

$$E_{g,\text{CIGS}}(x) = (1-x)E_{g,\text{CIS}} + xE_{g,\text{CGS}} - bx(1-x) \text{ eV}, \quad (4.1)$$

where $E_{g,CIS} = 1.0$ eV, $E_{g,CGS} = 1.65$ eV and the bowing parameter $b = 0.39$ eV of our samples were found from the best fit. Had there been the incidental changes up to 15% of the x values at $x = 0.37$, by the propagation of uncertainty – this would have caused the E_g shift by about 0.03 eV which was less than the shift in the sample with the thinnest 135-CIGS capping layer of 10 nm as shown in Fig. 35. We note that the 15% uncertainty in x at $x = 0.37$, i.e., ($\Delta x \simeq \pm 0.06$), is chosen to be approximately the same as the uncertainty in the atomic% reported by the EDS measurements, i.e., 0.47, 0.47, 0.37 and 0.51 for %Cu, %In, %Ga and %Se, respectively. This suggests that the band gap widening is due to the actual effect of 135-CIGS capping layer rather than the inhomogeneity of the Ga and In fluxes during the deposition process.

It has also been reported that the optical transmission of CIGS thin films with lower Cu atomic ratios (y) exhibits a band gap expansion [87]. For further investigation, we determined the E_g as a function of y from the CIGS thin films with $y = 0.33, 0.65$ and 0.90 and $x \sim 0.37$ for all samples as obtained from the EDS measurements and indicated by open circles in Fig. 36. The relationship between E_g and y is linear, and is given by

$$E_g(y) = -0.53y + 1.63 \text{ eV.} \quad (4.2)$$

The y_{cal} values were chosen to represent the 112-CIGS thin films with 135-CIGS capping layers shown by black solid circles in Fig. 36. We noticed that E_g from the absorbers with 135-CIGS capping layer with thicknesses of 10–80 nm are above the solid line of Eq. (4.2) despite $x \sim 0.37$ as claimed by the EDS measurements while those with 200–300 nm 135-CIGS capping layers almost follow the fitted line for $x = 0.37$, regardless of the higher values of $x = 0.41$ and 0.46 as reported by the EDS measurements, respectively. This suggests that the 10–80 nm 135-CIGS capping layers do not homogeneously mix with the 112-CIGS underlying layers, but affect the widening of E_g of the absorber as a whole more than anticipated by the linear plot of Eq. (4.2). It could also be explained that the thicker 135-CIGS capping layers of 200 and 300 nm that took a slightly longer deposition time (180 s) than those thinner ones (90 s) led to a better intermixing between 135-CIGS and 112-CIGS layers. Then, the increase in E_g from thicker 135-CIGS capping layers was not solely due to the effect

of 135-CIGS capping layer, but rather due to the coalescence of 135-CIGS and 112-CIGS layers.

It is worth noting that the x values of those samples with 200–300 nm 135-CIGS capping layer are quite higher (see Table 8) than those of other thinner ones as reported by the EDS measurements. The higher values of x could arise from i) longer deposition time and ii) substantially Cu-poor composition of thicker capping layers. Both effects allow for the unintended consequence of Ga and In inter-diffusion between the 135-CIGS capping layer and the underlying 112-CIGS film [19]. Substitutions of Cu with Ga or In are also expected [19]. In this case, more Ga atoms can be drawn to the upper region of the films that additionally contribute to the x-ray signals of the EDS detection and thus lead to higher x values than in those films with thinner 135-CIGS capping layer, leaving the underlying layer with x slightly lower than 0.37 set by the deposition fluxes. In other words, inhomogeneous Ga distribution is expected to be the cause of higher x values rather than greater Ga incorporation throughout the bulk of the films. It can be seen that the E_g of the sample with 200 nm 135-CIGS is slightly below the line for $x = 0.37$, while that of 300 nm 135-CIGS deviates further below the line for $x = 0.37$. This suggests that more Ga diffusion occurs in the thicker capping layer leaving the lower part with less Ga than in the sample with 200 nm 135-CIGS. Further verification shows that the E_g of the $\sim 1.8 \mu\text{m}$ thick CIGS films with the uniform $x = 0.46$ and $y = 0.35, 0.65, 0.78$ and 0.90 are much higher than those of $x = 0.37$ as indicated by the triangles with dashed line in Fig. 36. These samples were fabricated using the single-stage deposition process to avoid the diffusion of Ga. The x and y ratios were confirmed by the EDS. Similarly, the E_g vs. y for CIS ($x = 0$) indicated by the diamonds with dashed line are also shown for lower boundary in the plot of Fig. 36. Moreover, in the CIGS films with non-uniform x , the E_g obtained from the transmittance and reflectance measurements are, in general, corresponding to the lowest transition due to the actual minimum x value of the main portion of the film and analogous to what is described and shown in the inset of Fig. 34(a). Thus, the results suggest that the widening of E_g in the samples with 200–300 nm 135-CIGS capping layer should also be due to the effect of the 135-

CIGS covered layers rather than the effect of inadvertent increase in Ga content in the bulk of the films.

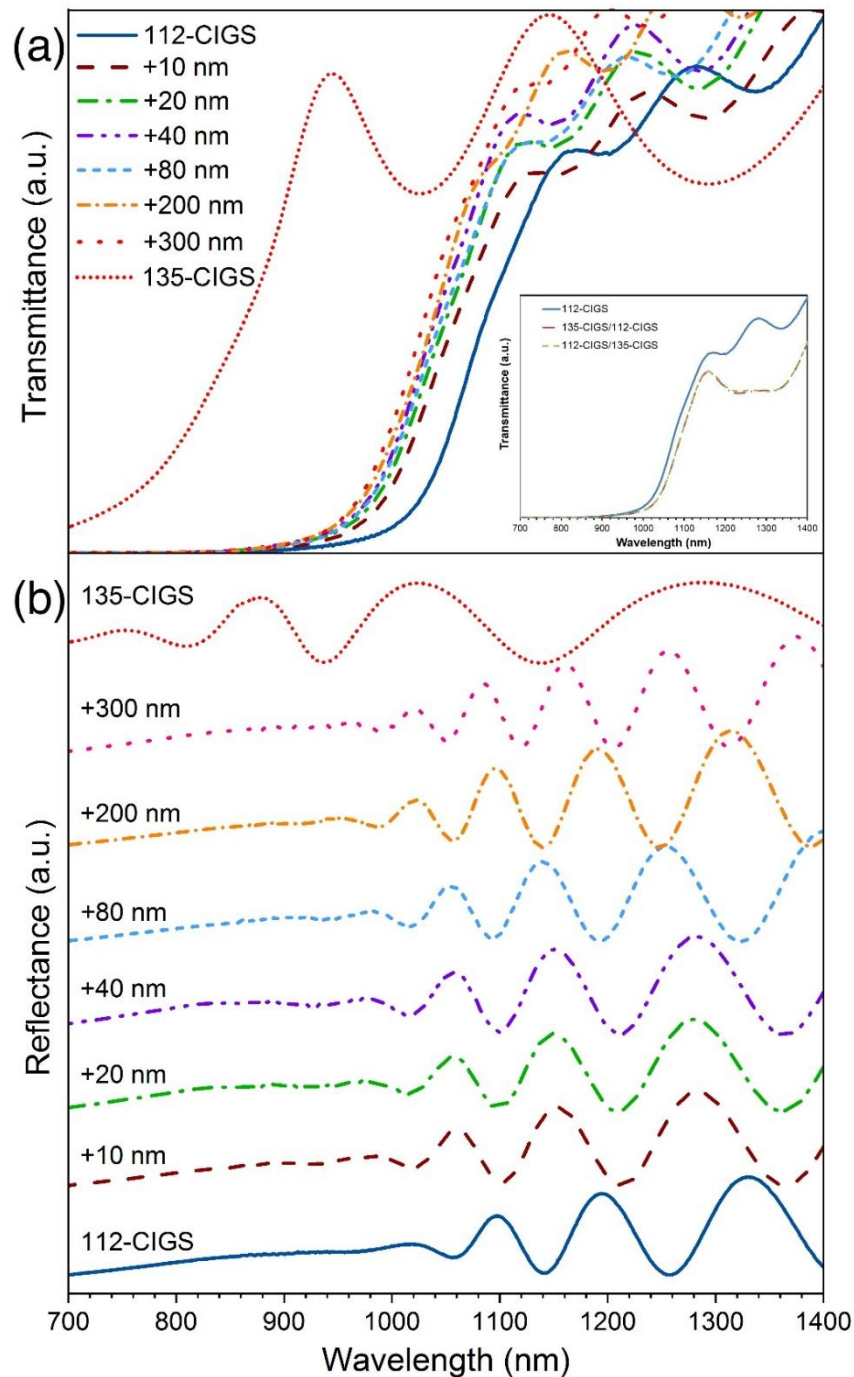


Figure 34: Plots of (a) optical transmittance and (b) reflectance spectra of 112-CIGS, 135-CIGS and 135-CIGS/112-CIGS with various thicknesses of 135-CIGS; 10, 20, 40, 80, 200 and 300 nm. Inset in (a) shows the results of the transmittance of physically stacked layers of 112-CIGS and 135-CIGS by laying two samples together.

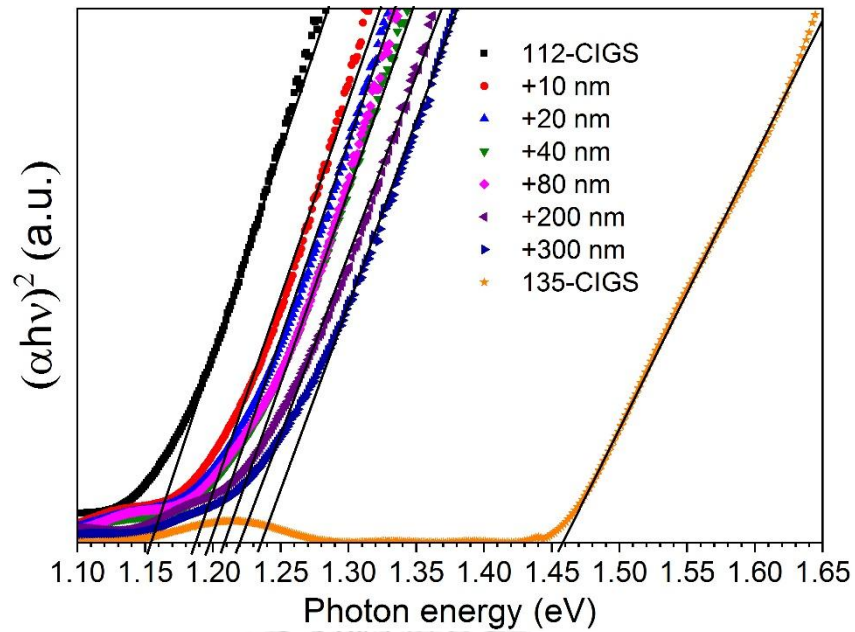


Figure 35: Tauc plot of $(\alpha hv)^2$ vs. incident photon energy (hv) for 112-CIGS, 135-CIGS and 135-CIGS/112-CIGS with various thicknesses of 135-CIGS. A straight line is extrapolated to determine band gap energy (E_g).

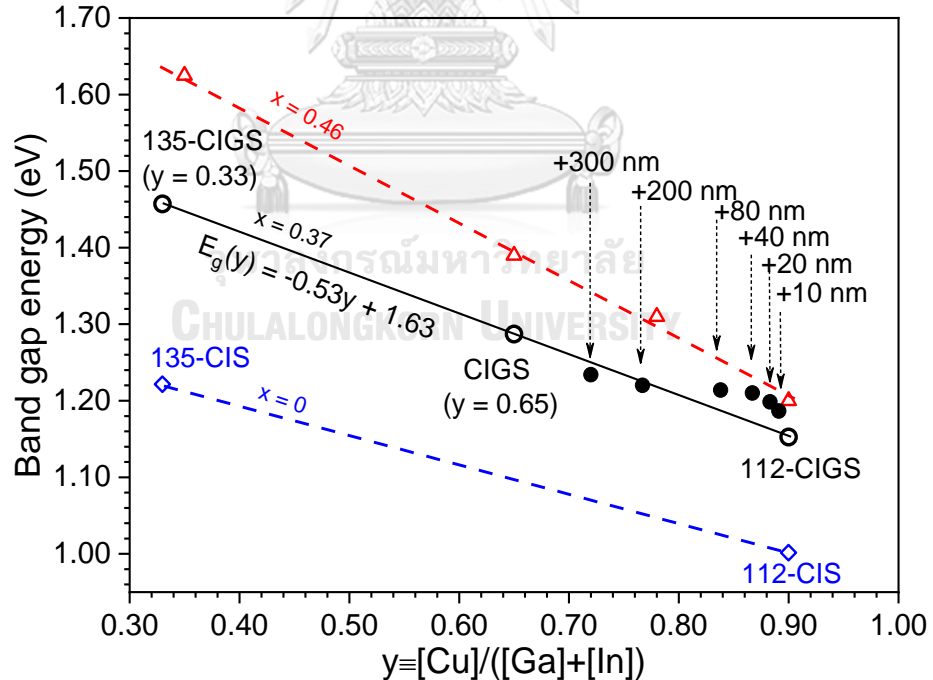


Figure 36: A plot of band gap energy vs. Cu-atomic ratios. Open circles are from the measurements with $y = 0.33, 0.65$ and 0.90 . Solid black circles represent the 112-CIGS with 135-CIGS capping layer with the thickness of 10-300 nm using calculated values of y .

Table 8: Ga composition ratio (x), Cu composition ratio (y) obtained from the EDS measurements and y_{cal} as calculated from overall thickness of the films.

Samples	$x = [Ga]/([Ga]+[In])$	$y = [Cu]/([Ga]+[In])$	y_{cal}
112-CIGS	0.37	0.91	0.90
+10 nm	0.39	0.87	0.89
+20 nm	0.36	0.86	0.88
+40 nm	0.36	0.82	0.87
+80 nm	0.37	0.80	0.84
+200 nm	0.41	0.72	0.77
+300 nm	0.46	0.62	0.72
135-CIGS	0.39	0.31	0.33

Table 9: XRD peak position of (112) and (220) phases, shift of peak position, ratio of lattice parameters (c/a) and volume of unit cell of 112-CIGS, 135-CIGS and 135-CIGS/112-CIGS.

Samples	2 θ peak position (degree)		$\Delta(2\theta)$ (degree)		c/a		Volume of unit cell (\AA^3)	
	(112)	(220)	(112)	(220)	(112)	(220)	(112)	(220)
112-CIGS	26.98	44.75	-	-	1.999	1.995	374.2	374.2
+10 nm 135-CIGS	27.07	44.85	0.09	0.10	1.993	1.989	370.6	370.5
+80 nm 135-CIGS	27.10	44.91	0.12	0.16	2.006	1.991	369.4	369.3
+200 nm 135-CIGS	27.13	44.93	0.15	0.18	2.004	1.986	368.2	368.1
135-CIGS	27.25	45.33	0.27	0.58	2.010	2.010	363.4	363.4

4.5 Crystal structure

The broad XRD spectra covering 2θ of 5–80° showing (112) and (220)(204) chalcopyrite phases of 112-CIGS, 135-CIGS and 135-CIGS/112-CIGS with various thicknesses of 135-CIGS films are presented in Fig. 37(a). The (110) plane of Mo layer on SLG substrate is also visible and can be used to align the samples for the XRD measurements. The normalized intensities of (112) and (220)(204) chalcopyrite phases of the samples were determined for the XRD peak shift at the diffraction angle of 25°–28° and 44°–46°, respectively, using Lorentzian function fitted to the XRD data as illustrated in Fig. 37(b)–(c). It can be seen that the peak positions of both (112) and (220)(204) phases of CIGS shift toward larger diffraction angle as the thickness of 135-CIGS capping layer increases. It can also be noticed in Fig. 37(c) that the (220) and (204) phases almost coincide with each other for the 112-CIGS. The shift of the (220) phase at higher angle was found to be slightly larger than that of the (112) phase as summarized in Table 9.

For simplicity, further analysis of the XRD peak shifting shall be done on the (112) phase. The calibration curve for the 2θ position of the (112) phase of CIGS with various Ga composition ratios was obtained from the XRD measurements of the 1.8 μm 112-CIGS thickness with $x = 0, 0.1, 0.2, \dots, 1$ and $y \sim 0.9$ for all samples. The 2θ position of the (112) peak vs. x was found from linear regression to be

$$2\theta_{(112)}(x) = 1.04x + 26.56^\circ. \quad (4.3)$$

This is then used to propagate the uncertainty in x to the uncertainty in the shift of the XRD peak of the (112) phase. The 15% uncertainty in Ga composition ratio or x at $x = 0.37$ or $\Delta x \simeq \pm 0.06$ was considered similar to that previously discussed and thus led to the uncertainty in the (112) peak of about 0.06°. Here, in this work, the shifts of the (112) peak due to the 135-CIGS capping layers are all greater than 0.06°.

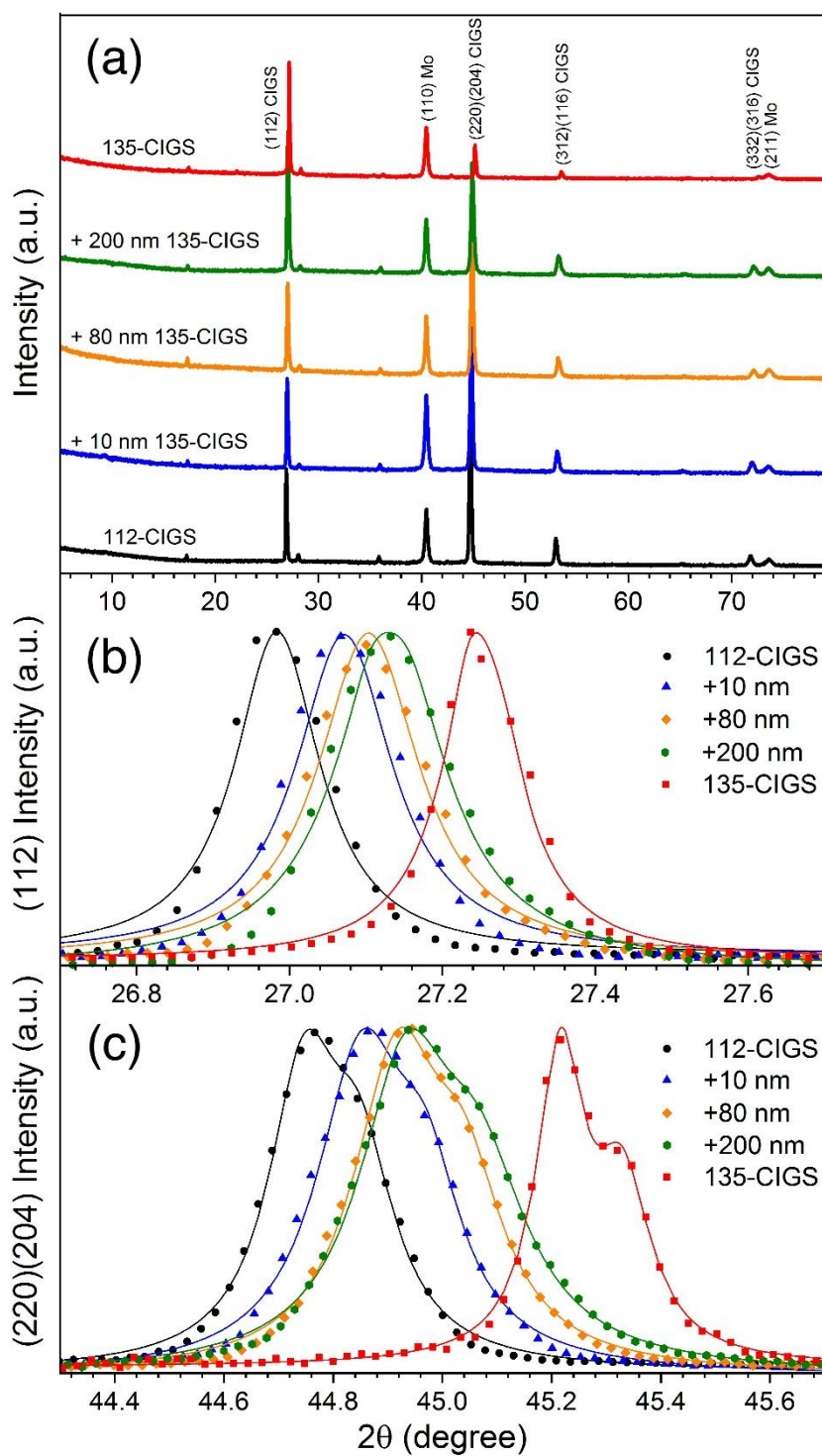


Figure 37: The XRD patterns showing (a) broad spectra, (b) (112) plane and (c) (220)(204) planes of 112-CIGS, 135-CIGS and 135-CIGS/112-CIGS with 135-CIGS capping layer of 10, 80 and 200 nm thick.

Additionally, we noticed that there is no peak broadening in the XRD pattern when the 135-CIGS covered layer becomes thicker, e.g., the sample with 200 nm 135-CIGS covered layer. Had the x value of the sample with 200 nm 135-CIGS covered layer been 0.41 to represent the bulk of the film, its 2θ peak position would have been at 26.99° for $y = 0.9$ according to Eq. (4.3). In fact, the 2θ peak position of this +200 nm 135-CIGS covered layer is at 27.13° , as indicated in Table 9, which is higher than the value expected from Eq. (4.3). This is mainly due to the effective y value being less than 0.9 caused by the 135-CIGS capping layer. The reasons above suggest that most lower portion of the film should have x slightly less than 0.37 and the 135-CIGS capping layers affect the crystal structure of the underlying 112-CIGS as a whole. These results are unlikely due to the incidental changes of the Ga composition ratio of the bulk of the film despite the fact that it can also cause the XRD peak shift.

The 2θ peak positions, the shift of 2θ peak positions, the calculated lattice parameters in terms of c/a and the volume of the unit cell ($V = a^2c$) from both (112) and (220) phases are listed in Table 9. 112-CIGS and 135-CIGS gave the largest and smallest volume of the unit cell, respectively. It was found that the volume of the unit cell decreased as the thickness of 135-CIGS capping layer increased. The E_g is related to the lattice constants or the volume of the unit cell, i.e., as the volume of the unit cell decreases, the E_g is widened. When the thinner 135-CIGS layer is on top of 112-CIGS, the lattice mismatch between 135-CIGS and 112-CIGS layers can induce strain at the interface of 135-CIGS and 112-CIGS layers. For the thin 135-CIGS capping layer of 10–80 nm, the whole 112-CIGS bottom layer accommodate its crystallographic structure by reducing its unit cell size which can cause the decrease in both lattice parameters (a and c) and the volume of the unit cell, as listed in Table 9. Thus, these thin 135-CIGS capping layers can cause a significant shift toward larger 2θ and also increase the E_g of the underlying 112-CIGS. The unit cell contraction has also been observed with decreasing Cu content in bulk CIGS [90]. Moreover, the XRD patterns shown in Fig. 8(b)–(c) are unresolvable for separated 112-CIGS and 135-CIGS structures. The estimated full width at half maximums (FWHMs) for every XRD pattern are approximately 0.08° . The broadening of 135-CIGS/112-CIGS layers cannot be observed. For those samples with 135-CIGS

capping layer thicker than 200 nm, the decrease in the volume of the unit cell should be less affected by the strain at the interface induced by 135-CIGS capping layer, but rather by the diffusion of elements, especially group-III elements, from 135-CIGS upper layer into 112-CIGS bottom layer to form a substantial amount of Cu vacancies.

4.6 Raman spectra and Raman shift

Commonly, the 135-CIGS has the space group $\bar{P}42c$ and point group $\bar{4}2m$ which is known as ordered vacancy compounds (OVCs) [91]. In order to see if 135-CIGS is chalcopyrite structure or not, the Raman measurement is used to investigate the vibrational spectra modes of 112-CIGS and 135-CIGS thin films. Moreover, the Raman shift is investigated to observe the stress and strain in 135-CIGS/112-CIGS samples. From the XRD results in Table 9, the lattice parameters calculated for 112-CIGS and 135-CIGS are: $a = 5.720 \text{ \AA}$, $c = 11.437 \text{ \AA}$ and $a = 5.654 \text{ \AA}$, $c = 11.367 \text{ \AA}$, respectively. These values are fairly comparable with the unit cell of 135-CIGS being slightly smaller. Then, what is expected for Raman measurement is the vibrational spectra of 112-CIGS chalcopyrite structure and 135-CIGS ordered vacancy compound must be nearly the same as well. The plot in Fig. 38 shows the Raman spectra of 112-CIGS, 135-CIGS and 135-CIGS/112-CIGS with 10 and 200 nm thick of 135-CIGS. According to the character for the point group $\bar{4}2m$ of chalcopyrite structure, the representations for the zone center Raman-active optical modes in these structures are: $1A_1+3B_1+3B_2+6E$. Then, the strongest Raman spectra of 112-CIGS, 135-CIGS and 135-CIGS/112-CIGS at 168.26 cm^{-1} , 169.44 cm^{-1} , 169.02 cm^{-1} and 169.31 cm^{-1} are due to the symmetric A_1 mode which results from the motion of Se atoms with the cations remaining at the rest. These values are in the range that is generally observed in the Raman spectra of chalcopyrite structure [92, 93] at 300K. Both compressive and tensile strain can be determined with compressive strain giving an upward and tensile strain a downward shift from the unstrained 169.44 cm^{-1} of 135-CIGS shift. For thinner 135-CIGS capping layer, 112-CIGS has larger lattice constant than 135-CIGS. Thus, the 10 nm thick of 135-CIGS grown on 112-CIGS sample is under tensile strain leading to downward shift. Moreover, the shift of 200 nm thick of 135-CIGS is under the relaxed strain because of the elemental diffusion as mentioned above in XRD section. Then, these Raman shifts can confirm the chalcopyrite

structure of 135-CIGS and strain in the heterostructure of 135-CIGS/112-CIGS with thin 135-CIGS capping layer.

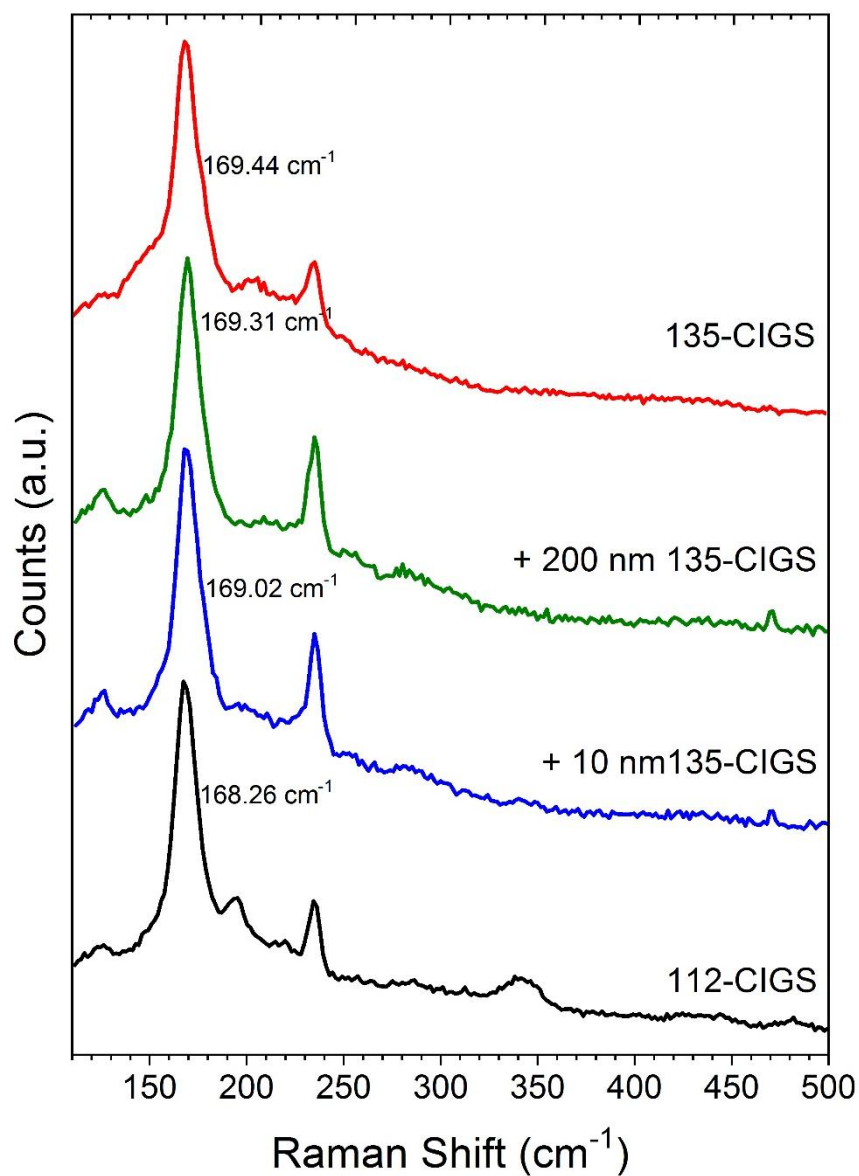


Figure 38: Raman spectra of 112-CIGS, 135-CIGS and 135-CIGS/112-CIGS with 135-CIGS capping layer of 10 and 200 nm thick.

4.7 J-V characteristics and QE of CIGS devices

The photovoltaic parameters of the CIGS solar cells, e.g., V_{oc} , J_{sc} , FF and power conversion efficiency (η) with various thicknesses of 135-CIGS film are shown by the box chart in Fig. 39. The upper and lower bars represent the maximum and minimum values, respectively. The numbered solid squares indicate the average values. The upper and lower boundaries of the box correspond to the upper and lower quartile, and the middle line is the median for the statistical analysis of the devices. Higher V_{oc} was achieved in range from 650 to 670 mV for 135-CIGS thickness below 80 nm. The thinnest 135-CIGS capping layer of 5 nm gives the highest value of V_{oc} . It is shown that the V_{oc} decreases when the thickness of 135-CIGS increases. The devices with 200 nm thick 135-CIGS have the lowest V_{oc} which are significantly less than the standard 112-CIGS devices. Short-circuit current densities (J_{sc}) are not significantly different among the 135-CIGS thicknesses of 5–200 nm. Fill factor (FF) of 200 nm thick 135-CIGS capping layer is significantly lower than others due to lower V_{oc} . The maximum conversion efficiency of the devices with 135-CIGS thickness below 10 nm is a bit lower than the standard 112-CIGS devices due to a slight decrease in the value of J_{sc} . The thin 135-covered layers affect the increase in V_{oc} without significant loss of J_{sc} which could be caused by the suppression of recombination at the interface. The larger valence band offset (ΔE_v) of less than 0.4 eV can create a sufficient barrier to eliminate interface recombination, thus the V_{oc} is increased [21]. However, the V_{oc} is reduced significantly with increasing thickness of 135-CIGS film to 200 nm. The decrease in the values of V_{oc} , FF and efficiency of the devices as the thickness of 135-CIGS increases is inferred by higher defect concentration in the 135-CIGS layer, e.g., a neutral defect of $2V_{Cu}+In_{Cu}$ (Cu vacancy and In on Cu site defects), deep defect of III_{Cu} (the substitution of group-III elements on Cu sites) and also excessive V_{Cu} that may, on the other hand, cause the interface recombination [18].

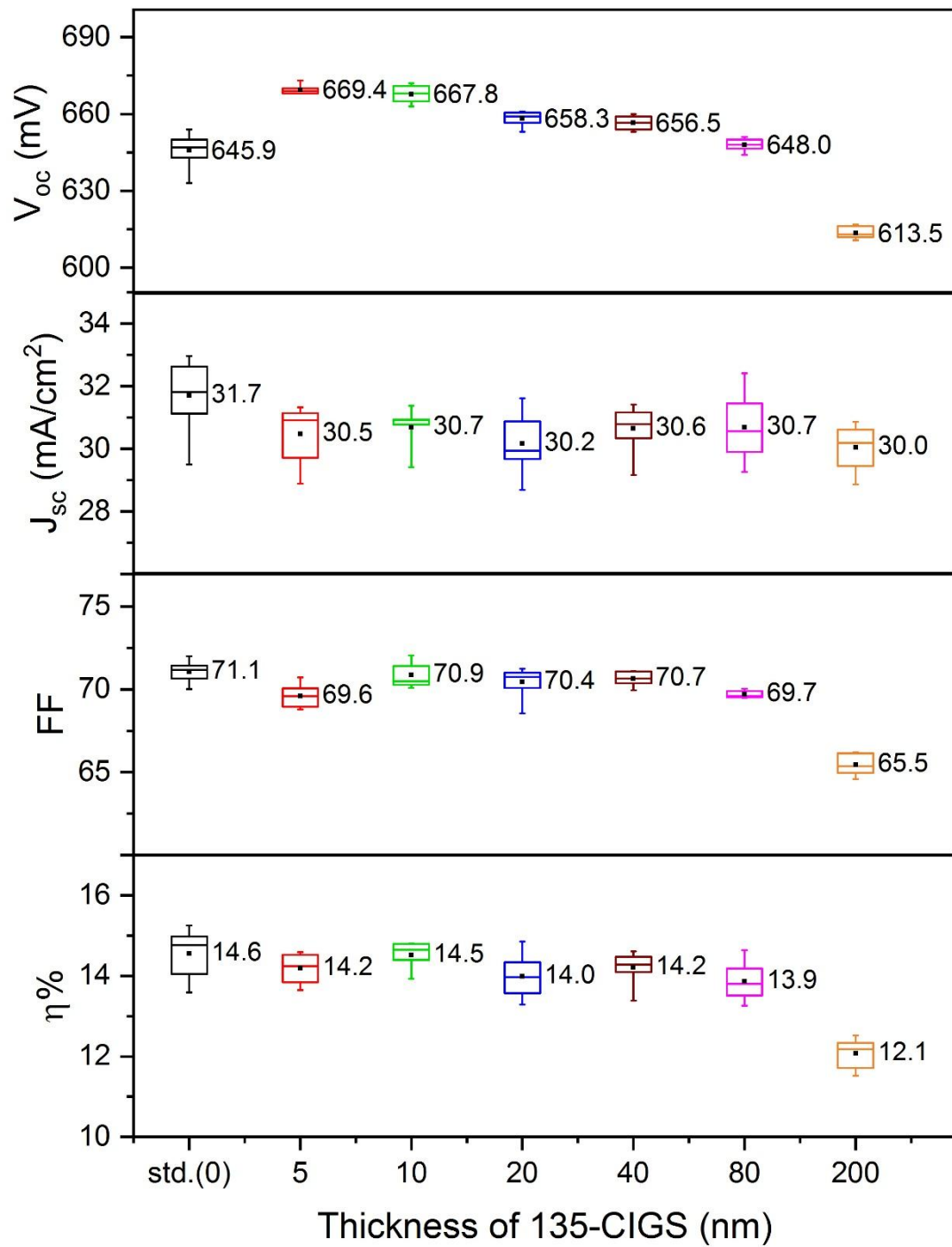


Figure 39: Plots of solar cell parameters of 112-CIGS and 135-CIGS/112-CIGS.

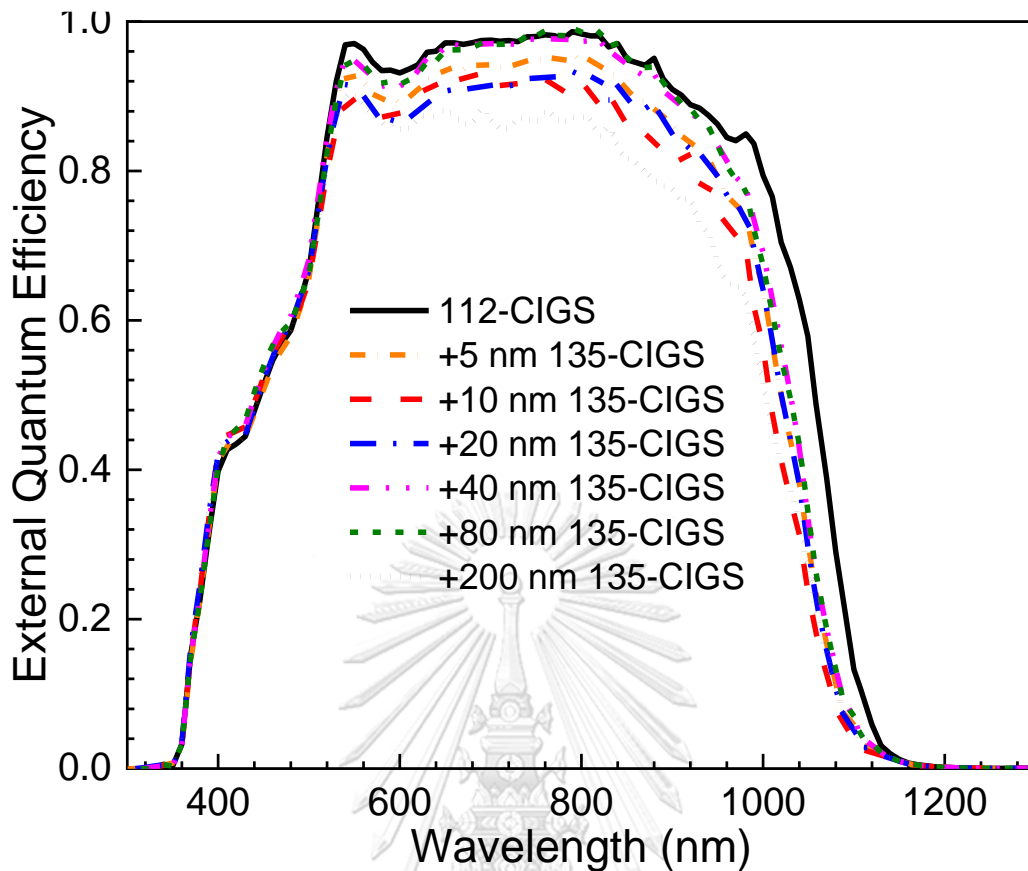


Figure 40: External quantum efficiency of 112-CIGS and 135-CIGS/112-CIGS solar cells.

The EQE of 112-CIGS and those with various thicknesses of 135-CIGS capping layer solar cells are shown in Fig. 40. The standard 112-CIGS devices show the highest generated photocurrent from the light absorption corresponding to the maximum value of J_{sc} , of 33 mA/cm^2 as shown in Fig. 39. The generated photocurrents of all 135-CIGS layers grown on top of 112-CIGS are slightly lower than that of the 112-CIGS device due to the loss of photocurrent in the long wavelength region. The cut-off wavelengths of EQE are also qualitatively consistent with the absorption edge of the CIGS absorber films as shown in the transmission spectra in Fig. 34(a).

4.8 Summary remarks

It has been demonstrated that very thin layer of 135-CIGS on the surface of 112-CIGS absorber layer significantly affects physical, optical and photovoltaic properties of photon absorber layer of CIGS thin film solar cells. However, surface

observation techniques such as AFM, FESEM cannot resolve the 135-CIGS capping layer when its thickness is less than 40 nm. On the other hand, optical transmission and XRD measurements clearly show the effect of 135-CIGS capping layer in the shift of absorption edge and the diffraction peak, respectively. The increase in the thickness of 135-CIGS capping layer leads to the shift of XRD peak towards larger 2θ position that results in the decrease in the volume of unit cell and thus the increase in E_g of the underlying 112-CIGS layer. This is consistent with the shift of absorption edge towards shorter wavelengths. For the device performance, the V_{oc} is increased from 646 mV (without 135-CIGS) to ~670 mV (with 5–10 nm 135-CIGS) with a slight decrease in the value of J_{sc} . The power conversion efficiencies are comparable between the devices with and without 135-CIGS capping layer but the increase in V_{oc} is directly due to the existence of the 135-CIGS capping layer. However, excessive thickness of 135-CIGS capping layer can also deteriorate the device performance. Lastly, for future investigation, the optical measurement technique such as temperature-dependent photoluminescence may be useful for investigating the electronic structures of this pseudo-homojunction 135-CIGS/112-CIGS or other ordered defect compound covered layers to verify the anticipated valence band offset (ΔE_v) in addition to the indirect evidences of widening of E_g and the increase in V_{oc} as reported here. Also, different deposition techniques that intrinsically deliver Cu-deficient surface to 112-CIGS could be beneficial to the improvement of CIGS solar cells.

CHAPTER V

PHOTOLUMINESCENCE OF 135-CIGS/112-CIGS HETEROSTRUCTURE SYSTEM

In this chapter, temperature-dependent and power-dependent photoluminescence (PL) spectra of 112-CIGS, 135-CIGS, 135-CIGS/112-CIGS and 112-CIGS/135-CIGS thin film heterostructures are investigated. The broad spectra are observed, especially in 135-CIGS and 112-CIGS/135-CIGS thin films. The nature of PL emission depends on temperature of 112-CIGS and 135-CIGS/112-CIGS that is different from 135-CIGS and 112-CIGS/135-CIGS. In this research, donor-acceptor pair (DAP) transition is mainly observed in the polycrystalline films and identified by their activation energies. The free-to-bound (FB) transition is only observed for 112-CIGS and 135-CIGS/112-CIGS heterostructures. Moreover, the effect of interference in photoluminescence spectra is also discussed here.

5.1 PL of 112-CIGS, 135-CIGS thin films and 135-CIGS/112-CIGS heterostructure

The excitation power dependence of PL spectra of 112-CIGS, 135-CIGS and 135-CIGS/112-CIGS with 10 nm thick 135-CIGS from 0.1 mW to 35 mW at 10 K are shown in Fig. 41. The PL spectra show broad donor-to-acceptor pairs (DAPs) transition for 112-CIGS and 135-CIGS/112-CIGS films. It can be seen in Fig. 41 that the broad emission in the PL spectra of 112-CIGS and 135-CIGS at high excitation power can be resolved into two peaks when the excitation intensity is reduced. The two resolved peaks at low excitation are identified as donor-to-acceptor pairs (DAPs) and free (conduction band)-to-bound (acceptor) (FB) transitions. Normally, the nature of peak position of the FB transition is temperature and excitation power independent, whereas the DAPs showed blue-shift for a p-type and red-shift for an n-type semiconductor [94]. It is worth to point out that the broad peak of 135-CIGS cannot be resolved to observe FB and DAP transitions when the excitation power is decreased. There is no significant shift of the peak in the excitation power for the 135-CIGS. In addition, the emission from the 135-CIGS cannot be noticed in the 135-CIGS/112-CIGS heterostructure.

Fig. 42–Fig. 44 show the temperature-dependent PL spectra of 112-CIGS, 135-CIGS/112-CIGS with 10 nm thick 135-CIGS from 10–300 K and 135-CIGS from 10–200 K. Inset is the fitting result of PL spectrum at 10 K. The broad peaks are observed in range of 1.07–1.12 eV for 112-CIGS and 1.09–1.14 eV for 135-CIGS/112-CIGS which the energy range for 10 nm thick 135-CIGS capping on 112-CIGS is slightly shifted to higher energy about 20 meV. The peak energy increases by reducing of Cu elements for 135-CIGS thin film. With increase in temperature, the transition to higher energy is apparent. The peak positions of the PL measurements from 10–300 K at maximum excitation power are plotted as a function of temperature and shown in Fig. 46. The PL emissions from 112-CIGS and 135-CIGS/112-CIGS show blue-shift as the temperature increases that are the nature of the DAP transition of a p-type semiconductor. It is noted that the peak energy at 300 K coincides with the FB transition at 10K. On the contrary, a 135-CIGS shows red-shift as the temperature increases that is a characteristic of an n-type semiconductor. The activation energy can be calculated from the two-channel model of Arrhenius function [95] as shown in Fig. 45;

$$I(T) = \frac{I(0)}{1 + A \exp\left(\frac{-E_{a1}}{k_B T}\right) + B \exp\left(\frac{-E_{a2}}{k_B T}\right)}, \quad (5.1)$$

where $I(0)$ is the PL emission intensity at 0 K, E_{a1} and E_{a2} are the activation energies in the low and high temperature regime, respectively, A and B are fitting parameters and k_B is the Boltzmann constant.

The types of donor and acceptor in the 112-CIGS and 135-CIGS/112-CIGS could be regarded as Se vacancies (V_{Se}) and Cu vacancies (V_{Cu}), respectively, and their estimated activation energies are ~10–30 meV for V_{Se} and ~50–90 meV for V_{Cu} compared with the values of 5–10 meV for V_{Se} and 80–90 meV for V_{Cu} reported elsewhere [96]. The slight discrepancies between these results and others are due to the difference of the Ga concentration. According to their calculated activation energies for 112-CIGS and 135-CIGS/112-CIGS thin films, the defect states can be interpreted to an energy level diagram illustrated in Fig. 47(a) and Fig.47(b).

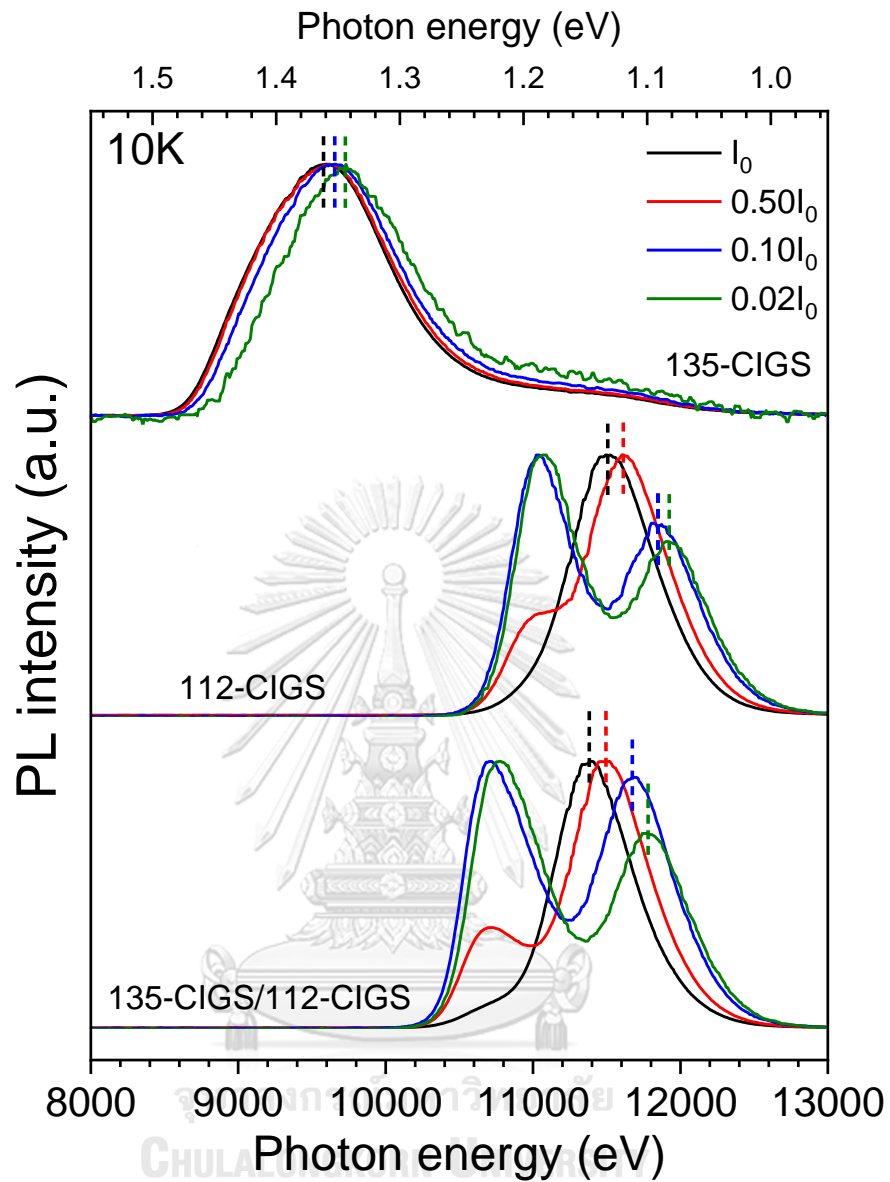


Figure 41: The PL spectra of 135-CIGS, 112-CIGS and 135-CIGS/112-CIGS thin films at 10 K. The black line is for the high power (35 mW) and the red line, green line and blue line are for the low excitation power.

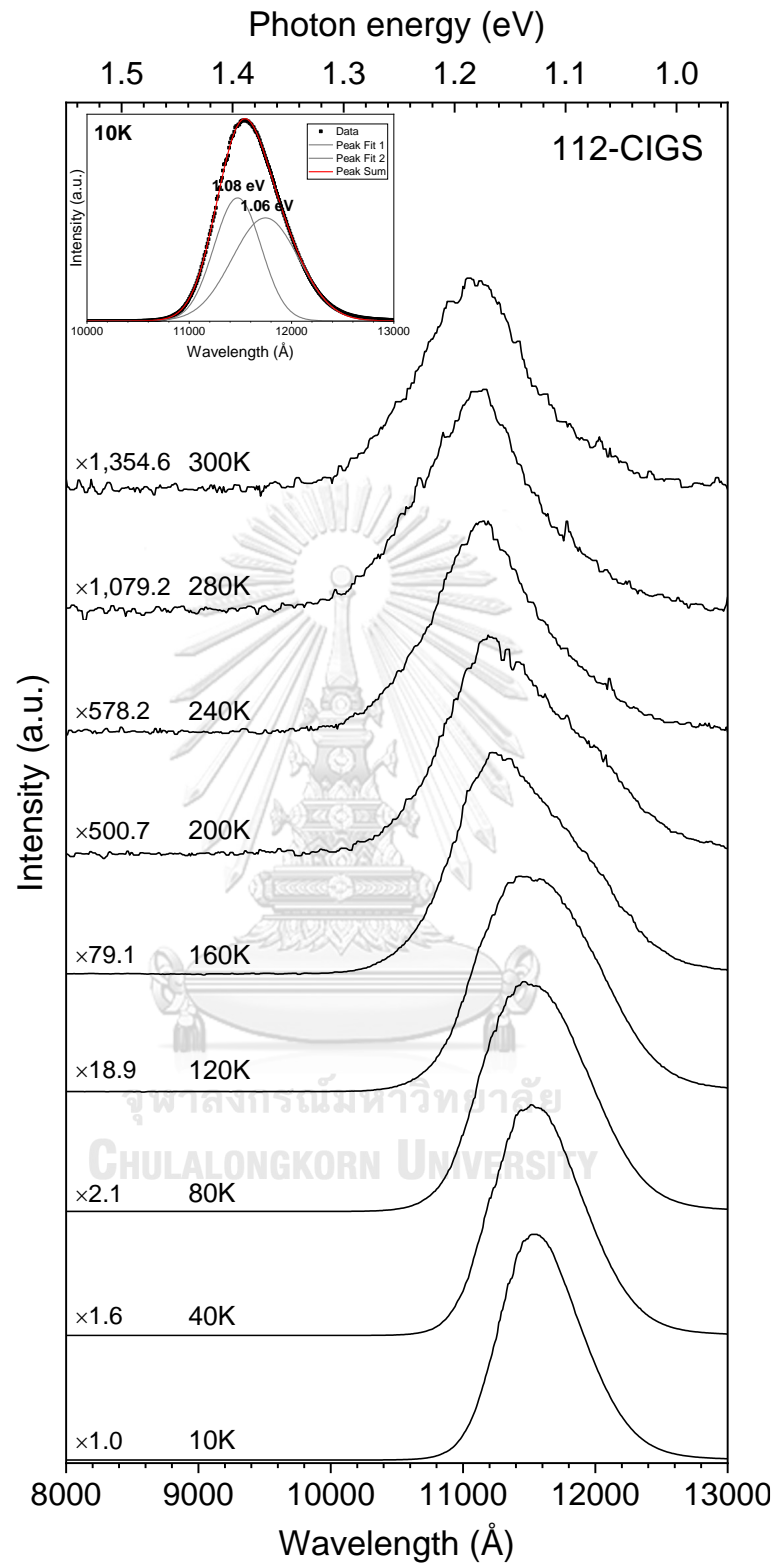


Figure 42: The PL spectra of the 112-CIGS thin film under temperatures from 10 K to 300 K. Inset is the fitting result of PL spectrum at 10 K using Gaussian distribution.

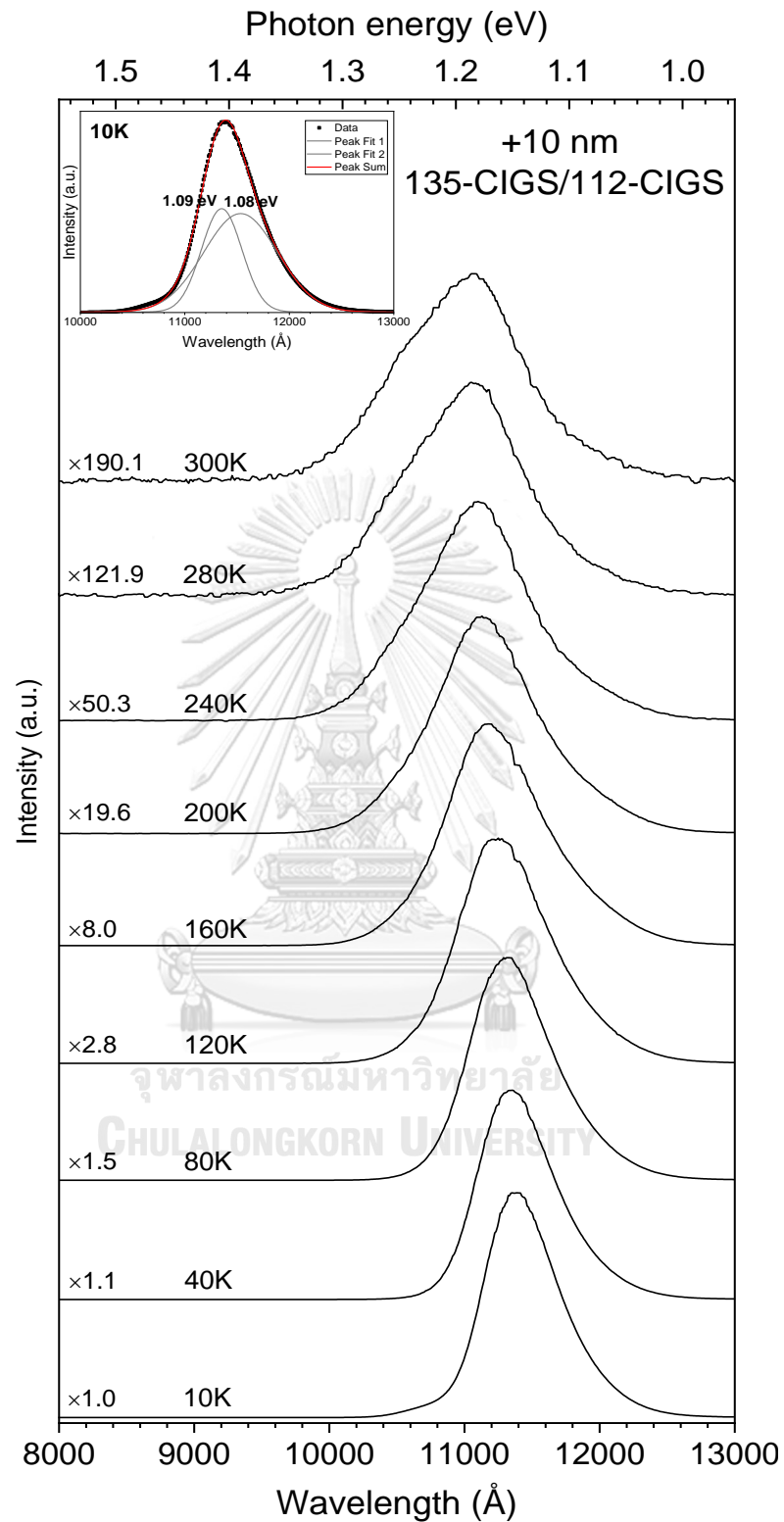


Figure 43: The PL spectra of the 135-CIGS/112-CIGS thin film with 10 nm thick of 135-CIGS capping layer under temperatures from 10 K to 300 K. Inset is the fitting result of PL spectrum at 10 K using Gaussian distribution.

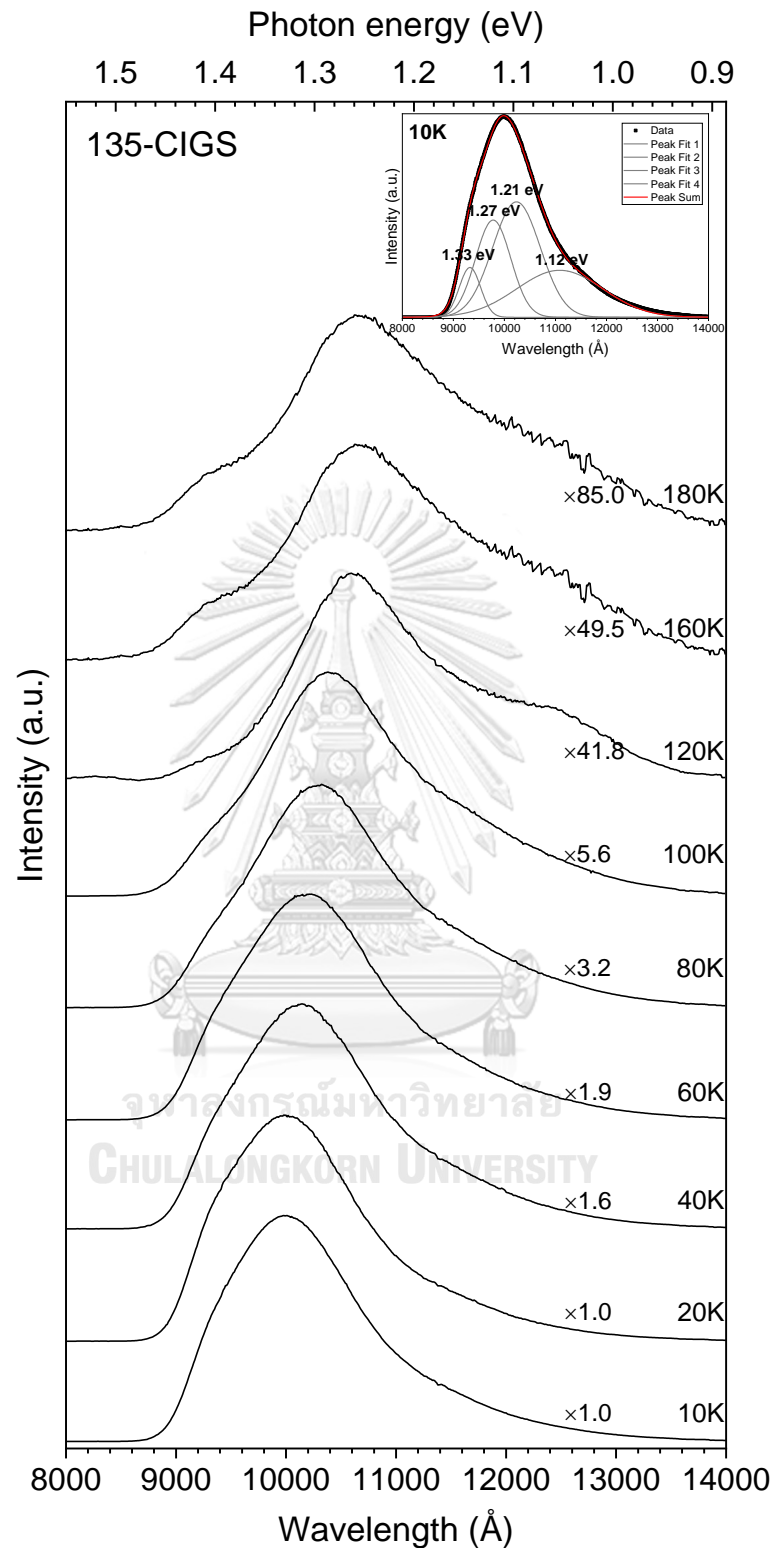


Figure 44: The PL spectra of the 135-CIGS thin film under temperatures from 10 K to 200 K. Inset is the fitting result of PL spectrum at 10 K using Gaussian distribution.

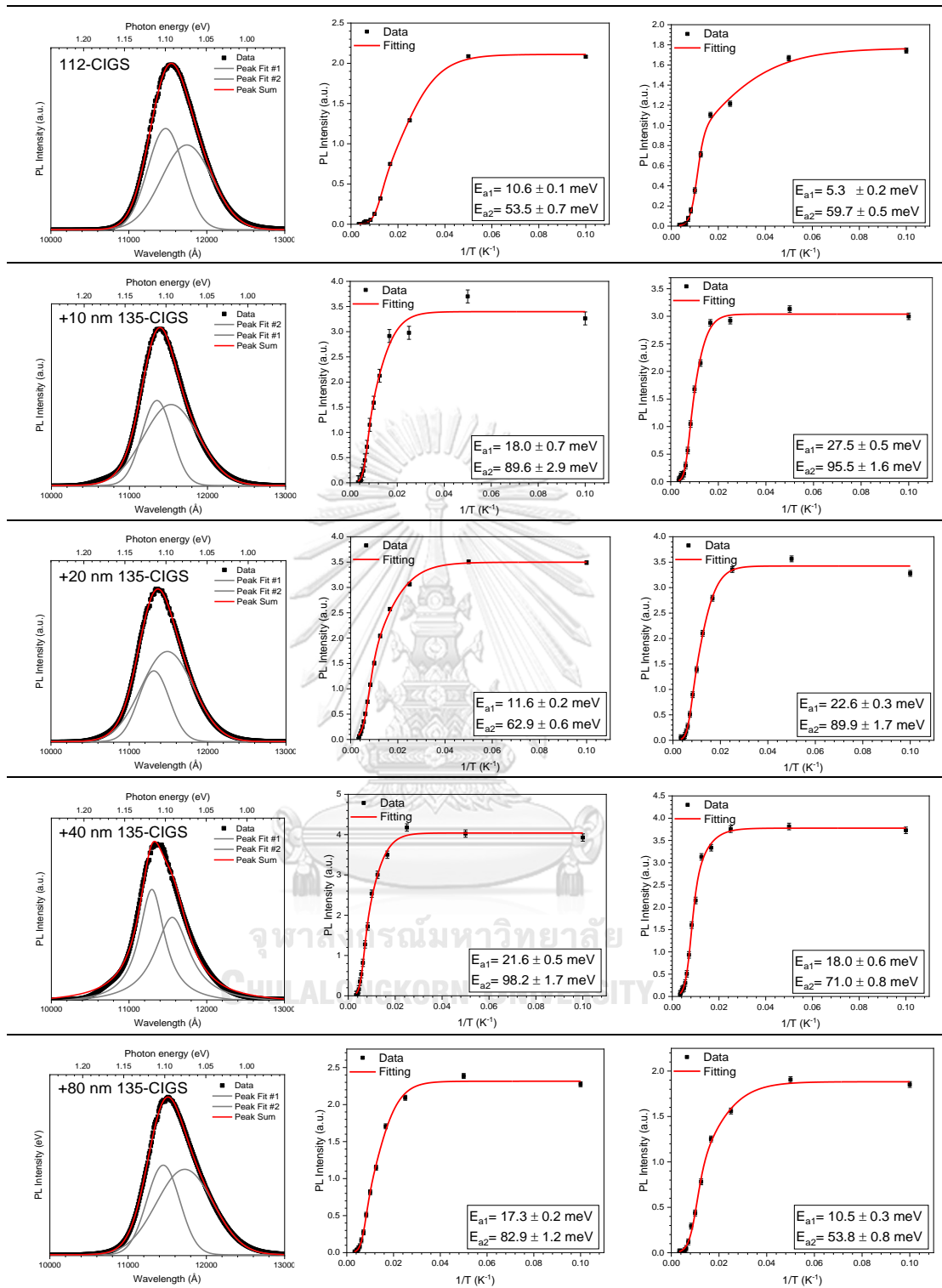


Figure 45: The Arrhenius plot of temperature-dependent PL intensity vs. $1/T$ for fitting peak 1 and peak 2.

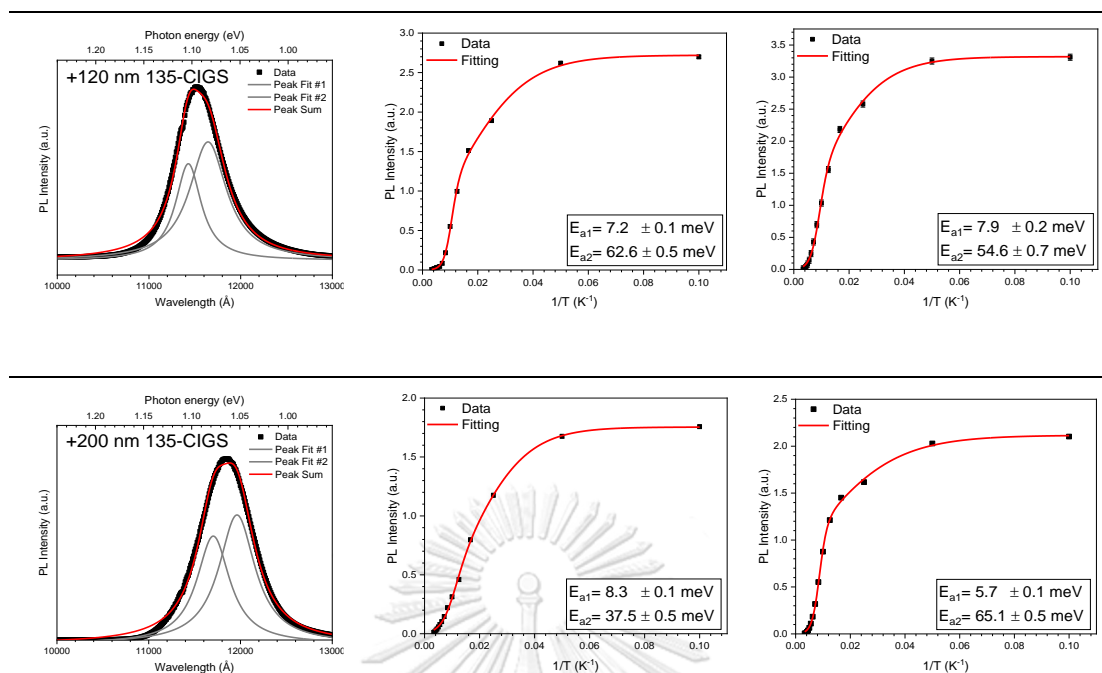


Figure 45: (Continued) The Arrhenius plot of temperature-dependent PL intensity vs. $1/T$ for fitting peak 1 and peak 2.

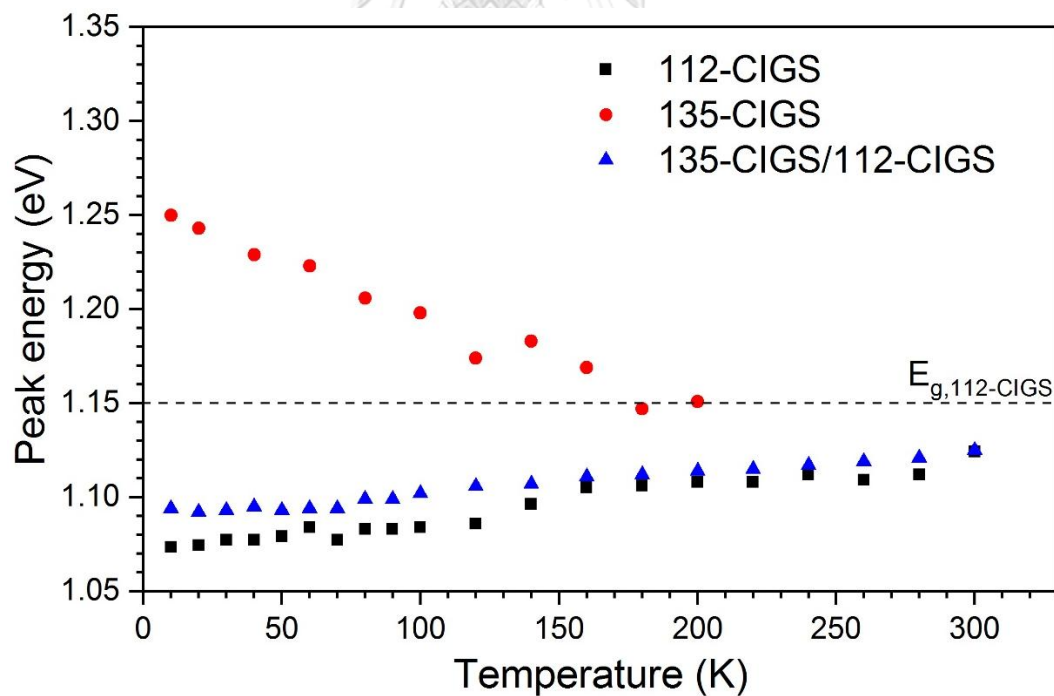


Figure 46: Peak energy at high excitation power plotted as a function of temperature from 10–300 K for 112-CIGS, 135-CIGS and 135-CIGS/112-CIGS.

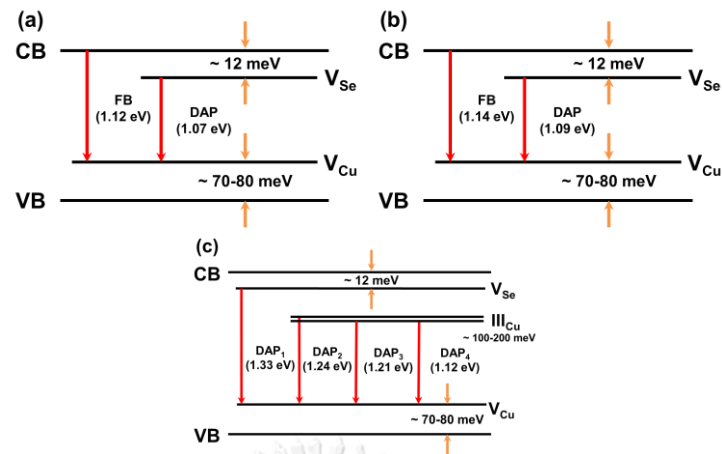


Figure 47: The energy level diagram of (a) 112-CIGS (b) 135-CIGS/112-CIGS and (c) 135-CIGS thin films.

For 135-CIGS thin film, it shows a broadening shape due to the possible various defects in the film. Then, in the PL spectrum, there are four fitting curves using Gaussian function. The energy level diagram of 135-CIGS is shown in Fig. 47(c). It composes of only DAPs transitions. It has been known that 135-CIGS is the n-type semiconductor, thus, the dominant defect is a donor. The possible donor types in 135-CIGS thin film are In_{Cu} (indium on Cu site) ($E_a \sim 100\text{--}200$ meV), and V_{Se} (selenium vacancy) ($E_a \sim 60\text{--}80$ meV) [97-103].

The PL spectra among the various thicknesses of 135-CIGS capping on 112-CIGS at 10 K are compared to that of 112-CIGS thin film as shown by Fig. 48. The PL peak position of 112-CIGS is at 1.12 eV while the PL peak energies of thin 135-CIGS capping layer of 1–40 nm are approximately at 1.14 eV, higher than that of 112-CIGS film by 20 meV. It is quite possible that there is the strain for only thinner 135-CIGS capping layer of 135-CIGS/112-CIGS heterostructure. Then, the activation energies of these defects may form at higher energy. However, the PL peak energy is shifted to the original position for 80 nm 135-CIGS capping layer and then shifted towards lower energy as increasing the thickness of 135-CIGS layer for 120–200 nm. The shifted spectra towards lower energy for thick 135-CIGS capping layer is possible due to the intermixing between 135-CIGS and 112-CIGS layer as mentioned in Chapter IV. As a result, the y value ($y \equiv [\text{Cu}]/([\text{Ga}]+[\text{In}])$) is lower and could form the concentration of deeper defect levels that cause the peak shifted.

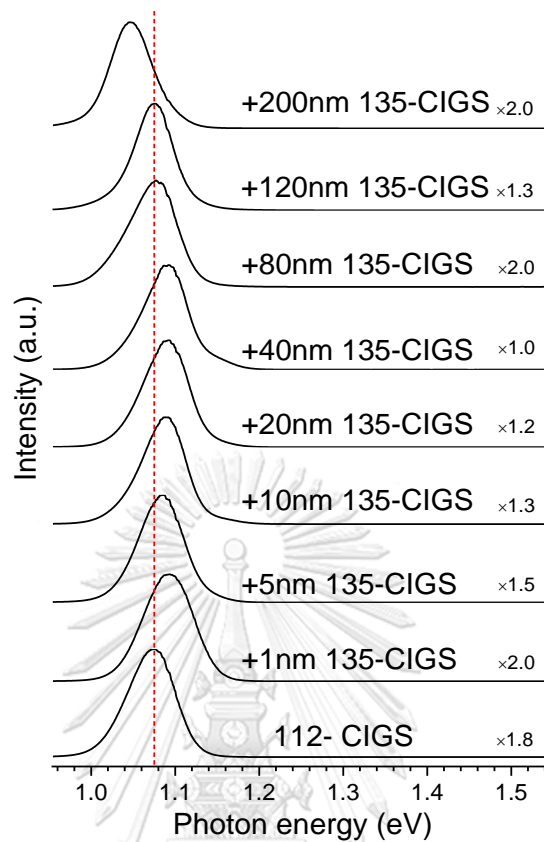


Figure 48: PL spectra of 135-CIGS/112-CIGS with various thicknesses of 135-CIGS capping layer at 10 K.

5.2 PL of 112-CIGS/135-CIGS heterostructure

It can be previously noticed that the 112-CIGS, 135-CIGS and 135-CIGS/112-CIGS show only single broad peak of PL emissions at high excitation power. As a result, the alternate structure of 112-CIGS/135-CIGS is also fabricated for comparison with 135-CIGS/112-CIGS structure. The SEM cross-sectional images of 135-CIGS/112-CIGS with 40 nm thick 135-CIGS was compared to 112-CIGS/135-CIGS with 50 nm and 200 nm thick 112-CIGS as seen in Fig. 49. In Fig. 49(a), the 40 nm 135-CIGS capping layer is barely seen on the 112-CIGS, whereas the 112-CIGS capping layer is noticeable on the surface of the underlying 135-CIGS layer as shown in Fig. 49(b)–(c). The 112-CIGS has relatively larger columnar grains than that the 135-CIGS.

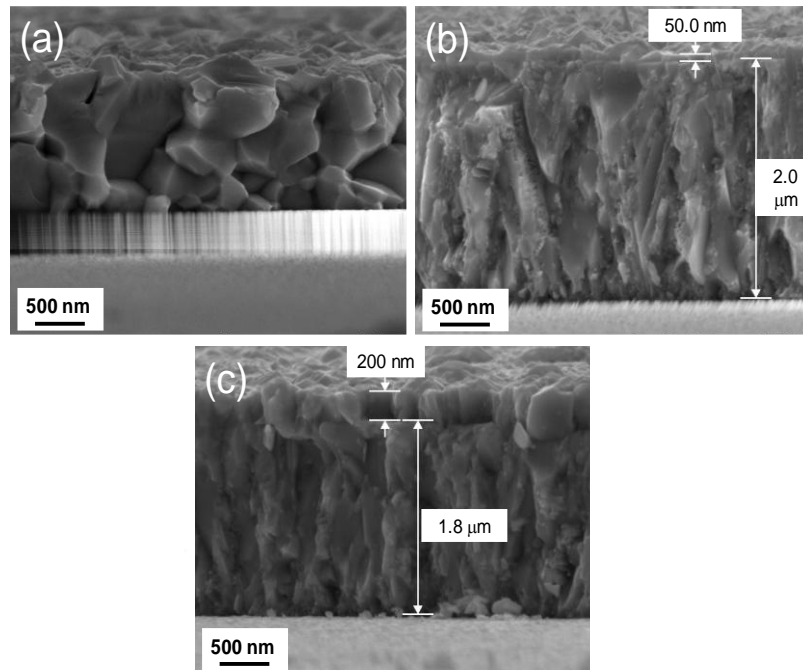


Figure 49: SEM Cross-sectional images of (a) 135-CIGS/112-CIGS with 40 nm thick 135-CIGS and 112-CIGS/135-CIGS with (b) 50 nm and (c) 200 nm thick 112-CIGS.

The PL emission spectra of 112-CIGS/135-CIGS with 50 nm and 200 nm thick 112-CIGS prepared on $\sim 2 \mu\text{m}$ thick 135-CIGS are shown in Fig. 50. Surprisingly, when 112-CIGS is deposited on top of 135-CIGS, the emissions from underlying 135-CIGS and (50, 200 nm thick) 112-CIGS capping layer are resolved and noticeable. The PL emissions from 112-CIGS/135-CIGS, shown in Fig. 50, are significantly distinguishable from those of 135-CIGS/112-CIGS (single-band emission), i.e., they have no temperature and excitation power dependence as those mentioned previously. However, the PL signals are only observed from 10 K up to ~ 200 K. There are five or six distinguishable PL emissions from both 50 and 200 nm thick 112-CIGS capping layers on 135-CIGS. Our previous interpretation, the peak energy positions indicated above 1.12 eV were from the sub-gap states of the underlying 135-CIGS layer since the emitted energies are greater than the E_g of the 112-CIGS capping layer, and thus the peak positions lower 1.12 eV were from the sub-gap states of 112-CIGS upper layer. However, when observing the experimental results more carefully, it was found that the PL peaks are equally separated by 70–90 meV. But, it does not come from the result of phonon replica as shown in other works

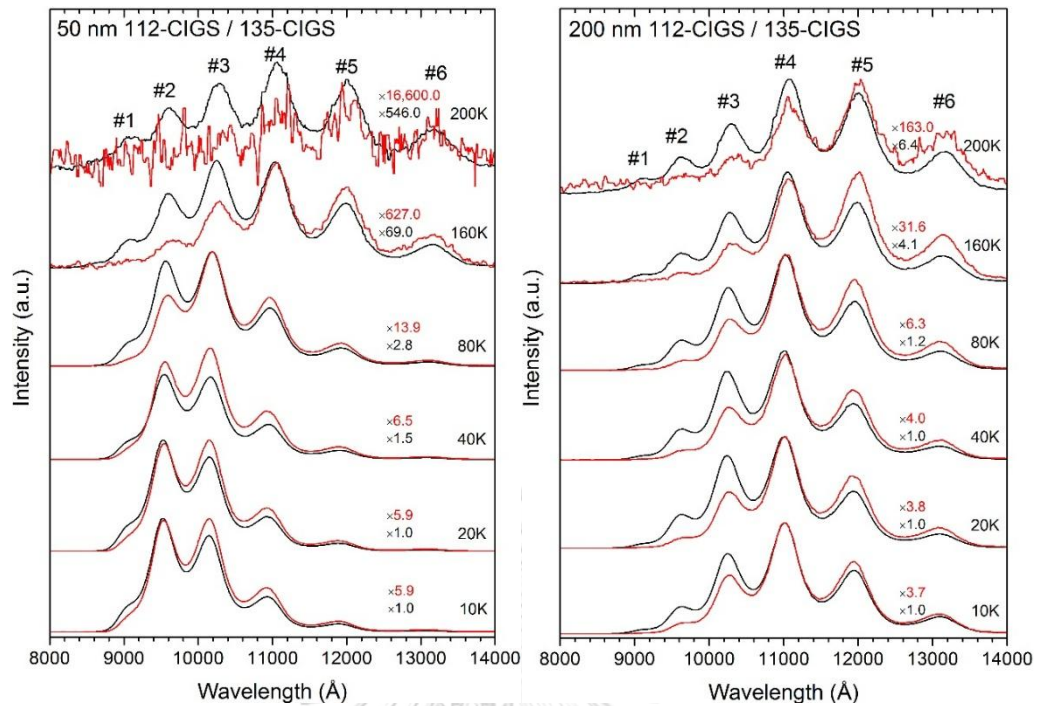


Figure 50: The PL spectra of 112-CIGS/135-CIGS with 50 and 200 nm thick 112-CIGS capping layers at lower (red line) and higher (black line) excitation power from 10–200 K.

[104, 105] because the height of intensities did not descend equally. These PL spectra may cause from the interference effect which is going to be discussed hereafter.

5.2.1 The interference effects in PL of 135-CIGS and CIGS thin films

There are some researchers studied the effect influenced the measured PL spectrum, i.e., thin film interference that originated from, e.g., sample tilt, film roughness, film layer thickness and y values [106]. The thin film interference can strongly affect the PL spectrum of smooth surface that follows from the coherent superposition of the luminescence emitted and internally reflected at the surface of the sample. The artifact PL spectrum may show multiple peaks like it was in 112-CIGS/135-CIGS structure in Fig. 50 that was almost overlooked in this effect. As shown in Fig. 33 of Chapter IV in AFM measurement, 135-CIGS has the surface height and the rms roughness less than 112-CIGS and 135-CIGS/112-CIGS thin films. Consequently, this effect would lead to misinterpretation of PL spectra.

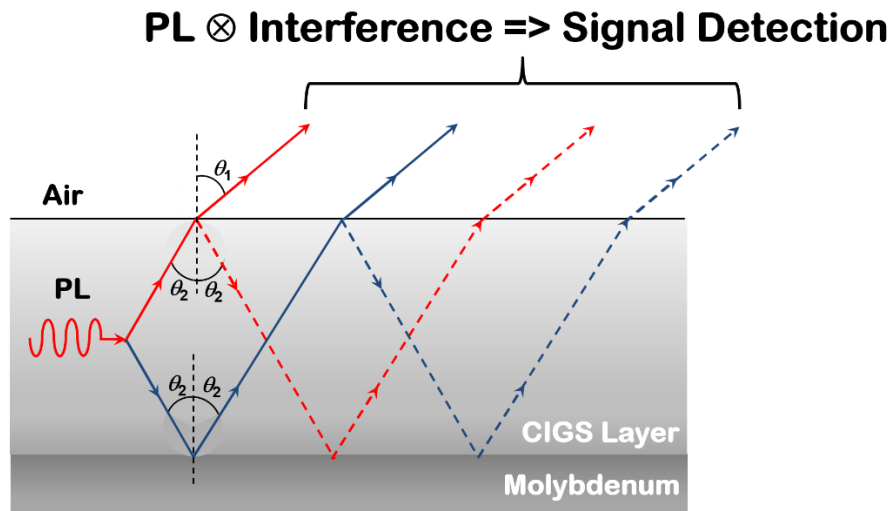


Figure 51: Schematic illustration of PL generated in the CIGS absorber film and collected at angle θ_1 to the surface normal. Red and black lines perform up-going and down-going rays, respectively.

The interference circumstance can directly affect the smooth surface film, here is 135-CIGS layer. In order to make it clear to understand the interference effect, Fig. 51 shows schematic illustration of the interference source. The PL generated in the absorber film can be distinguished between two directions, the first one is up-going beam to be the real PL signal and the another one is down-going beam that incidents to the Mo surface and reflects to the top of film. As the result, the interference effect will occur because of its combination between the real PL and the internal reflection. Then, the PL emission can be approximated by $1-R$, where R is the sample reflectance. Thus, in an attempt to understand the cause for the interference effect, the reflection counterpart with surface roughness, 135-CIGS layer thickness and CIGS film composition ($y \equiv [\text{Cu}]/([\text{Ga}]+[\text{In}])$) are investigated.

5.2.1.1 Effect of surface roughness

The 112-CIGS, 135-CIGS, 135-CIGS/112-CIGS with 40 nm thick of 135-CIGS capping layer and 112-CIGS/135-CIGS with 50 nm thick of 112-CIGS capping layer are investigated for the correlation of surface roughness and PL emission. The surface roughness parameter corresponding with PL emission are shown in Fig. 52 for an absorber layer of 112-CIGS and 135-CIGS with a thickness of 1.8–2.0 μm . The surface roughness of the samples can be determined by root-mean-square (rms)

roughness measured by AFM. The maxima of the fringes are well-matched to the maxima of PL spectrum for 135-CIGS and 112-CIGS/135-CIGS samples. Since the 135-CIGS film has a smoother surface (low rms) than the 112-CIGS, there is the effect of roughness on the PL spectrum for both 135-CIGS and 112-CIGS on top of the 135-CIGS bottom layer. 112-CIGS and 135-CIGS/112-CIGS thin films have rougher surface (high rms) that show no interference effect. Moreover, full width at half maximum (FWHM) of the PL spectrum of 112-CIGS and 135-CIGS/112-CIGS is also smaller than the wavelength of the reflectance fringes. In order to understand of this effect, various FWHM of PL spectrum and reflectance fringes are simulated and illustrated in Fig. 53. The FWHM less than the wavelength shows no interference effect while the FWHMs of those samples that greater than or equal to the wavelength show the dominant interference effect for the measured PL in grey line.

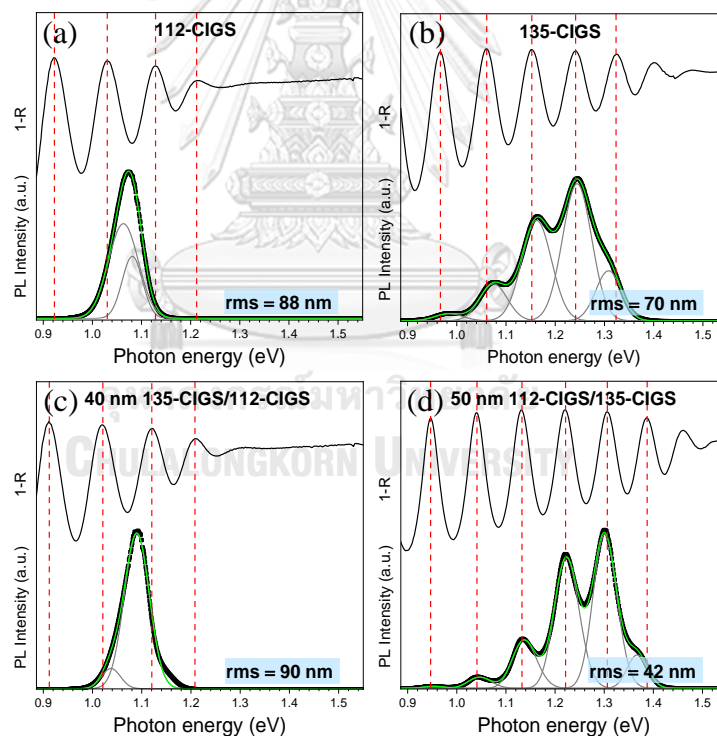


Figure 52: Effect of rms surface roughness on PL emission for (a) 112-CIGS, (b) 135-CIGS, (c) 135-CIGS/112-CIGS and (d) 112-CIGS/135-CIGS thin films.

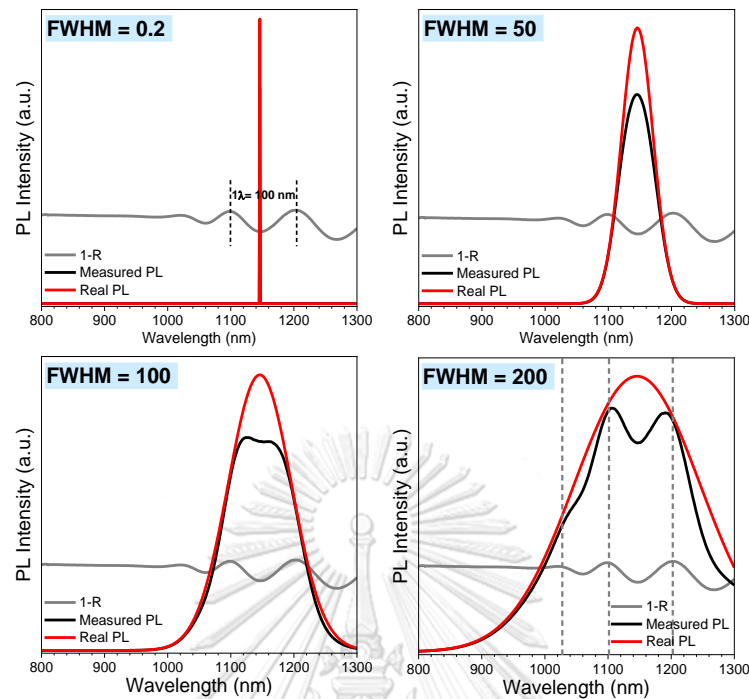


Figure 53: Simulation of Gaussian distribution (measured PL) counterpart with full width at half maximum (FWHM) affected by the interference effect.

5.2.1.2 Effect of 135-CIGS layer thickness

The only 135-CIGS films with various thicknesses are investigated from SEM surface images, rms roughness and reflection to see the interference effect. Fig. 54 shows the summary of SEM surface morphology, rms value and PL spectrum with the measured 1-R. SEM surface images exhibit the smallest grain size for 50 nm thick 135-CIGS. The grain size is gradually increased as the thickness of film increased. It has already been known that grain growth is particularly regarded to factors such as growth temperature, deposition time and composition (x or y). Here in this work, the growth temperature, x and y values at 450°C, 0.37 and 0.33, respectively. The rms roughness increases as the film thickness increases. Although smoother film surface directly affects the reflection, but the thickness of the film has more effect on the interference pattern as shown in the measured 1-R. For samples thinner than 1 μ m, the interference effect is less significant due to the period of the oscillations in the fringes is wider or approaches the width of the PL peak. Then, the interference effect is rarely affected the very thin layer films. For very thick layer, the value of 1-R coincides with the PL peak significantly and the PL peaks are separated almost equally that would be

the result of the interference. The PL spectrum here is assumed by the Gaussian distribution, and when the reflectance is known, the actual PL can be obtained, i.e., by dividing the measured PL with $(1-R)*c$, where c is a factor that scales the fringe amplitude of the measured reflectance to match the fringe amplitude observed in PL. Thus, the actual PL spectrum is shown in red line in the shape of Gaussian distribution. It can be seen that the actual PL peak width (FWHM) is wider than the period of the fringes. This result is opposite to that of the 112-CIGS thin film that the PL peak width of 112-CIGS is smaller than the wavelength and shows no result from the interference.



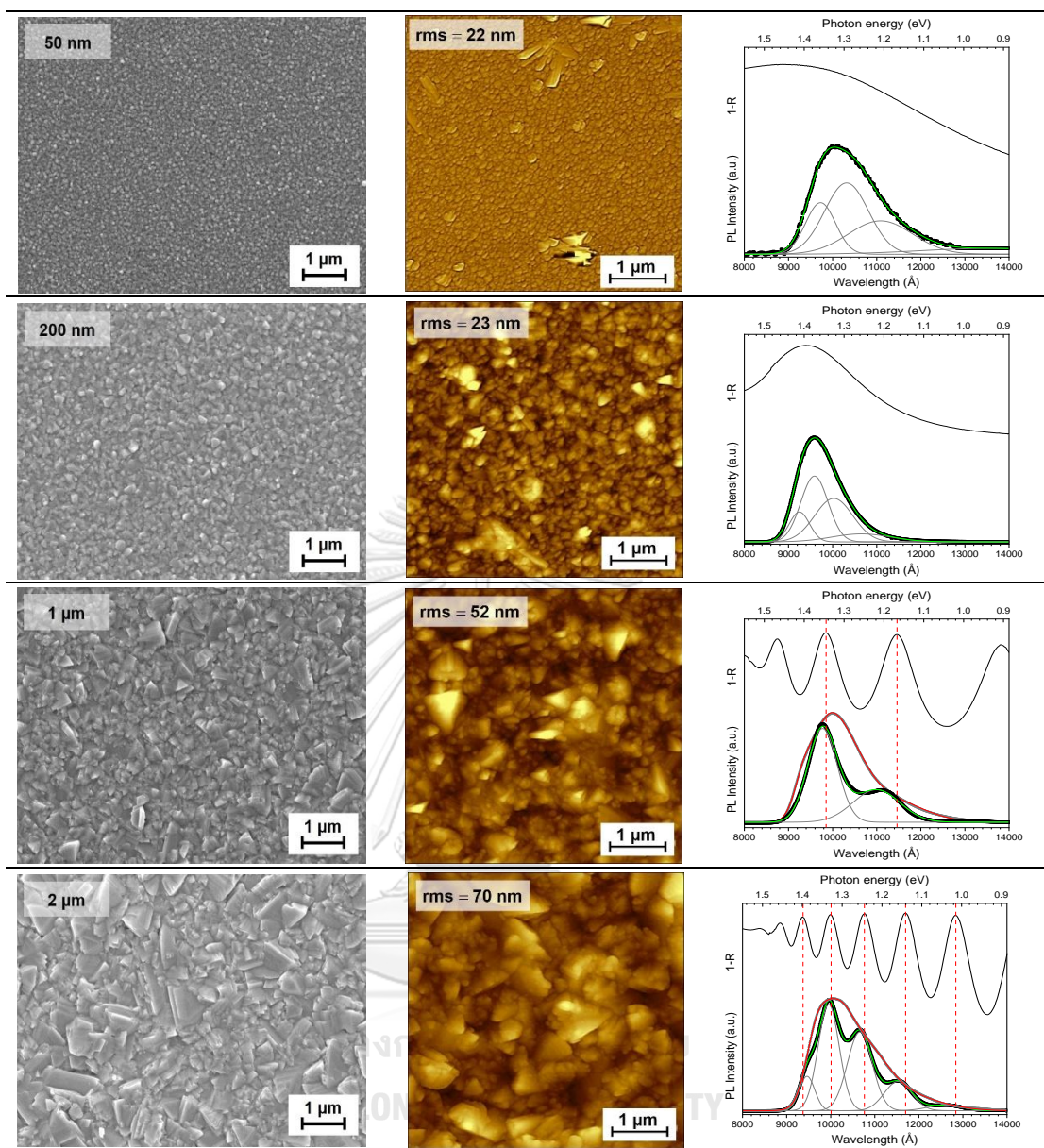


Figure 54: The comparison of SEM surface, AFM, and PL measurement corrected by the interference factor ($1-R$) among the various thicknesses of 135-CIGS layer.

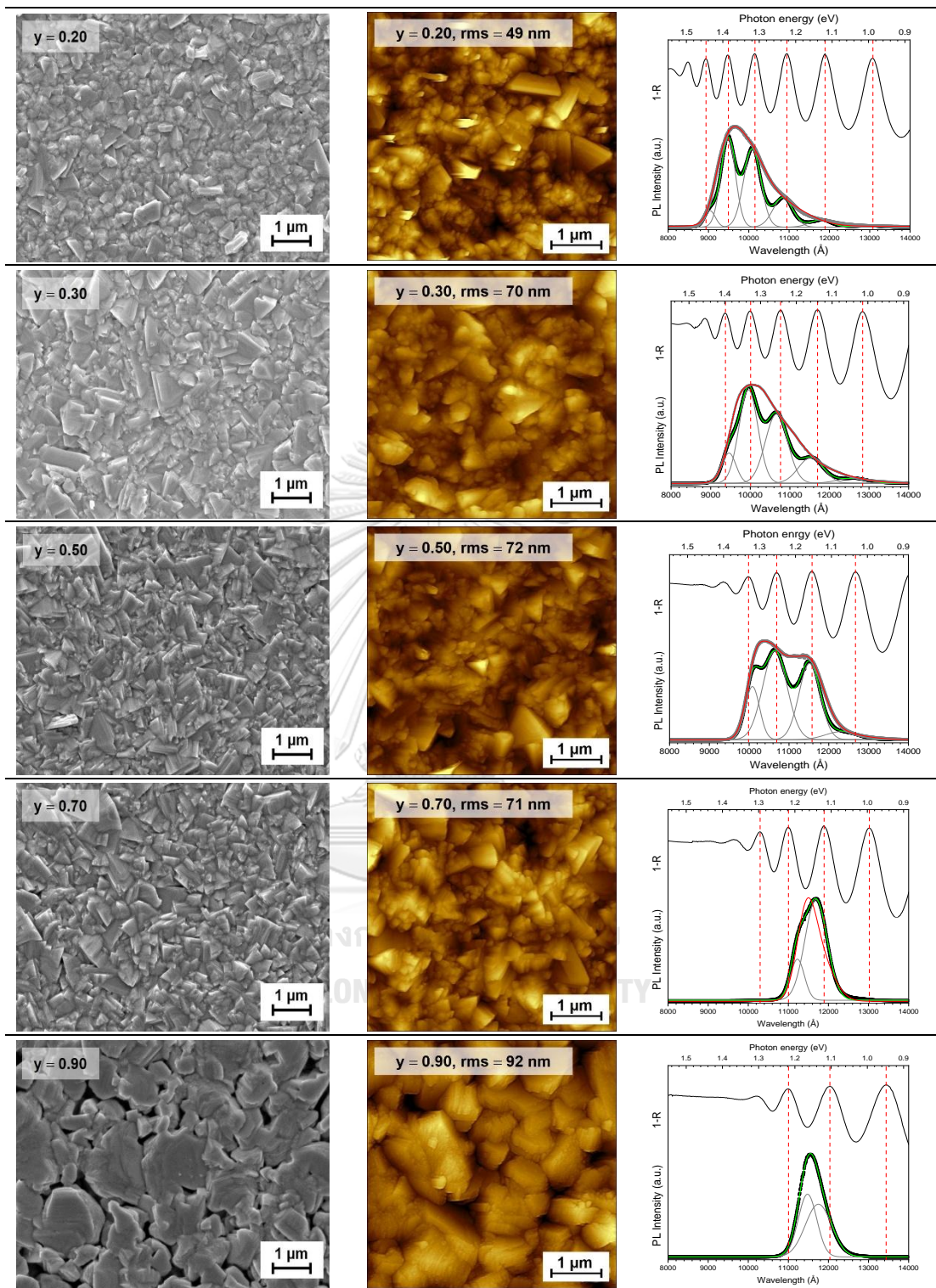


Figure 55: The comparison of SEM surface, AFM, and PL measurement corrected by the interference factor for various compositions of CIGS thin films.

5.2.1.2 Effect of CIGS film composition

Then, in order to substantiate the effect of interference in PL that could be influenced by Cu composition, then the y value is varied from 0.20–0.90 and investigated for surface morphology, rms roughness and PL measurement. As discussed in Chapter IV, the grain size of CIGS thin films depends on both x and y values. Here in this work, x is set at 0.37 and y is varied. The varied y composition of 0.20, 0.33, 0.50, 0.70 and 0.90 can be established to be 158-CIGS, 135-CIGS, 247-CIGS, 235-CIGS and 112-CIGS, respectively [107-109]. The y values of 0.20–0.70 are commonly existed as β -phase or ordered defect compound (ODC) as illustrated in Fig. 7. As y is decreased from 0.90 to 0.20, the grain size becomes smaller as shown in SEM surface images of Fig. 55. In addition, the rms roughness is also reduced. The thickness of these thin films is about 2 μm . The result of interference has a strong effect on y value, especially when y is lower than 0.50 as depicted in the appearance of fringes in the PL spectrum. In comparison of measured PL and $1-R$, the coincidence between the maxima of $1-R$ and the measured PL is obvious for y less than 0.50. The PL correction of 135-CIGS with lower y value shows the similar broadening shape. The influence of y composition that affect the interference almost vanishes when it approaches to 0.90 (112-CIGS).

5.2.2 The PL correction for 112-CIGS/135-CIGS heterostructures

As it has been shown that what factors can result in the interference in the PL spectrum, e.g., the surface roughness, the layer thickness and composition of 135-CIGS. To understand how the thickness of 112-CIGS capping layer affect for 135-CIGS underlying layer, the thicknesses of 112-CIGS are varied for 5, 10, 25, 50, 80, 140, 200 and 300 nm on top of the 135-CIGS layer for the PL measurements. Fig. 56 shows the temperature-dependent PL spectra of the films of 112-CIGS/135-CIGS with 10 nm thick of 112-CIGS from 10–200K. Inset is the Gaussian distribution fitting of PL spectrum at 10 K.

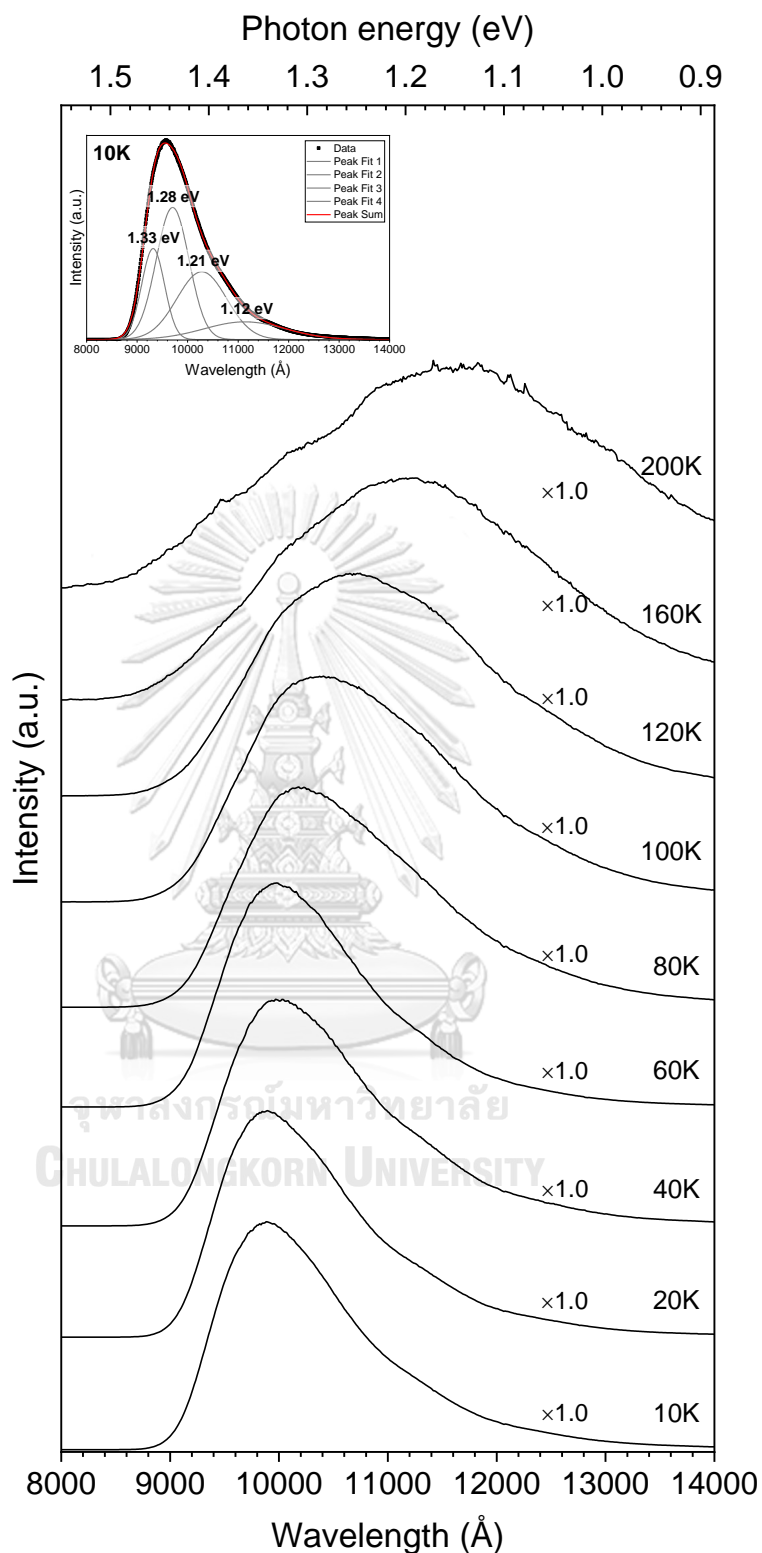


Figure 56: The PL spectra of the 112-CIGS/135-CIGS thin film with 10 nm thick of 112-CIGS capping layer under temperatures from 10 K to 200 K. Inset is the fitting result of PL spectrum at 10 K using Gaussian distribution.

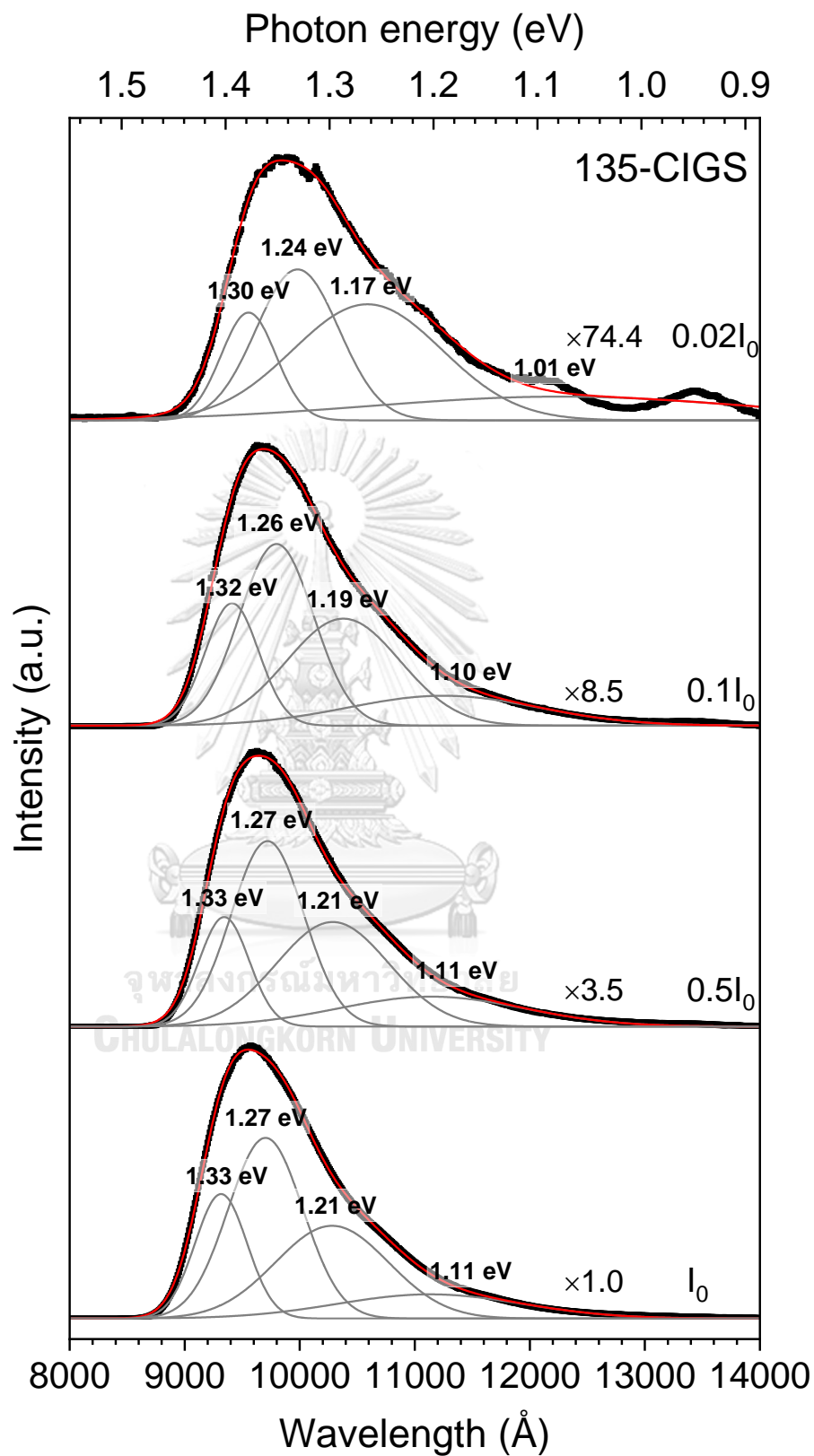


Figure 57: The PL spectra of the 112-CIGS/135-CIGS thin film with 10 nm thick of 112-CIGS capping layer under various excitation power.

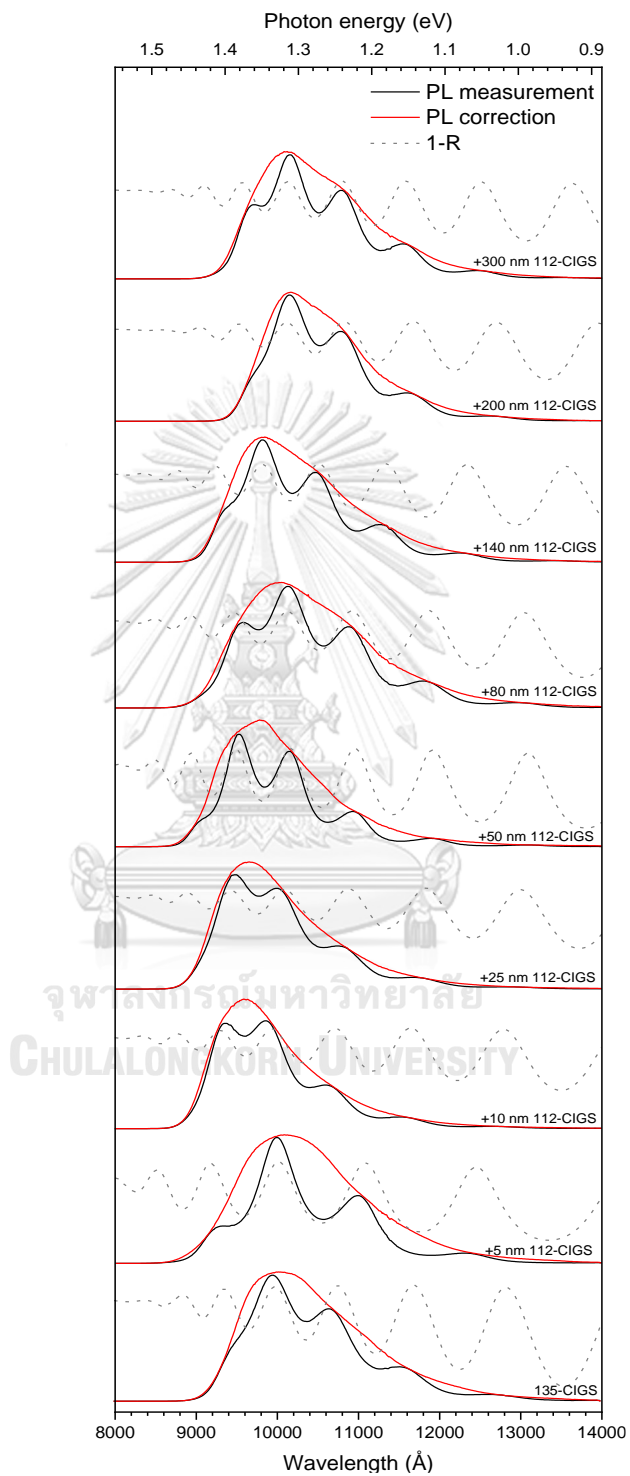


Figure 58: The PL spectra, PL correction and 1-R of the 112-CIGS/135-CIGS thin film with various thicknesses of 112-CIGS capping layer.

The 112-CIGS/135-CIGS heterostructures show more broadening line width than that of the 135-CIGS/112-CIGS heterostructures. The broad peaks are observed in range 0.95–1.40 eV. The PL spectra from 112-CIGS/135-CIGS show red shift as the temperature increases similar to that of only 135-CIGS film, which is the nature of n-type semiconductor. Moreover, the excitation power-dependent PL spectrum of 112-CIGS/135-CIGS shifts toward lower energy as the power decreases as shown in Fig. 57. From the temperature-dependent and excitation power-dependent results, the band diagram of 112-CIGS/135-CIGS can be depicted in Fig. 47(c) that consists only DAP transitions. The donor and acceptor defects are the same types like in 135-CIGS thin film.

In order to compare the PL emissions among the various thicknesses of 112-CIGS layer, the PL spectra depending on 112-CIGS capping layer are compared in Fig. 58 at 10K. The dominant PL peak of only 135-CIGS is ~1.23 eV. A very thin 5 nm thick 112-CIGS has less effect on the 135-CIGS, i.e., no change the PL peak. However, the PL peaks of thin 112-CIGS capping layer of 10–50 nm are slightly shifted to 1.28 eV higher than that of the only 135-CIGS by 50 meV. It may arise from the compressive strain between the layer that is dissimilar from the tensile strain in 135-CIGS/112-CIGS heterostructure. For 80 nm thick 112-CIGS, the PL peak is back to the original position and then shifts toward lower energy for a thicker layer of 112-CIGS capping layer of 200 nm. It can be described that a greater amount of 112-CIGS layer can cause the PL peak of 112-CIGS/135-CIGS shifting to the peak direction of 112-CIGS.

5.3 Summary Remarks

In this study, the broad PL emissions from both 112-CIGS thin films and 135-CIGS/112-CIGS heterostructures are identified as the DAPs and FB transitions with corresponding temperature and excitation power dependence. The PL spectra of 112-CIGS/135-CIGS heterostructures exhibit no temperature and excitation power dependence and resolve to various transitions contributed from the interference effect. The sub-gap states from 135-CIGS and 112-CIGS/135-CIGS heterostructures are indicated as the DAPs transition due to the defect compound of 135-CIGS. The dominated DAPs transition is slightly shifted to higher photon energy for a very thin

of 135-CIGS or 112-CIGS capping layer. The nature of the PL emissions from the sub-gap states observed in the 135-CIGS/112-CIGS and 112-CIGS/135-CIGS heterostructures are distinguishable depending upon the sequence of the deposited layers.



CHAPTER VI

CONCLUSION

High efficiency 112-CIGS thin film solar cells usually require additional techniques to enhance the solar cell parameters. One of the techniques that is motivated by pseudo-homojunction of the absorber is the inserting of a wider band gap of a thin 135-CIGS defect phase layer between n-type CdS and p-type 112-CIGS. Thus, understanding of the effects of 135-CIGS capping layer on 112-CIGS film is necessary to develop CIGS devices with high efficiency.

The effects of thickness of 135-CIGS capping layer on 112-CIGS film (135-CIGS/112-CIGS) were investigated in this work through bare absorbers and solar cell devices. The absorbers of 135-CIGS/112-CIGS were observed for their optical band gap energy via the transmittance and reflectance measurements, crystal structure by X-ray diffraction, morphology by the atomic force microscopy (AFM) and scanning electron microscopy (SEM), defect states by photoluminescence (PL) technique for both 135-CIGS/112-CIGS and 112-CIGS/135-CIGS heterostructures, solar cell performance by I-V and quantum efficiency (QE) measurements, respectively. Moreover, the film composition of 112-CIGS, 135-CIGS/112-CIGS and 135-CIGS was assured by the energy dispersive X-ray spectroscopy (EDS) technique.

Important conclusions for the macroscopic observation are, (1) 135-CIGS thin film has larger band gap energy (E_g) compared to 112-CIGS, (2) when 135-CIGS is on 112-CIGS structure, the E_g increased more than the stand-alone 112-CIGS as the thickness of 135-CIGS capping layer increased due to the decreasing of volume of unit cell. The increasing of band gap energy can be affected by two mechanisms, (i) the strain induced by a thinner 10–80 nm of 135-CIGS upper layer to the whole 112-CIGS structure, (ii) the overall composition of CIGS thin film changes to lower Cu-atomic ratio ($y = [\text{Cu}]/([\text{Ga}]+[\text{In}])$) because of the elemental diffusion from 112-CIGS diffusing to a thick 135-CIGS capping layer of 200–300 nm. For the device applications, the parameter of open circuit voltage (V_{oc}) is increased with the thickness of 135-CIGS capping layer because of the increasing of E_g , except when the 135-CIGS layer is too thick (> 200 nm). The current densities (J_{sc}) are comparable to

112-CIGS devices, except for 200 nm thick of 135-CIGS layer shows slightly lower values. Hence, it is likely that a very thin 135-CIGS layer is a benefit for CIGS solar cells. The defect phase of 135-CIGS by a post-deposition may lead to the valence band offset (ΔE_v) at the surface because of its larger E_g than 112-CIGS approximately 0.30 eV. The valence band bending at the interface of n-CdS and p-CIGS layer can retard the recombination rate by blocking holes from the interface with high energy barrier. As a result, the open circuit voltage (V_{oc}) distinctly increases. One important problem that can be misled by the effect of 135-CIGS is the elemental diffusion from 112-CIGS layer diffusing to a very thick of 135-CIGS covered layer to form another CIGS composition as a whole. The results obtained in this dissertation yield a suggestion that can improve the V_{oc} of devices and to substantiate the existing of 135-CIGS layer by indirect means. Those techniques are such as secondary ion mass spectrometry (SIMs) or grazing incident X-ray diffraction (GIXRD) may be useful to verify the existence of 135-CIGS covered layer directly but they are very time consuming.

Apart from the macroscopic observation of the device performance, the microscopic investigation for 135-CIGS/112-CIGS or even 112-CIGS/135-CIGS heterostructure is also essential. The defect energy level can be achieved by the photoluminescence (PL) measurement in order to investigate the effect of 135-CIGS capping layer. The PL transitions were observed for both the temperature-dependent and excitation power-dependent. The general defect states detected in 112-CIGS thin film are Cu vacancies (V_{Cu}) and Se vacancies (V_{Se}) that are the acceptor defects and donor defects, respectively. The deep donor defects, i.e., group-III elements on the Cu site (III_{Cu}) is found only in 135-CIGS and 112-CIGS/135-CIGS structures. The transitions found in this work are donor to acceptor (DAP) transition and free-electron to bound-acceptor (FB) transition. The 112-CIGS and 135-CIGS show the nature of p-type and n-type, respectively. The first one exhibits blue-shift while the latter one shows red-shift as the temperature increases. The PL of 135-CIGS/112-CIGS samples with a very thin of 135-CIGS capping layer of 1–40 nm shift to higher energy as compared to only 112-CIGS film which is the same as the PL of 112-CIGS/135-CIGS samples with a very thin of 112-CIGS capping layer. These suggest that the widen E_g

at the interface that can induce a shift in the energy levels of either conduction band or valence band to higher energy level. Another interesting results for this experiment is the interference effect from a smoother surface of 135-CIGS that can conceal the real PL and show the artifact PL instead, especially the structure of 112-CIGS/135-CIGS. This has a direct effect on a very broad PL spectrum in which the full width at half maximum (FWHM) is larger than a wavelength of interference fringes. As a result, in order to prevent the misleading, the PL spectra need to be corrected.

In this work, the capping layer was always kept thinner than the bottom layer. Thus, the properties under investigation were mainly influenced by the bottom layer. Therefore, further experiments with the variations of 135-CIGS and 112-CIGS thickness may reveal the preeminent phenomena, such as blue-shift or red-shift, depending on the layer thickness. For example, in the PL measurements, it remains unclear whether n-type or p-type the films would exhibit in the 135-CIGS/112-CIGS and 112-CIGS/135-CIGS bilayer structures when the thickness of capping layer and bottom layer is comparable. This leaves some questions for future investigation.

REFERENCES

1. Ossila Ltd., *Perovskites and Perovskite Solar Cells: An Introduction*. Available at: <https://www.ossila.com/pages/perovskites-and-perovskite-solar-cells-an-introduction>. (Accessed: 17th May 2019).
2. Yoshida, S., *Solar Frontier Achieves World Record Thin-Film Solar Cell Efficiency of 22.9%*. 2017: Solar Frontier, Tokyo, Japan.
3. P. Jackson, et al., *Effects of heavy alkali elements in Cu(In,Ga)Se₂ solar cells with efficiencies up to 22.6%*. Phys. Status Solidi RRL, 2016. **10**(8): p. 583-586.
4. A. Chirila, et al., *Potassium-induced surface modification of Cu(In,Ga)Se₂ thin films for high-efficiency solar cells*. Nature Materials, 2013. **12**: p. 1107-1111.
5. Sakdanuphab, R., *Influence of Sodium in Fabrication Process of High Efficiency Cu(In,Ga)Se₂ Thin Film Solar Cells*. 2010, Chulalongkorn University: Department of Physics Faculty of Science p. 103.
6. Gloeckler, M. and J.R. Sites, *Band-gap grading in Cu(In,Ga)Se₂ solar cells*. J. Phys. Chem. Solids, 2005. **66**(11): p. 1891-1894.
7. T. Dullweber, et al., *A new approach to high-efficiency solar cells by band gap grading in Cu(In,Ga)Se₂ chalcopyrite semiconductors*. Sol. Energy Mater. Sol. Cells, 2001. **67**: p. 145-150.
8. Kodigala, S.R., *Thin Films and Nanostructures Cu(In_{1-x}Ga_x)Se₂ Based Thin Film Solar Cells*. 2010: United States of America: Academic Press of Elsevier.
9. C. L. Jenson, et al., *The role of gallium in CuInSe₂ solar cells fabricated by a two-stage method*, in *23rd IEEE Photovoltaic Specialist Conference*. 1993: Louisville. p. 577-580.
10. W. N. Shafarman, R.K., B. E. McCandless, *Device and material characterization of Cu(InGa)Se₂ solar cells with increasing band gap*. J. Appl. Phys., 1996. **79**(9): p. 7324-7328.
11. A. Luque and S. Hegedus, *Handbook of photovoltaic science and engineering*. 2003, England: John Wiley & Sons Ltd. 1,179.
12. J. Hedstrijm, et al., *ZnO/CdS/Cu(In,Ga)Se₂ thin film solar cells with improved performance*, in *IEEE Photovoltaic Specialist Conference*. 1993.
13. A. M. Gabor, et al., *High efficiency CuIn_xGa_{1-x}Se₂ solar cells made from*

- (In_xGa_{1-x})₂Se₃ precursor films. Appl. Phys. Lett. , 1994. **65**(2): p. 198-200.
14. T. Nakada, et al., *Improved Cu(In,Ga)(S,Se)₂ thin film solar cells by surface sulfurization*. Sol. Energy Mater. Sol. Cells, 1997. **49**: p. 285-290.
 15. U. P. Singh, W. N. Shafarman, and R.W. Birkmire, *Surface sulfurization studies of Cu(InGa)Se₂ thin film*. Sol. Energy Mater. Sol. Cells, 2006. **90**: p. 623-630.
 16. F. Kessler and D. Rudmann, *Technological aspects of flexible CIGS solar cells and modules*. Sol. Energy, 2004. **77**: p. 685-695.
 17. T. Nakada, et al., *Effects of Sodium on Cu(In, Ga)Se₂-Based Thin Films and Solar Cells*. Jpn. J. Appl. Phys., 1997. **36**: p. 732-737.
 18. S. H. Wei, S. B. Zhang, and A. Zunger, *Effects of Na on the electrical and structural properties of CuInSe₂*. J. Appl. Phys., 1990. **85**(10): p. 7214-7218.
 19. B. Namnuan, K. Yoodee, and S. Chatrathorn, *Probing diffusion of In and Ga in CuInSe₂/CuGaSe₂ bilayer thin films by x-ray diffraction*. J. Cryst. Growth, 2015. **432**: p. 24-32.
 20. D. Schmid, et al., *Chalcopyrite/defect chalcopyrite heterojunctions on the basis of CuInSe₂*. J. Appl. Phys., 1993. **73**(6): p. 2902-2909.
 21. N. E. Gorji, et al., *A new approach to valence and conduction band grading in CIGS thin film solar cells*. IACSIT International J. Eng. Techol., 2012. **4**(5): p. 573-576.
 22. T. Negami, et al., *Preparation and characterization of Cu(In_{1-x}Ga_x)₃Se₅ thin films*. J. Appl. Phys., 1995. **67**(6): p. 825-827.
 23. H. Z. Xiao, L.-Chung Yang, and A. Rockett, *Structural, optical, and electrical properties of epitaxial chalcopyrite CuIn₃Se₅ films*. J. Appl. Phys., 1994. **76**(3): p. 1503-1510.
 24. C. D. Kim, M. S. Jin, and W.T. Kim, *Growth and Characterization of Ordered Vacancy Chalcopyrite CuIn₃Se₅ and Cu(In, Ga)₃Se₅ Single Crystals*. J. Korean Phys. Soc., 1998. **30**(3): p. 750-753.
 25. R. Kimura, et al., *Photoluminescence properties of sodium incorporation in CuInSe₂ and CuIn₃Se₅ thin films* Sol. Energy Mater. Sol. Cells, 2001. **67**: p. 289-295.
 26. D. Habib, et al., *Fabrication, Characterization and Optical Properties of*

- CuIn₃Se₅ Bulk Compounds*. World Journal of Condensed Matter Physics (WJCMP), 2015. **5**: p. 201-208.
27. M. J. Romero, et al., *Surface-layer band gap widening in Cu(In,Ga)Se₂ thin films*. J. Appl. Phys., 2003. **83**(23): p. 4731-4733.
 28. A. Stokes, et al., *Direct evidence of a Cu(In,Ga)₃Se₅ phase in a bulk, high-Efficiency Cu(In,Ga)Se₂ device using atom probe tomography*, in *IEEE Photovoltaic Specialist Conference*. 2014. p. 3335-3337.
 29. M. Morkel, et al., *Flat conduction-band alignment at the CdS/CuInSe₂ thin-film solar-cell heterojunction*. J. Appl. Phys., 2001. **79**(27): p. 4482-4485.
 30. Y. Yan, et al., *Microstructure of surface layers in Cu(In,Ga)Se₂ thin films*. J. Appl. Phys., 2002. **81**(6): p. 1008-1010.
 31. I. M. Kötschau and H.W. Schock, *Depth profile of the lattice constant of the Cu-poor surface layer in (Cu₂Se)_{1-x}(In₂Se₃)_x evidenced by grazing incidence X-ray diffraction*. J. Phys. Chem. Solids, 2003. **64**: p. 1559-1563.
 32. M.M. Islam, et al., *Determination of Cu(In_{1-x}Ga_x)₃Se₅ defect phase in MBE grown Cu(In_{1-x}Ga_x)Se₂ thin film by Rietveld analysis*. Sol. Energy Mater. Sol. Cells, 2011. **95**: p. 231-234.
 33. M. M. Islam, et al., *Impact of Se flux on the defect formation in polycrystalline Cu(In,Ga)Se₂ thin films grown by three stage evaporation process*. J. Appl. Phys., 2013. **113**: p. 064907.
 34. S. H. Kwon, D. Y. Lee, and B.T. Ahn, *Characterization of Cu(In_{1-x}Ga_x)Se₂ films prepared by three-stage coevaporation and their application to CIGS solar cells for a 14.48 % Efficiency*. J. Korean Phys. Soc., 2001. **39**(4): p. 655-660.
 35. T. Nishimura, et al., *Control of valence band offset at CdS/Cu(In,Ga)Se₂ interface by inserting wide-bandgap materials for suppression of interfacial recombination in Cu(In,Ga)Se₂ solar cells*. Jpn. J. Appl. Phys., 2015. **54**: p. 08KC08.
 36. K. Yoshino, et al., *Crystal growth and photoluminescence of CuIn_xGa_{1-x}Se₂ alloys*. J. Cryst. Growth, 2000. **211**: p. 476-479.
 37. B. J. Stanbery, *Copper indium selenides and related materials for photovoltaic devices*. Crit. Rev. Solid State Mater. Sci., 2002. **27**: p. 73-117.

38. J. H. Schön and E. Bucher, *Comparison of point defects in CuInSe₂ and CuGaSe₂ single crystals*. Sol. Energy Mater. Sol. Cells, 1999. **57**: p. 229-237.
39. C. Rincón, et al., *Optical properties and characterization of CuInSe₂*. Sol. Cells, 1986. **16**: p. 335-349.
40. G. P. Bernardioni and A. Catani, *The Cu-Se system*. Mineral Deposita (Berl.), 1968. **3**: p. 375-380.
41. R. Noufi, et al., *Investigation of the microstructure of Cu(In,Ga)Se₂ thin films used in high-efficiency devices*, in *29th IEEE Photovoltaic Specialists Conference*. 2002.
42. J. E. Jaffe and A. Zunger, *Theory of the band-gap anomaly in ABC₂ chalcopyrite semiconductors*. Phys. Rev. B, 1984. **29**: p. 1882-1906.
43. B. D. Viezbicke, et al., *Evaluation of the Tauc method for optical absorption edge determination: ZnO thin films as a model system* Phys. Status Solidi B, 2015. **252**: p. 1700-1710.
44. Pankove, J.I., *Optical processes in semiconductors*. 1971, New York, United States: Dover Publication, Inc. 422.
45. Tauc, J., *Optical properties and electronic structure of amorphous Ge and Si*. Mat. Res. Bull., 1968. **3**: p. 37-46.
46. K. Osamura, S. Naka, and Y. Murakami, *Preparation and optical properties of Ga_{1-x}In_xN thin film*. J. Appl. Phys., 1975. **46**: p. 3432-3437.
47. G. H. Bauer, et al., *Quasi-Fermi level splitting and identification of recombination losses from room temperature luminescence in Cu(In_{1-x}Ga_x)Se₂ thin films versus optical band gap*. Thin Solid Films, 2005. **480-481**: p. 410-414.
48. Lutz Nasdala, et al., *Spectroscopic methods in mineralogy*. Luminescence techniques in earth science. Vol. 6. 2004: EÖTVÖS university press.
49. Neamen, D.A., *Semiconductor physics and devices*. 4th ed. 2012, Singapore: The McGraw-Hill Companies, Inc. 758.
50. Bube, R.H., *Photovoltaic material*. 1998, London: Imperial college press.
51. Z. J. Wei, et al., *Morphology of CIGS thin films deposited by single-stage process and three-stage process at low temperature*. Optoelectron. Lett., 2013. **9(6)**: p. 0449-0453.

52. M. Nishitani, T. Negami, and T. Wada, *Composition monitoring method in CuInSe₂ thin film preparation*. Thin Solid Films, 1995. **258**: p. 313-316.
53. J. Kessler, et al., *Cu(In,Ga)Se₂ thin films grown with a Cu-Poor/Rich/Poor sequence: growth model and structural considerations*. Prog. Photovolt: Res. Appl., 2003. **11**: p. 319-331.
54. J. Schöldström, J. Kessler, and M. Edoff, *Two-stage growth of smooth Cu(In,Ga)Se₂ films using end-point detection*. Thin Solid Films, 2005. **480-481**: p. 61-66.
55. R. Scheer, et al., *Cu(In_{1-x}Ga_x)Se₂ growth studies by in situ spectroscopic light scattering*. Appl. Phys. Lett., 2003. **82**: p. 2091-2093.
56. J. Liu, et al., *Preparation of Cu(In,Ga)Se₂ thin film by sputtering from Cu(In,Ga)Se₂ quaternary target*. Prog. Nat. Sci. Mater. Int., 2013. **23**(2): p. 133-138.
57. X. L. Zhu, et al., *13.6%-efficient Cu(In,Ga)Se₂ solar cell with absorber fabricated by RF sputtering of (In,Ga)₂Se₃ and CuSe targets*. Sol. Energy Mater. Sol. Cells, 2013. **113**: p. 140-143.
58. M. Wolf, *Limitations and possibilities for improvement of photovoltaic solar energy converters; Part I: Considerations for earth's surface operation*. Proc. IRE, 1960: p. 1246-1263.
59. T. Dullweber, et al., *Study of the effect of gallium grading in Cu(In,Ga)Se₂*. Thin Solid Films, 2000. **361-362**: p. 478-481.
60. O. Lundberg, M. Edoff, and L. Stolt, *The effect of Ga-grading in CIGS thin film solar cells*. Thin Solid Films, 2005. **480-481**: p. 520-525.
61. R. Sakdanuphab, S. Chatraphorn, and K. Yoodee, *The advantages of Ga-graded obtained by growth profile modification and Na incorporation on Cu(In,Ga)Se₂ solar cells*. Adv. Mater. Res., 2014. **936**: p. 633-638.
62. O. Lundberg, et al., *Diffusion of indium and gallium in Cu(In,Ga)Se₂ thin film solar cells*. J. Phys. Chem. Solids, 2003. **64**: p. 1499-1504.
63. R. Sakdanuphab, et al., *Growth characteristics of Cu(In,Ga)Se₂ thin films using 3-stage deposition process with a NaF precursor*. J. Cryst. Growth, 2011. **319**: p. 44-48.

64. W. Thongkham, et al., *Enhancing efficiency of Cu(In,Ga)Se₂ solar cells on flexible stainless steel foils using NaF co-evaporation*. Sol. Energy, 2013. **92**: p. 189-195.
65. K. Granath, M. Bodegård, and L. Stolt, *The effect of NaF on Cu(In, Ga)Se₂ thin film solar cells*. Sol. Energy Mater. Sol. Cells, 2000. **60**: p. 279-293.
66. Roth, A., *Vacuum technology*. 1990, Amsterdam, The Netherlands: Elsevier science publishers B. V. 554.
67. C. Chityuttakan, et al., *In situ monitoring of the growth of Cu(In,Ga)Se₂ thin films*. Sol. Energy Mater. Sol. Cells, 2006. **90**: p. 3124-3129.
68. R. Hunger, et al., *In situ deposition rate monitoring during the three-stage-growth process of Cu(In,Ga)Se₂ absorber films*. Thin Solid Films, 2003. **431-432**: p. 16-21.
69. S. Nishiwaki, et al., *Preparation of Cu(In,Ga)Se₂ thin films from Cu-Se/In-Ga-Se precursors for high-efficiency solar cells*. Sol. Energy Mater. Sol. Cells, 2001. **67**: p. 217-223.
70. Ortega-Borges, R. and D. Lincot, *Mechanism of chemical bath deposition of cadmium sulfide thin films in the ammonia-thiourea system*. J. Electrochem. Soc., 1993. **140**: p. 3464-3473.
71. Y. Hirai, Y.H., Y. Kurokawa, A. Yamada, *Improvement of the band profile of Cu(In,Ga)Se₂ solar cells with high-Ga content prepared using a five-stage method*. Jpn. J. Appl. Phys., 2012. **51**: p. 10NC03.
72. W. Shockley and H.J. Queisser, *Detailed balance limit of efficiency of pn junction solar cells*. J. Appl. Phys., 1961. **32**: p. 510-519.
73. Siebentritt, S., *What limits the efficiency of chalcopyrite solar cells?* Sol. Energy Mater. Sol. Cells, 2011. **95**: p. 1471-1476.
74. S. Jung, et al., *Effects of Ga contents on properties of CIGS thin films and solar cells fabricated by co-evaporation technique*. Curr. Applied Physics, 2010. **10**: p. 990-996.
75. J. T. Heath, et al., *Effect of Ga content on defect states in CuIn_{1-x}Ga_xSe₂ photovoltaic devices*. Appl. Phys. Lett., 2002. **80**: p. 4540-4542.
76. G. Hanna, et al., *Influence of the Ga-content on the bulk defect densities of*

- Cu(In,Ga)Se₂*. Thin Solid Films, 2001. **387**: p. 71-73.
77. S. H. Wei, S. B. Zhang, and A. Zunger, *Effects of Ga addition to CuInSe₂ on its electronic, structural, and defect properties*. Appl. Phys. Lett., 1998. **72**: p. 3199-3201.
 78. X. Lyu, et al., *Influences of sulfurization on performances of Cu(In,Ga)(Se,S)₂ cells fabricated based on the method of sputtering CIGSe quaternary target*. J. Alloy Comp., 2019. **791**: p. 1193-1199.
 79. Y. Kamikawa, et al., *Effect of thermal annealing on the redistribution of alkali metals in Cu(In,Ga)Se₂ solar cells on glass substrate*. J. Appl. Phys., 2018. **123**: p. 093101.
 80. A. Sadono, et al., *Effect of an additional Cu-deficient layer deposition on alkali treated Cu(In,Ga)Se₂ solar cells deposited at low temperature*. Sol. Energ. Mat. Sol. Cells, 2018. **184**: p. 67-72.
 81. S. Zahedi-Azad, et al., *Influence of heavy alkali post deposition treatment on wide gap Cu(In,Ga)Se₂*. Thin Solid Films, 2019. **669**: p. 629-632.
 82. T. Feurera, et al., *RbF post deposition treatment for narrow bandgap Cu(In,Ga)Se₂ solar cells*. Thin Solid Films, 2019. **670**: p. 34-40.
 83. M. Raghuwanshi, et al., *Influence of RbF post deposition treatment on heterojunction and grain boundaries in high efficient (21.1%) Cu(In,Ga)Se₂ solar cells*. Nano Energy, 2019. **60**: p. 103-110.
 84. J. Chen, et al., *Engineered Cu(InGa)Se₂ thin films through CaF₂ post-deposition treatment for enhancing solar cell performance*. J. Alloy Comp., 2018. **766**: p. 1046-1053.
 85. D. Schmid, M. Ruckh, and H. W. Schock, *A comprehensive characterization of the interfaces in Mo/CIS/CdS/ZnO solar cell structures*. Sol. Energy Mater. Sol. Cells, 1996. **41/42**: p. 281-294.
 86. T. Nishimura, et al., *Fabrication of Cu(In,Ga)Se₂ solar cells with a single graded band profile*. Phys. Solidi B, 2015. **252**: p. 1235-1238.
 87. J. H. Kim, et al., *Fabrication of wide-bandgap β -Cu(In,Ga)₃Se₅ thin films and their application to solar cells*. Current Photovoltaic Research, 2013. **1**(1): p. 38-43.

88. Y. Hirai, Y. Kurokawa, and A. Yamada, *Numerical study of Cu(In,Ga)Se₂ solar cell performance toward 23% conversion efficiency* Jpn. J. Appl. Phys., 2014. **53**: p. 012301.
89. B. Namnaun, K. Yoodee, and S. Chatraphorn, *Different natures of sub-gap states in 135-CIGS/112-CIGS and 112-CIGS/135-CIGS heterostructures investigated by photoluminescence technique*. J. Phys. Conf. Ser., 2018. **1144**: p. 012058.
90. E. Haubold, et al., *Short-range versus long-range structure in Cu(In,Ga)Se₂, Cu(In,Ga)₃Se₅, and Cu(In,Ga)₅Se₈*. J. Alloy Comp., 2019. **774**: p. 803-812.
91. T. Hanada, et al., *Crystal structure of CuIn₃Se₅ semiconductor studied using electron and X-ray diffraction*. Jpn. J. Appl. Phys., 1997. **36**: p. L1494-L1497.
92. C. Rincón and F.J. Raminéz, *Lattice vibrations of CuInSe₂ and CuGaSe₂ by Raman microspectrometry*. J. Appl. Phys., 1992. **72**: p. 4321-4324.
93. C. Rincón, et al., *Raman spectra of the ordered vacancy compounds CuIn₃Se₅ and CuGa₃Se₅*. J. Appl. Phys., 1998. **73**: p. 441-443.
94. P. W. Yu, *Radiative recombination in melt-grown and Cd-implanted CuInSe₂*. J. Appl. Phys., 1976. **47**: p. 677-684.
95. Y. K. Liao, et al., *Observation of unusual optical transitions in thin-film Cu(In,Ga)Se₂ solar cells*. Opt. Express, 2012. **20**: p. A836-A842.
96. Subba, R.K., *Thin films and nanostructures CuIn_{1-x}Ga_xSe₂ Based Thin Film Solar Cells*. Vol. 75. 2010: Elsevier Inc.
97. C. Rincón, J. González, and G.S. Pérez, *Luminescence and impurity states in CuInSe₂*. J. Appl. Phys., 1983. **54**: p. 6634-6636.
98. F. Abou-Elfotouh, et al., *Photoluminescence studies of CuInSe₂: identification of intrinsic defect levels*. Prog. Cryst. Growth Charact., 1984. **10**: p. 365-370.
99. R. Márquez and C. Rincón, *Defect physics of the ordered defect compound CuIn₃Se₅*. Sol. Energy Mater. Sol. Cells, 2002. **71**: p. 19-26.
100. P. Migliorato, et al., *Analysis of the electrical and luminescent properties of CuInSe₂*. J. Appl. Phys., 1975. **46**: p. 1777-1782.
101. D. Habib, et al., *Fabrication, Characterization and Optical Properties of CuIn₃Se₅ Bulk Compounds*. World J. Condens. Matter Phys., 2015. **5**: p. 201-

- 208.
102. D. Habib and G.E.H. Moussa, *Crystal Growth, Structural and Optical Studies of $CuGa_3Se_5$ Bulk Compounds*. World J. Condens. Matter Phys., 2016. **6**: p. 27-34.
103. F. A. Abou-Elfotouh, et al., *Characterization of the defect levels in copper indium diselenide*. Sol. Cells, 1991. **30**: p. 151-160.
104. S. Chatraphorn, et al., *Photoluminescence of a high quality $CuInSe_2$ single crystal*. Jpn. J. Appl. Phys., 1998. **37**: p. L269-L271.
105. S. Niki, et al., *Sharp optical emission from $CuInSe_2$ thin films grown by molecular beam epitaxy*. Jpn. J. Appl. Phys., 1994. **33**: p. L500-L502.
106. J. K. Larsen, et al., *Interference effects in photoluminescence spectra of Cu_2ZnSnS_4 and $Cu(In,Ga)Se_2$ thin films*. J. Appl. Phys., 2015. **118**: p. 035307.
107. C. H. Chang, et al., *Structure investigations of several In-rich $(Cu_2Se)_x(In_2Se_3)_{1-x}$ compositions: From local structure to long range order*. Mat. Res. Soc. Symp. Proc., 2001. **668**: p. H4.3.1-H4.3.6.
108. S. M. Wasim, et al., *Growth, structural characterization, and optical band gap anomaly in $Cu-III_3-VI_5$ and $Cu-III_5-VI_8$ Ternary Compounds*. Mat. Res. Soc. Symp. Proc., 2001. **668**: p. H1.2.1-H1.2.6.
109. S. Lehmann, et al., *Long-range structure of $Cu(In_xGa_{1-x})_3Se_5$: A complementary neutron and anomalous x-ray diffraction study*. J. Appl. Phys., 2011. **109**: p. 013518.



จุฬาลงกรณ์มหาวิทยาลัย
CHULALONGKORN UNIVERSITY

VITA

NAME Boonyaluk Namnuan

DATE OF BIRTH 08 September 1988

PLACE OF BIRTH Bangkok, Thailand

INSTITUTIONS ATTENDED B.Sc., Department of Physics, Thammasart University.
M.Sc., Department of Physics, Chulalongkorn University.

HOME ADDRESS Soi Chokchai Ruammit, Vibhavadi-Rangsit Road,
Chomphon Subdistrict, Chatuchak District, Bangkok,
Thailand, 10900

PUBLICATION [1] B. Namnuan, K. Yoodee, and S. Chatraphorn, Probing diffusion of In and Ga in CuInSe₂/CuGaSe₂ bilayer thin films by x-ray diffraction. *J. Cryst. Growth*, 2015. 432: p. 24-32.
[2] B. Namnuan, K. Yoodee, and S. Chatraphorn, Different natures of sub-gap states in 135-CIGS/112-CIGS and 112-CIGS/135-CIGS heterostructures investigated by photoluminescence technique. *J. Phys.: Conf. Series*, 2018. 1144: p. 012058.

AWARD RECEIVED [1] The best oral presentation award from Siam Physics Congress 2017 (SPC 2017), 24-26 May 2017, Rayong Marriott Resort and Spa, Thailand, in the title of "Optical properties of Cu(In,Ga)Se₂ thin films with ultra-thin B-Cu(In,Ga)₃Se₅ capping layer"
[2] The best oral presentation award from Siam Physics Congress 2018 (SPC 2018), 21-23 May 2018, Phitsanulok, Thailand, in the title of "Different natures of sub-gap states in 135-CIGS/112-CIGS and 112-CIGS/135-CIGS heterostructures investigated by photoluminescence technique"